Multiscale Modeling of Polymers: from Atomistic Structure to Macroscopic Properties

A Dissertation Presented for the

Doctor of Philosophy

Degree

The University of Tennessee, Knoxville

Nobahar Shahidi

August 2023

© by Nobahar Shahidi, 2023
All Rights Reserved.

dedicated to my dear parents for their support and encouragement.

Acknowledgments

I would like to express my utmost gratitude to my advisor, Dr. Manolis Doxastakis, who always made time to answer my questions and many doubts through the years. His tremendous support and mentorship have made this work possible.

I want to thank my collaborators, Dr. Vagelis Harmandaris, Dr. Antonis Chazirakis, Dr. Emmanuel Mapesa, Dr. Joshua Sangoro, Jeffrey Laub, and Dr. Konstantinos Vogiatzis whose work has contributed significantly to this publication. I also want to thank Dr. Michael Kilbey, Dr. Konstantinos Vogiatzis, and Dr. Brian Edwards, for serving on my committee and providing valuable suggestions.

I am thankful to have met many wonderful people through this university. I want to thank my lab mates and peers who helped me push on and gave me advice when I needed it, especially Jonathan Coote, Christopher Bottoms, Rohit Ghanta, Karthika Madathil, Mahdi Boudaghi, and Azarang Asadi.

I also want to thank my parents, my brother Omid, Johnny, and my dear grandma Malijoon for years of support, encouragement, and inspiration.

Abstract

Computer simulations serve as pillars of material engineering and design. Multiscale modeling enables the simulation of molecular phenomena at various spatial and temporal scales, aiding in the establishment of structure-property relationships for larger and more complex systems. This work focuses on predicting the properties of various polymer materials by utilizing atomistic and chemically specific coarse-grained models that enhance computational efficiency while preserving the underlying structure and characteristics.

We incorporated atomistic simulations to investigate chain motion in poly(vinyl acetate) thin films on silica. By comparing the simulation results with experimental data, we developed a comprehensive understanding of the distinct regions and relaxation modes contributing to segmental dynamics in these films. We quantified the impact of free and attractive interfaces on film dynamics and derived the temperature dependence of each relaxation mode.

Vinyl-addition polynorbornenes are high-glass transition polymers with backbone stereochemistry that is challenging to determine experimentally. We conducted simulations of polynorbornene systems with varying backbone tacticities and alkyl side chains to study the effect of microstructure on conformational, thermodynamic, and dynamic properties. Initially, we derived a representative atomistic model and subsequently created a coarse-grained model that preserves the underlying chemical microstructure to analyze high molecular weight polymers. Our results demonstrated that racemic chains formed a helical structure, and an increase in the ratio of meso isomers led to more rigid chains with faster dynamics. The helical structure persisted in alkyl-substituted racemic chains, but increasing the side chain length reduces the difference in dynamics among different backbone tacticities.

Bottom-up coarse-graining of macromolecules is commonly achieved by matching structural order parameters. Here, we introduced the distribution of nearest neighbors as an additional multibody order parameter and demonstrated that the inverse-Monte Carlo method can overcome challenges associated with the parameterization of various correlated potentials. We applied this technique to polyisoprene melts as a prototype system, and demonstrated that incorporating nearest-neighbor potentials provides a straightforward approach to match both thermodynamic and conformational properties. We find that several temperature state points can be addressed by refining the forcefield accordingly. We examined the dynamics of different coarse-grained models and found a similar acceleration of dynamics in different models.

Table of Contents

1 Introduction **1**

1.1 Thesis Outline . . . 3

2 Interfacial dynamics of poly(vinyl acetate) thin films on silica **5**

2.1 Introduction . . . 5

2.2 Method . . . 6

2.2.1 Simulation details . . . 6

2.2.2 Calculations for segmental dynamics . . . 7

2.3 Results . . . 9

2.3.1 Density profile . . . 9

2.3.2 Segmental dynamics . . . 10

2.3.3 Film and bulk dynamics at different temperatures . . . 10

2.4 Conclusions . . . 17

3 Atomistic and coarse-grained modeling of vinyl-addition polynorbornenes: The effect of stereochemistry on melt properties **19**

3.1 Introduction . . . 19

3.2 Method . . . 22

3.2.1 Atomistic simulations . . . 22

3.2.2 Coarse-graining method . . . 22

3.3 Results . . . 26

3.3.1 Forcefield optimization . . . 26

3.3.2 Thermodynamic properties and structure . . . 28

3.3.3 Chain conformation . . . 35
3.3.4 Dynamics . . . 35
3.4 Conclusions . . . 39

4 Effect of alkyl side chains on structure-property relationships of vinyl-addition polynorbronenes 41
4.1 Introduction . . . 41
4.2 Simulation details . . . 42
4.3 Results . . . 43
4.3.1 Thermodynamic properties and structure . . . 43
4.3.2 Conformational properties . . . 45
4.3.3 Dynamics . . . 47
4.4 Conclusions . . . 50

5 Coarse-graining of polyisoprene melts using inverse Monte Carlo and local density potentials 52
5.1 Introduction . . . 52
5.2 Method . . . 56
5.2.1 Atomistic simulations . . . 56
5.2.2 Coarse-grain models . . . 57
5.2.3 Inverse Monte Carlo . . . 61
5.2.4 Coarse-grained simulations . . . 63
5.3 Results . . . 64
5.3.1 Optimization . . . 64
5.3.2 Forcefields . . . 65
5.3.3 Conformational and thermodynamic properties . . . 69
5.3.4 Dynamics . . . 74
5.4 Conclusions . . . 81

6 Conclusions 84

Bibliography 86

Vita **113**

List of Tables

3.1 Studied systems include 4 different backbone tacticities with a random sequence of meso and racemo dimers at different chain lengths. 24

3.2 The parameters for Williams7B [1] forcefield with bonded parameters originally taken from CHARMM forcefield [2] and dihedral parameters from Tu et al. [3]. Meso and racemo backbone dihedrals (C_2-C_3-C_2-C_3) were optimized for PNB (this work). 25

5.1 Nomenclature for the developed CG models based on their nearest-neighbor (NN) potentials. 59

5.2 Comparison of density (ρ) and isothermal compressiblity (κ_T) of CG models with UA for various temperatures (T) at 1 bar. 73

List of Figures

2.1 Representation of the PVAC thin film on amorphous silica. The shaded area shows the trajectory of the highlighted chains in each dynamic regime during a 1.5 μs simulation run at 400 K. The dashed lines represent the boundaries of the simulation box with a periodic condition with pressure coupling. The z dimension of the box along the substrate normal vector does not have a periodic boundary condition and its size remains constant to represent the vacuum at the top. 8

2.2 Density profile of the film in the z direction at 460 K (blue) and 560 K (red). The dashed lines represent the bulk density. The dotted lines separate the vacuum interface according to Eq. 2.7. The inset shows the thickness of the top layer with temperature. 11

2.3 a) Comparison of different autocorrelation functions for quantifying segmental dynamic of PVAC film at 460 K: monomer dipole (φ, chain dipole, and backbone dihedral. b) Comparison of film and bulk φ with two different chain lengths at 560 K: $N = 10$ and $N = 30$. 12

2.4 a) Comparison of monomer dipole autocorrelation function of thin film (solid line) and bulk (dashed line) at 400 K (orange), 430 K (black), 460 K (red), 500 K (green), and 560 K (blue). b) Distribution of Debye relaxation times (ψ) for the film (solid line) and bulk (dashed line) from φ_D. c) Dielectric loss for film and bulk. Inset shows the comparison of simulation results with BDS data [4] for bulk at 470 K. 14

2.5 Average relaxation time for monomers at different film layers parallel to silica. The dashed line represents the bulk relaxation time at each temperature. . . 16

2.6 a) Monomer dipole autocorrelation function for different film layers and the average for total film compared to bulk at 500 K. 16

2.7 Relaxation map for different processes in films (circles) and bulk (squares) from simulations (open symbols) and BDS experiments (filled symbols) copied from paper [5]. High temperature BDS data, τ^*_{bulk}, is taken from literature [4]. The solid, dashed, and dash-dotted lines represent VFT fits to the slow, segmental, and fast processes respectively. The pentagon represents bulk T_g. The error bars are comparable to the symbol size. 18

3.1 Stereoregular isomers of PNB with 2,3 polymerization: a) erythro di-isotactic (meso) and b) erythro di-syndiotactic (racemic). Backbone hydrogens are drawn to note the *exo*-polymerization followed. 24

3.2 Mapping schematic for CG-PNB. Each monomer has a bead in the middle of the backbone bond (C_2-C_3) connecting it to the next monomer (red, CGB) and a bead in the middle of the other 5 ring carbons (cyan, CGS). Each CGB bead is bonded to the consecutive CGB bead as well as the middle CGS bead. 24

3.3 Energy barriers for rotation of backbone dihedral (C2-C3-C2-C3) of a) meso and b) racemo dimers. The DFT calculations are compared with data from literature calculated using the AM1 semiempirical method [6] and STO-3G *ab initio* quantum mechanical calculations [7]. Dashed lines show results from MD simulations performed with different forcefields: OPLS-AA [8], Amber99sb [9] and Williams7B [1]. 27

3.4 a) The energy difference between DFT and classical MD forcefield minimum states for meso-racemo trimers as a function of two successive backbone (C_2-C_3-C_2-C_3) dihedrals (ϕ_1 and ϕ_2) evaluated with different forcefields. Left-to-right: OPLS-AA [8], Amber99sb [9] and Williams7B [1]. b) Root mean square deviation (RMSD) between MD structures after energy minimization and DFT structures used as the initial state. 27

3.5 Rotational energy maps of trimers from DFT calculations by Jeffrey A. Laub and Dr. Konstantinos D. Vogiatzis and our MD simulations using Williams7B [1] with optimized backbone dihedrals for the meso-meso, racemo-racemo, and meso-racemo tacticities. The bottom row displays the RMSD of minimum MD structures from DFT structures. 29

3.6 The CG-PNB nonbonded radial distribution function (rdf_{nb}) compared with AA target (left) and the optimized CG-PNB nonbonded potentials (right) for: a) CGB-CGB, b) CGB-CGS and c) CGS-CGS. The forcefields were optimized separately for the following systems: meso with $N = 41$, random 50, and racemo with $N = 30$ at 800 K. 30

3.7 The bonded distribution functions for the backbone CGB bead compared with their AA target (left) and the corresponding bonded potentials (right): a) bond, b) angle, and c) dihedral. 31

3.8 a) Specific volume (V_{sp}) of PNB as a function of chain length from AA and CG simulations at 800 K. b) V_{sp} with temperature and T_g at the cooling rate of 2 K/ns for PNB-N30. Each point represents the average over a 2 K range (5000 points). Solid lines mark the linear fit to the melt and glass regimes. Dashed lines represent the intersections of linear fits that correspond to Tg. . 33

3.9 a) X-ray scattering patterns calculated for PNB-N22 at 300 K (from the cooling ramp of 10 K/ns starting from 800 K) compared with WAXS experimental data with unknown tacticity from Wozniak et al. [10] ($\lambda = 0.154$ nm). b) Intra-molecular and inter-molecular radial distribution function of carbons (g_{CC}). 34

3.10 a) Normalized correlation of the C_2-C_3 bond vector (with length l_b) for PNB-N30 and b) characteristic ratio ($C_{\Delta n} = < R_e^2(\Delta n) > /2(\Delta n + 1)l^2$ with $l = 1.53$ Å) as a function of monomer distance (Δn) for PNB-N30 and PNB-N41 at 800 K. c) Schematic representation of a meso (top) and a racemo (bottom) PNB-N30 chain at 800 K. 36

3.11 a) characteristic ratio as a function of monomer distance using AA and CG models. b) Mean squared chain end-to-end distance ($\langle {R_e}^2 \rangle$) as a function of chain length. Inset shows ratio of $\langle {R_e}^2 \rangle$ over mean squared radius of gyration ($\langle {R_g}^2 \rangle$) for different chain lengths (N) at 800 K. c) Normalized correlation of the C_2-C_3 bond vector for racemo chains. d) Schematic representation of racemo CG-PNB chain with $N = 100$. 37

3.12 a) Normalized correlation of the C_2-C_3 bond vector for racemo chains sing AA and CG models. b) Schematic representation of racemo CG-PNB chain with $N = 100$. 38

3.13 a) Autocorrelation of end-to-end vector (solid lines) and bridge vector (dashed lines) from the middle of C2-C3 to C7 and b) Mean square displacement (MSD) of chain center of mass for PNB with $N = 41$ at 800 K. c) Diffusion coefficient (D) of different PNB tacticities as a function of chain length. CG values are scaled to match AA values at $N = 41$. 40

4.1 a) Specific volume (V_{sp}) with tacticity for PNB-C6 and PNB-C9 at 700 K. b) V_{sp} with temperature and T_{g} at the cooling rate of 10 K/ns for PNB-C6 and PNB-C9. Each point represents the average over a 5 K range (6000 points). Solid lines mark the range of linear fit. Dashed lines show the interception corresponding to Tg. Error smaller than symbol size. 44

4.2 a) X-ray scattering patterns calculated for PNB-C6 compared with experimental data from two samples with unknown tacticities from Kai *et al.* [11] ($\lambda = 0.1$ nm). b) X-ray scattering for PNB-C9 compared with PNB-C8 and PNB-C10 from Wozniak *et al.* [10] ($\lambda = 0.154$ nm). c) Intra-molecular and inter-molecular radial distribution function ($\mathrm{g_{CC}}$) of PNB-C6. All data at 300 K. 46

4.3 Characteristic ratio ($C_n = < R_e^2 > /2(n+1)l^2$ with $l = 1.53\,\text{Å}$) as a function of monomer distance (n) for a) PNB and PNB-C6 at 800 K and b) PNB-C6 and PNB-C9 with at 700 K. 48

4.4 Normalized correlation of the C_2-C_3 bond vector (with length l_b) for a) PNB-C6 at 700 K. b) Effect of alkyl side chain on conformation and secondary-structure of racemo chains at 700 K and 800 K. 49

4.5 a) Autocorrelation of chain end-to-end vector, b) MSD, c) autocorrelation of Rouse modes for PNB-C6 with racemo tacticity, d) average Rouse times normalized by first mode for PNB-C6 (dashed line represents the Rouse prediction of $1/p^2$) at 700 K and 800 K, e) average Rouse times, and $G(t)$ of g) PNB-C6 and h) PNB-C9. All simulations are at 700 K unless otherwise specified. 51

5.1 a) Distribution of the number of nearest-neighbors (n) extracted with SANN [12] (symbols) and by the use of indicator functions (lines) at 298 K (blue), 353 K (green) and 413 K (red). b) Nearest neighbors (blue) of a CG bead (red) as extracted from SANN analysis on a mapped atomistic configuration. The dashed red lines represent a circle centered on the examined bead. c) Total pair-distribution function (g) and contribution from nearest-neighbors (g_{NN}) as determined by SANN at 413 K. The dashed line depicts the extracted indicator function Θ. d) $\Theta(r)$ extracted at different temperatures. 59

5.2 a) Convergence of distributions to target values during the IMC process (inset shows the convergence of density to the UA value at 1 bar) and optimization of the b) pair nonbonded potentials and c) nearest-neighbor potentials at 413 K for the CG-CN in the *NPT* ensemble. 66

5.3 a) Bond-stretching, b) Angle-bending, c) Dihedral, d) Pair non bonded, and e) Nearest-neighbor potentials for CG-CN (−), CG-NN (- -) and CG-pair (· - ·) at 353 K. 68

5.4 a) Pair nonbonded and b) nearest-neighbor potentials for CG-NN (−) and CG-CN (- -) at 298 K (blue), 353 K (green) and 413 K (red). 70

5.5 Distributions produced by the CG-CN forcefield (lines) and the mapped atomistic trajectory (symbols) at 298 K. At higher temperatures, the comparison was even more favorable. 71

5.6 a) Characteristic ratio (C_N) as a function of monomer distance (N) in a chain with 30 repeat units, b) distribution of chain end-to-end distances, and c) distribution of distances for CG beads separated by three bonds for mapped UA and CG models (CG-NN, CG-CN, and CG-pair) at 353 K. 73
5.7 Mean square displacement (MSD) for the segment (monomer) and chain center-of-mass from UA and CG simulations (CG-CN, CG-NN, and CG-pair) at different temperatures: a) 413 K, b) 353 K and c) 298 K. 76
5.8 Single chain dynamic structure factor S(q,t) from UA and CG-NN models at $q = 3, 6, 9$, and 12 nm^{-1}, at different temperatures: a) 413 K, b) 353 K and c) 298 K. 79
5.9 Average relaxation time of the single chain structure factor (τ_{NSE}) as a function of the scattering vector (q) at 413 K (red), 353 K (green), and 298 K (blue). 83

Chapter 1

Introduction

Specialty and composite polymers are designed by modulating the structure and composition of polymers for enhanced performance, such as withstanding large deformation, high fatigue resistance, keeping a high elastic modulus, and improving biodegradability. Designing high-performance polymers relies on a comprehensive understanding of their hierarchical structure and behavior. Theoretical methods offer valuable insight alongside experiments; however, they generally do not account for specific microscopic characteristics or rely on experimental input to do so. For instance, the agreement between experimental data and theory for the free energy of mixing polymers is often semi-quantitative and the standard Flory-Huggins parameter [13, 14, 15] is not a reliable indication of miscibility for real systems [16, 17, 18].

In the past decades, computer simulations of materials have evolved significantly with the fast growth of high-performance computing and are well-established alongside experimental and analytical theories as pillars for material engineering and design. The design objective is to propose the optimal molecular parameters to produce novel polymers with select characteristics. Multiscale material modeling facilitates this process by enabling us to directly examine polymer behavior at different length scales and predict the macroscopic properties of the system from microscopic mechanisms and molecular structure without employing empirical constitutive models. Polymer length scales and their corresponding dynamics span over several orders of magnitude, from the vibration of atoms to the reptation of long chains. In theory, all-atom (AA) models can be used to predict macroscopic behavior; however, with the current computational resources, the time and length of simulations are

still limited to micro scale due to the system size and femtosecond time step employed [19]. Commercial polymers have thousands of repeat units and long correlation times that scale with their molecular weight ($\sim M_w^{3.4}$) which makes accurate sampling and observing important phenomena such as phase separation and crystallization with AA models onerous.

Lower resolution coarse-grained (CG) models have been developed to enable studying the spatial and temporal evolution of systems on large scales that are relevant to macromolecules [20]. Bottom-up coarse-graining methods reduce the degrees of freedom by eliminating certain details of the AA model in the chosen CG mapping. Multiple atoms are mapped to a single CG bead and the interactions between the beads are calculated by matching a set of specific target properties that are obtained from AA simulations. In cases where AA details are needed but the system has a long equilibration time, an equilibrated CG structure can be mapped to a higher resolution model using various back-mapping methods [21, 22]. Different bottom-up methods have been developed that match different target properties, such as the iterative Boltzmann inversion (IBI) [23] and inverse Monte Carlo (IMC) [24] that match a set of structural distributions, force matching [25, 26] and conditional reversible work method [27] that match the potential of mean force, and optimization of relative entropy [28, 29]. Unlike top-down methods, bottom-up coarse graining does not rely on experimental input and can be used to study novel systems and conditions where the relevant experimental data is not available. As computational efficacy is rapidly growing, so are the size and complexity of simulated systems which justifies continuous developments of CG models for efficient equilibration and accurate sampling [30].

Due to the reduction of degrees of freedom, CG models do not preserve all the properties of the underlying AA model. The most common method for coarse-graining polymers is the IBI method which uses an iterative process to optimize potentials in order to match structural distributions, such as the radial distribution function and distribution of bonds, angles, and dihedrals. The resulting CG model can reproduce the target structure but often fails to match the thermodynamic properties and overestimates the pressure by several orders of magnitude. One solution is further optimization of non-bonded pair potentials by adding a linear correction [31, 23] that can fix the pressure of the CG system and enable studies in the isothermal–isobaric ensemble. Similar techniques have been implemented

in other methods such as incorporating pressure constraints in IMC and force-matching methods [32, 33, 34], and inclusion of volume-dependant potentials [35]. However, fixing the pressure will not necessarily calibrate other thermodynamic properties such as isothermal compressibility [36, 37, 38]. Another issue is the correlation between different potentials. In the IBI method, this correlation is not incorporated in the optimization term and often several cycles of optimization are performed to match all the distribution terms. Similarly, the posterior modification of potentials for pressure matching requires further optimization to keep the target properties intact [31, 23]. More importantly, the implementation of these techniques is not straightforward in multi-component systems. Another challenge is that the CG forcefield is usually not transferable across different thermodynamic states [31, 33, 39] and can only describe the system close to the temperature, density, and composition the forcefield was derived from. Coarse graining multi-component systems present additional challenges since the forcefield is utilized across different compositions and micro-phases.

1.1 Thesis Outline

We employed molecular simulations to characterize different polymer systems in the following chapters. We applied density functional theory calculations to inform the AA representation of chapter 3 and developed bottom-up CG models to predict properties of high-glass transition polymers. We employed different coarse-graining methods throughout this work and introduced a novel method for macromolecules that was shown to improve CG representability in chapter 5.

Chapter 2 focuses on segmental dynamics of thin poly(vinyl acetate) films on silica and the effect of substrate and free interfaces on overall film dynamics compared to bulk. We performed AA simulations to characterize molecular motion in the interface layers over a broad range of temperatures and showed the existence of three distinct dynamic regimes throughout the film. We compared our findings directly with experimental broadband dielectric spectroscopy to depict a comprehensive picture of temperature-dependence of different molecular motions in the poly(vinyl acetate)-silica system. Although our simulations proved to be a good match for experimental data, AA simulations were

limited to short oligomers at high temperatures due to the slow relaxation times at the substrate interface. This further illustrates the need for CG models in more complex systems for simulations to more closely resemble experimental and practical conditions.

High-glass-transition polymers are another class of materials where mesoscale modeling is required for accurate sampling. In chapter 3 we use simulations to establish the effect of stereochemistry on conformational, thermodynamic, and dynamics properties of rigid and intractable vinyl-addition polynorbornenes. Since this polymer is challenging to describe with general forcefields commonly used for hydrocarbons [7, 6, 40], we first validated and optimized the AA forcefield by comparing the rotational energy barriers with density functional theory calculations of different trimers. Subsequently, we used AA simulations to predict properties of polynorbornenes with different backbone tacticities and developed a CG model based on AA structure to simulate high molecular weight chains. In chapter 4, we extended our research to the structure-property relationship of alkyl-substituted polynorbornenes which can function as templates for the design of high-performance thermoplastics. Alkyl side chains can be used to tune thermal properties and improve melt processability, but the direct determination of backbone stereochemistry is challenging in such materials. Therefore we used simulations to determine the role of both backbone tacticity and side chain length on polymer properties.

Finally in chapter 5, we introduced a novel method for systematic bottom-up coarse-graining of macromolecules by including nearest-neighbor potentials in the forcefield and using the IMC method to simultaneously optimize different terms in forcefields while accounting for their cross-correlations. The nearest-neighbor potentials are multi-body in nature and are used to improve the representability of the CG model by supplementing the nonbonded potentials which are assumed to be pair-wise. We developed a method to define a system-specific indicator function to calculate local density. Consequently, by applying this method to polyisoprene melts at different temperatures, we showed that the inclusion of fully attractive or unconstrained nearest-neighbor potentials in the model results in the accurate prediction of pressure and isothermal compressibility as well as structure and conformation. We also investigated the effect of these potentials on segmental and chain dynamics at different length scales and showed that this multi-body term does not affect dynamic scaling.

Chapter 2

Interfacial dynamics of poly(vinyl acetate) thin films on silica

This chapter is based on the following publication:

Mapesa, E. U., Shahidi, N., Kremer, F., Doxastakis, M., & Sangoro, J. (2020). Interfacial Dynamics in Supported Ultrathin Polymer Films—From the Solid to the Free Interface. The Journal of Physical Chemistry Letters, 12(1), 117-125 [5].

2.1 Introduction

Thin polymer films are used for a broad range of applications. They are heterogeneous systems with altered dynamic and thermodynamic properties at the interfaces. Interfacial dynamics of polymer thin films are relevant for their application in adhesion, coatings, and nano-composites. Properties like the glass transition temperature (T_g) that are used to represent segmental dynamics of bulk polymers are limited for inferring dynamics in thin films, since segmental dynamics do not change in accordance with the value of T_g in confinement [41, 42, 43].

Molecular dynamics (MD) simulations of polymers near an attractive substrate have demonstrated the existence of different dynamic regimes in film and limited mobility in the first adsorbed layer. Such behavior has been confirmed by probing different properties. Mortazavian *et al.* [44] have shown a gradient in mobility and T_g in different regions of

poly(vinyl acetate) (PVAC) film on silica. Rissanou *et al.* [45] have shown the dynamic regimes for chain and segmental relaxation of different polymers on graphene, which exhibit slower and more heterogeneous dynamics near the substrate. Studies of dynamics in confined polybutadiene films on graphite have also shown altered segmental dynamics close to the attractive substrate with an additional relaxation mode [46, 47, 48]. We performed MD simulations of PVAC films on amorphous silica to directly probe the properties as a function of both film depth and temperature and aid the interpretation of experimental broadband dielectric spectroscopy (BDS) data provided by our collaborators, Dr. Emmanuel U. Mapesa and Dr. Joshua Sangoro [5].

We demonstrate that while the mean rates of the segmental relaxation remain bulk-like, modified molecular mobilities arise in the interfacial zones. Finally, we study the temperature dependence of different relaxation modes present in the PVAC-silica system. The temperature dependence of the adsorbed layer in different systems is a topic of discussion [49, 50, 51]. In this chapter, by combining simulation and experimental data we derive the relaxation times of the different relaxation regimes present in film over a large temperature range.

2.2 Method

2.2.1 Simulation details

MD simulations were performed with the GROMACS 2018.3 package [52, 53]. Atactic PVAC was modeled with full atomistic detail and partial charges using the OPLS-AA forcefield for hydrocarbons [54, 8]. We employed an atomistic model of amorphous silica to simulate the oxidized layer in contact with the films in experiments. The nonbonded parameters for silica were taken from Lopes *et al.* [55] and Ndoro *et al.* [56]; the bonded parameters and initial structure were adopted from Pandey *et al.* [57] and hydrogens were added to the structure. Fig. 2.1 shows a representation of simulation box and chain trajectories. The simulations were performed with a 2 fs time step with semi-isotropic pressure coupling using the Berendsen barostat [58] and velocity re-scaling thermostat [59] with a time step of 1.0

ps and 0.1 ps, respectively. The box depth was kept constant to include a vacuum on top of the PVAC. Non-bonded interactions were switched to zero at 1.3 nm without long-range dispersion correction. A reaction field was employed for the Coulomb interactions with a relative dielectric constant of ϵ_{rf}=3.8 (adopted from the average experimental dielectric constant of silica and PVAC at room temperature [56, 60]). The bulk with N=10 repeat units has a density of 1.073 g/cm^3 at 400 K which is in agreement with the experimental value of 1.107 g/cm^3 [61]. PVAC films each contained 614 chains with N=10 (M_w=860 g/mol) and were simulated at temperatures of 560, 530, 500, 480, 460, 430, and 400 K at the pressure of 1 bar. The films were each equilibrated for 200, 250, 300, 450, 450 ns, and 1.5 μs respectively, resulting in thin films with thicknesses ranging from 13.4 to 17 nm, as temperature decreases.

2.2.2 Calculations for segmental dynamics

To compare our results directly to experiments, we quantified segmental dynamics in the time domain by calculating the z-component of the monomer dipole autocorrelation function (φ):

$$\varphi(t) = \frac{\langle \vec{\mu_z}(t_0+t).\vec{\mu_z}(t_0)\rangle}{\langle \vec{\mu_z}(t_0).\vec{\mu_z}(t_0)\rangle} \tag{2.1}$$

where $\vec{\mu_z}(t) = \sum_i q_i.\hat{e_z}.\vec{r_i}(t)$ is the z-component of monomer dipole moment (along the surface normal) at time t. The complex dielectric permittivity (ϵ^*) in the frequency domain is the Fourier transform of the derivative of $\varphi(t)$:

$$\frac{\epsilon^*(\omega)-\epsilon_\infty}{\epsilon_\infty-\epsilon_0} = 1 - i\omega\int_0^\infty \frac{d\varphi(t)}{dt}\exp\left(-i\omega t\right)dt \tag{2.2}$$

The resulting $\varphi(t)$ was estimated as a superposition of Debye relaxations (φ_D) with relaxation time τ to calculate the equivalent loss profile ($\epsilon^{"}$) analytically (Eq. 2.4). The distribution of relaxation times (ψ) were fitted using the CONTIN package [62, 63, 64]:

$$\varphi_{\mathrm{D}}(t) = \sum_\tau \psi(\tau)\exp\left(\frac{-t}{\tau}\right) \tag{2.3}$$

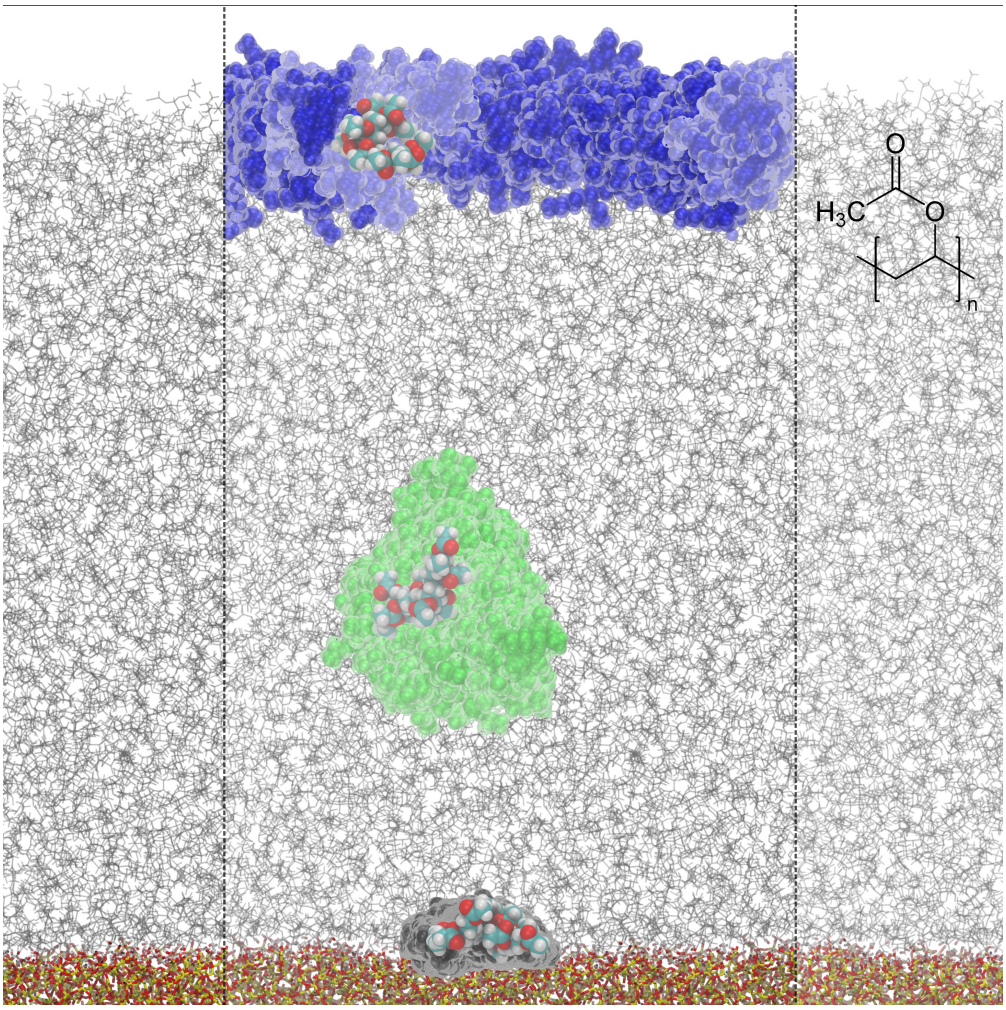


Figure 2.1: Representation of the PVAC thin film on amorphous silica. The shaded area shows the trajectory of the highlighted chains in each dynamic regime during a 1.5 μs simulation run at 400 K. The dashed lines represent the boundaries of the simulation box with a periodic condition with pressure coupling. The z dimension of the box along the substrate normal vector does not have a periodic boundary condition and its size remains constant to represent the vacuum at the top.

We calculated $\epsilon^{"}$ from the distribution of Debye times and normalized it by the difference in permittivity at the infinite (ϵ_∞) and zero (ϵ_0) limit of frequency:

$$\frac{\epsilon^{"}(\omega)}{\epsilon_\infty - \epsilon_0} = \sum_\tau \psi(\tau) \frac{\omega\tau}{1 + (\omega\tau)^2} \tag{2.4}$$

Segmental relaxation of bulk PVAC can be fitted with a Kohlrausch-Williams-Watts (KWW) function [65] and the film can be fitted as a sum of two stretched exponential functions that represent the two main processes, bulk-like (m) and slow process (s):

$$\varphi_{\mathrm{KWW}}^{\mathrm{film}} = \alpha_{\mathrm{m}} \exp\left(-\left(\frac{t}{\tau_{\mathrm{m}}}\right)^{\beta_{\mathrm{m}}}\right) + \alpha_{\mathrm{slow}} \exp\left(-\left(\frac{t}{\tau_{\mathrm{slow}}}\right)^{\beta_{\mathrm{slow}}}\right) \tag{2.5}$$

where τ is the KWW relaxation time and β describes the heterogeneity of the distribution of relaxation times. The α parameter represents the weight of each term in $\varphi(t)$. Using the KWW fits, we extracted the average characteristic relaxation time for each process (τ_i):

$$\langle\tau_i\rangle = \frac{\alpha_i}{\beta_i}\Gamma\left(\frac{1}{\beta_i}\right)\tau_i \tag{2.6}$$

2.3 Results

2.3.1 Density profile

Fig. 2.2 shows the density profile of the PVAC film compared with bulk density at 460 and 560 K. The density is displayed as a function of distance from the silica substrate. Each bin displays the density for a layer normal to the substrate with a thickness of 0.1 nm. Accumulation of segments near the attractive substrate results in a peak at the adsorbed layer [45, 44, 48, 46, 47] at ∼0.7 nm. The effect of the substrate on density is short-ranged and after ∼1.6 nm, the density decays to a plateau that matches the bulk density. The drop in density from the bulk value at the top of the film marks the vacuum interface. This drop was fitted with the hyperbolic tangent function to determine the position of the interface:

$$\rho(d) = \frac{\rho_{\mathrm{bulk}}}{2}\left(1 - \tanh\left(\frac{2(d - d_{\mathrm{e}})}{\delta}\right)\right) \tag{2.7}$$

The width of the vacuum interface ($\approx 2\delta$ from the equation above) slowly expanded with temperature (as shown in the inset of Fig. 2.2), while the position of the substrate peak remained constant.

2.3.2 Segmental dynamics

We compared different measures of segmental dynamics by comparing different relaxation functions. The autocorrelations of chain dipole and backbone dihedral are compared with $\varphi(t)$ in Fig. 2.3.a. Although the main component of the monomer dipole is located in the side chain, the re-orientation of the backbone plays an important part in the segmental relaxation. The three measures of segmental dynamics follow a similar trend, although chain dipole and dihedral autocorrelation functions probe larger segments and are slower at longer times. Probing the autocorrelation of monomer dipole improves the statistics and permits a more detailed analysis of dynamics throughout the film thickness. Relaxation of the chain dipole is qualitatively similar to the monomer dipole but the decay of the adsorbed segments is even slower when cross-correlations between monomers are accounted for. The average relaxation time for chain dipole autocorrelation in the film is ∼7.5 times larger than bulk.

The segmental dynamics of PVAC depend on molecular weight and still display end-group effects even at high molecular weights [66]. Fig. 2.3.b displays the average $\varphi(t)$ of film and bulk at 560 K for two different chain lengths, $N = 10$ ($M_w = 860$ g/mol, $\rho = 0.945$ g/cm^3) and $N = 30$ ($M_w = 2582$ g/mol, $\rho = 0.975$ g/cm^3). Both systems show a similar trend in dynamics with a bulk-like relaxation at short times and a second slow relaxation at longer times. The dynamics in the $N = 30$ system are slower due to the higher density and the difference between the two modes in film is more apparent. The average film relaxation time that is ~ 5 times larger than bulk for $N = 30$ and ~ 1.5 times larger for $N = 10$.

2.3.3 Film and bulk dynamics at different temperatures

Fig. 2.4.a contrasts φ of film and bulk over a large temperature range (400−560 K). The initial steep drop is due to the fast vibrational motion. The film behavior at short times is similar to bulk, but the dynamics at larger time scales are significantly slower. An additional

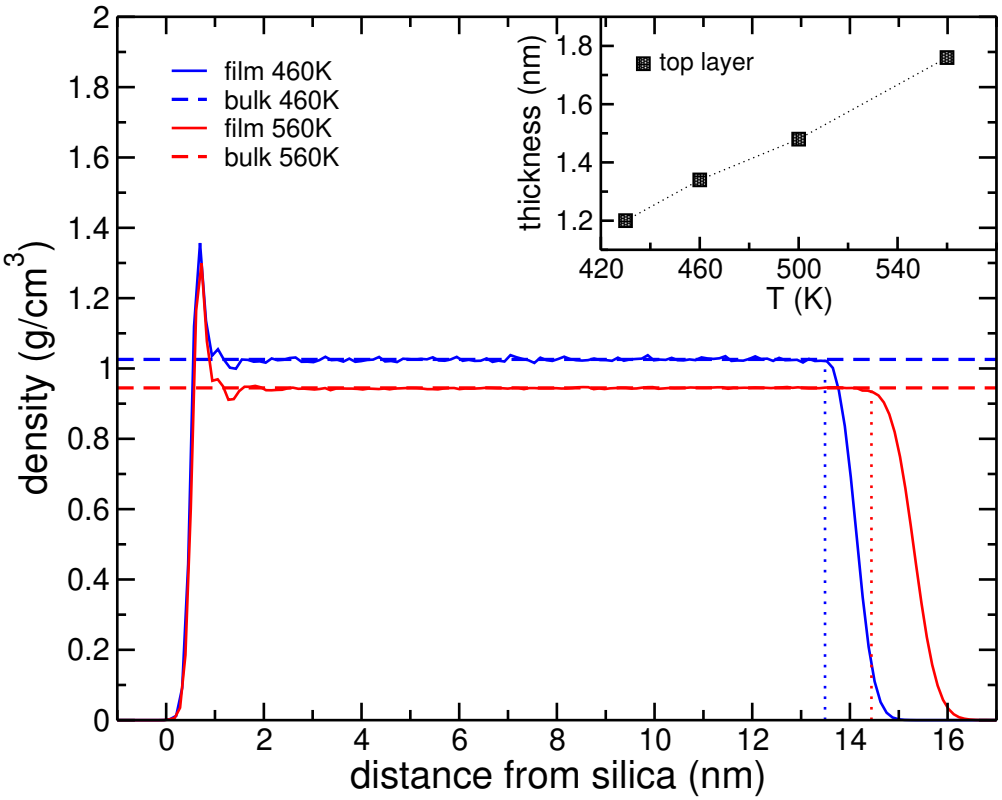
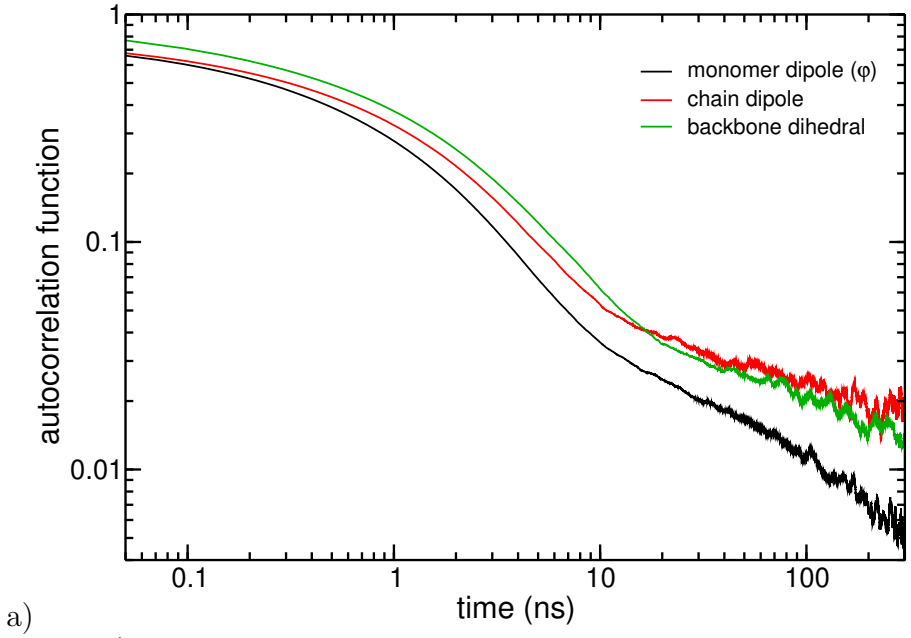
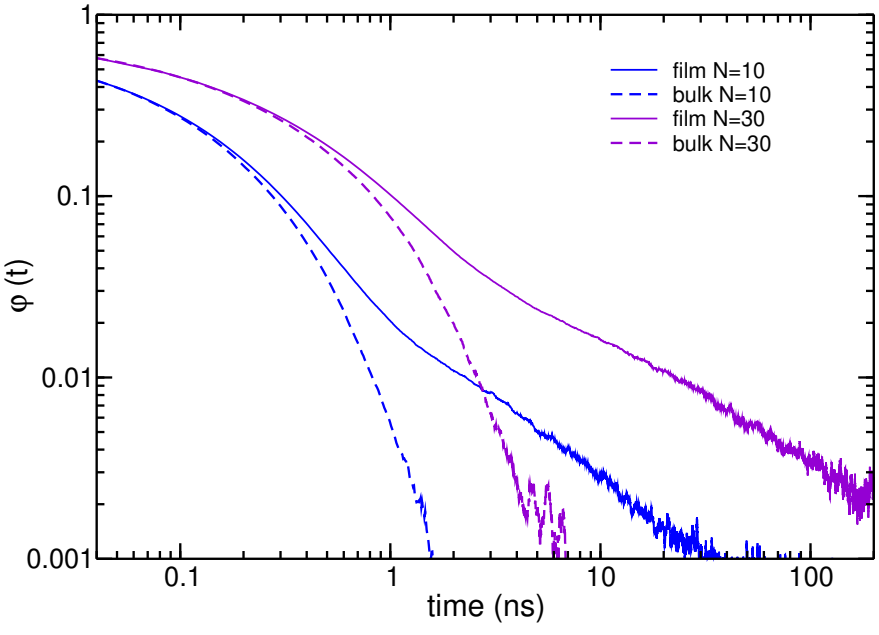


Figure 2.2: Density profile of the film in the z direction at 460 K (blue) and 560 K (red). The dashed lines represent the bulk density. The dotted lines separate the vacuum interface according to Eq. 2.7. The inset shows the thickness of the top layer with temperature.



a)



b)

Figure 2.3: a) Comparison of different autocorrelation functions for quantifying segmental dynamic of PVAC film at 460 K: monomer dipole (φ, chain dipole, and backbone dihedral. b) Comparison of film and bulk φ with two different chain lengths at 560 K: $N = 10$ and $N = 30$.

relaxation mode emerges at large time scales. This mode is not present in bulk and is due to the absorption of PVAC chains on the silica surface. This additional relaxation caused by polymer adsorption onto the attractive substrate has been observed in other systems [46, 47, 48] and resulted in more heterogeneous dynamics compared to bulk polymer [45]. Due to the presence of the hydrogen bonds, PVAC and silica have stronger interactions in comparison which results in much slower film dynamics.

To obtain a comprehensive image of the different relaxation processes in film and bulk, we compare the distribution of characteristic relaxation times. The fast vibrational relaxation was excluded since the relaxation times are close to the time step of fluctuations present in the MD simulation. Fig. 2.4.b shows the distribution of Debye relaxation times for film and bulk at different temperatures. As observed in dielectric loss form BDS experiments [5], the range of relaxation times is broader in films with both faster and slower times. There are two peaks present in the film with separate distributions that indicate two separate relaxation processes. The first peak belongs to the main segmental relaxation and is similar to bulk with additional distributions at small relaxation times. The mode relaxation time (τ_{m}) for this process is in close agreement with the bulk value. The second peak (τ_s) belongs to the additional process caused by adsorption with larger relaxation times that are not present in bulk and its relative strength compared to τ_{m} increases at lower temperatures. In addition, both film peaks, as well as the bulk distribution, become broader with decreasing temperature.

We study the effect of polymer-silica and the polymer-vacuum interfaces on dynamics by systematically probing segmental motion in different layers throughout the film. The layers are defined based on the center of mass distance of the monomers from the silica surface and are each about 1 nm thick. The monomer dipole autocorrelation function for each layer is calculated for monomers that are in that layer at time t to improve the statistics. The average relaxation time for each layer is calculated as $\langle\tau_{\mathrm{layer}}\rangle = \int_0^\infty \varphi_{\mathrm{layer}}(t)dt$ and presented in Fig. 2.5 as a function of layer distance from the silica interface at different temperatures.

Based on the profile of the relaxation times throughout the film, we define three main layers. Similar to the density profile (Fig. 2.2), the middle layer away from the two interfaces has bulk-like dynamics. The bottom layer (near the substrate) has much slower dynamics

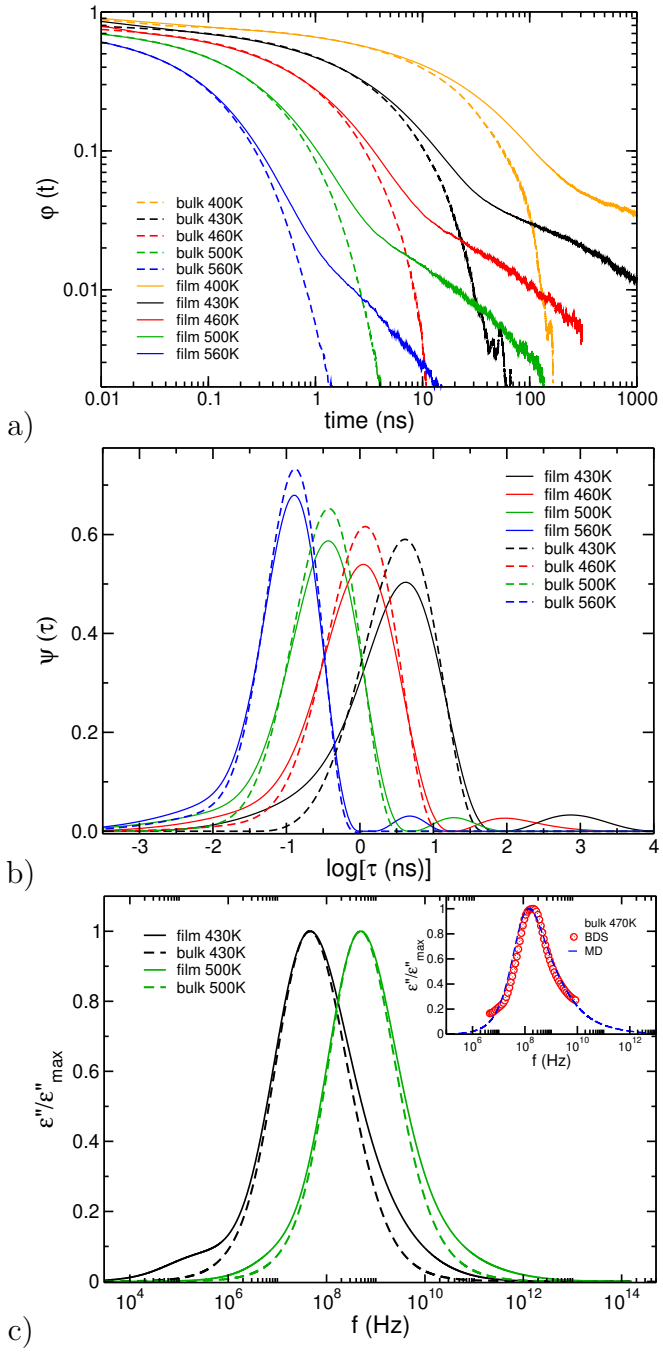


Figure 2.4: a) Comparison of monomer dipole autocorrelation function of thin film (solid line) and bulk (dashed line) at 400 K (orange), 430 K (black), 460 K (red), 500 K (green), and 560 K (blue). b) Distribution of Debye relaxation times (ψ) for the film (solid line) and bulk (dashed line) from φ_D. c) Dielectric loss for film and bulk. Inset shows the comparison of simulation results with BDS data [4] for bulk at 470 K.

(more than 10 times slower than bulk); the thickness of this bottom layer is around 4 nm and does not have a strong correlation with temperature. However, the contribution of the bottom layer to overall film dynamics increases with decreasing temperature since the fraction of monomers near the substrate increases with density. Finally, segmental relaxation is faster in the top layer (close to the vacuum interface), and its thickness and mole fraction increase at low temperatures. The relaxation time of the free segments near the vacuum approaches the bulk value at high temperatures hence the decrease in top layer thickness as defined here. Notably, the thickness of the layers as defined by dynamics is different from that determined by the density profile.

The dynamics of the three main layers for the thin film at 500 K are presented in Fig. 2.6. It is apparent that the additional slow relaxation mode is only present in the adsorbed layer which is ∼4 nm thick ($\approx 6.5R_g$) at all temperatures. The distributions for film and bulk are normalized while the layers' distributions are weighted based on their number density so that the total film distribution is the sum of layer distributions. The distribution at the top layer has a strong overlap with the middle layer with a faster mode. The distribution in the middle layer is very similar to bulk. There's a higher error at the interface layer due to slow dynamics and lower statistics. The main relaxation at the substrate layer is similar to the middle layer. The second relaxation mode with higher τ is responsible for the slower dynamics close to the surface. The overall film dynamics are dominated by the large middle layer with an additional slower relaxation mode from the adsorbed layer. The top layer has the smallest weight fraction and has less effect on overall film dynamics.

Fig. 2.7 displays the temperature dependence of the characteristic mean relaxation times for the three main regimes of segmental dynamics from our simulations as well as BDS results from collaborators. The simulation $\langle\tau_m\rangle$ and $\langle\tau_{slow}\rangle$ are mean relaxation times from KWW fits of the total film $\varphi(t)$ (using Eq. 2.5). Since there is a lot of overlap between relaxation times of the top layer and middle layer, τ_{fast} was extracted by fitting $\varphi(t)$ for only the top layer (as shown in Fig. 2.6). The experimental τ were extracted by fitting the dielectric loss spectra of the film with three Havriliak-Negami functions [67] which correspond to the three relaxation regimes [5]. Due to the computational cost of the atomistic model, simulations were performed at high temperatures due to the long relaxation times and limited statistics close

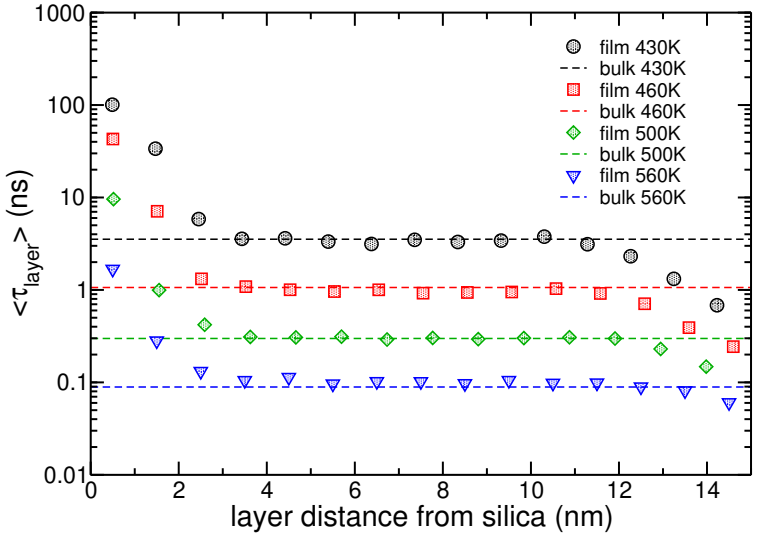


Figure 2.5: Average relaxation time for monomers at different film layers parallel to silica. The dashed line represents the bulk relaxation time at each temperature.

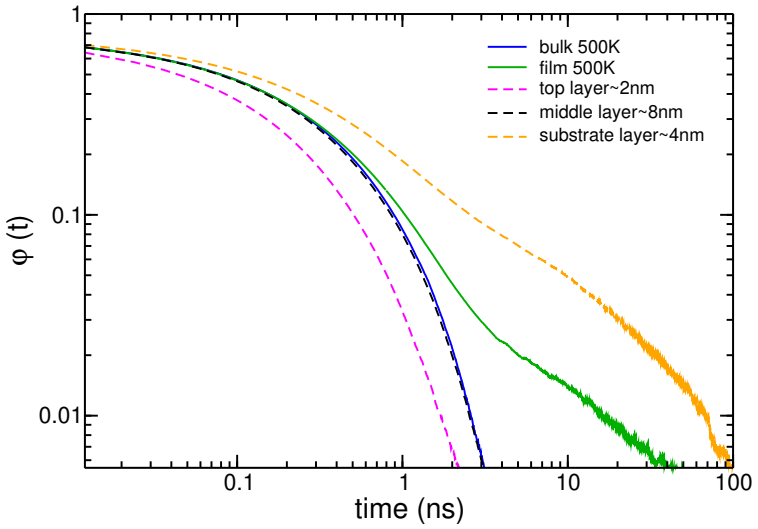


Figure 2.6: a) Monomer dipole autocorrelation function for different film layers and the average for total film compared to bulk at 500 K.

to the surface. There is also a low probability for whole molecules to adsorb on the substrate contributing to an average relaxation that potentially is slower due to the short chains modeled compared to the experimental system. Decomposition to separate processes also involves numerical errors for both simulation and experimental data. Nonetheless, relaxation times extracted from experimental and simulation data for thin films and bulk PVAC appear to coincide, and their temperature dependence can be described by a single Vogel-Fulcher-Tammann (VFT) function [68, 69, 70] defined as $\tau(T) = \tau_0 \exp\left[(D \times T_V)/(T - T_V)\right]$. The VFT parameters for slow, main and fast relaxations are $\log(\tau_0) = [9.1, 12.1, 11.9]$, $D \times T_V = [1093.5, 1409.2, 1472.5]$ K and $T_V = [271.9, 268.8, 232.3]$ K. There is a discrepancy in the literature concerning whether the slow process arising from the substrate-polymer interface has Arrhenius or non-Arrhenius temperature dependence [49, 50, 51]. In this study, by combining experimental and simulation results, we unambiguously show that both τ_{slow} and τ_{fast} have VFT-like activation for the PVAC-silica system.

2.4 Conclusions

We observed that the effect of free and attractive interfaces on the thermodynamic and dynamic properties of PVAC thin films are short-ranged and the middle layer between the two interfaces is bulk-like. An additional relaxation mode exists in the adsorbed layer which is up to two orders of magnitude slower than bulk and is the biggest contributor to modified dynamics in film at high temperatures. The segmental motion in the free layer near the vacuum is faster than bulk but has a strong overlap with bulk relaxation times at the high temperatures simulated here. By combining simulation results with experimental BDS data at low temperatures, we observed that each of the three main relaxation modes has a distinct non-Arrhenius temperature dependence that can be fitted with a VFT function. Consequently at low temperatures near T_g, the slow and main relaxation modes overlap and the fast relaxation at the free layer becomes distinct from bulk. The length of the interface layers as defined by segmental dynamics has a weak correlation with temperature, but as we cool the system, the molar ratio of the interface layer increases compared to the bulk-like layer and so does its contribution to segmental relaxation in film.

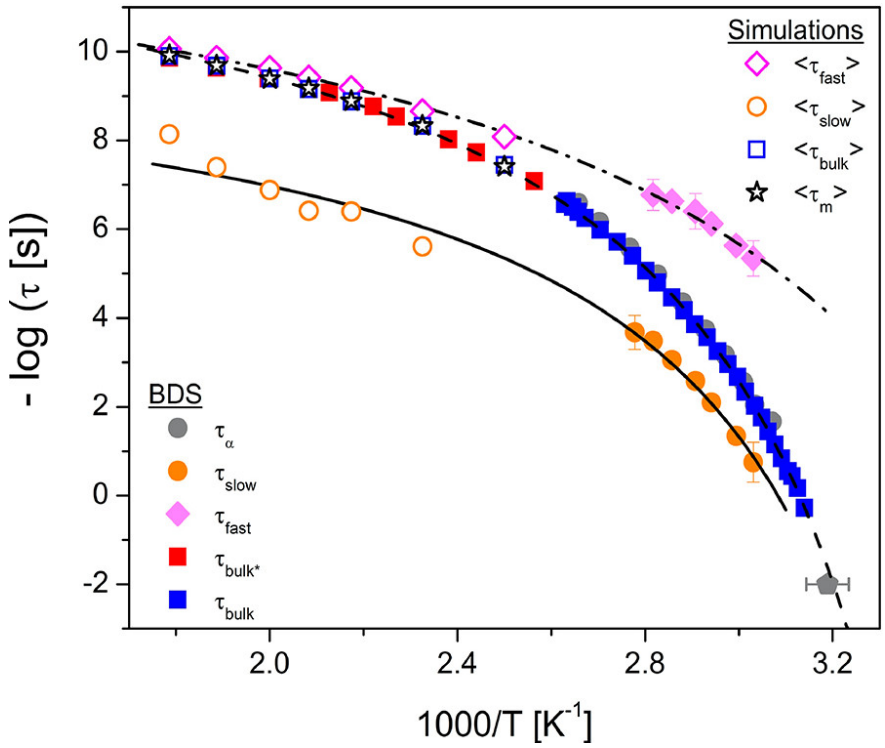


Figure 2.7: Relaxation map for different processes in films (circles) and bulk (squares) from simulations (open symbols) and BDS experiments (filled symbols) copied from paper [5]. High temperature BDS data, $\tau^*_{\rm bulk}$, is taken from literature [4]. The solid, dashed, and dash-dotted lines represent VFT fits to the slow, segmental, and fast processes respectively. The pentagon represents bulk $T_{\rm g}$. The error bars are comparable to the symbol size.

Chapter 3

Atomistic and coarse-grained modeling of vinyl-addition polynorbornenes: The effect of stereochemistry on melt properties

3.1 Introduction

Vinyl-addition polynorbornenes (PNB) display unique characteristics such as high glass transition temperature (T_g), high thermal and chemical stability, low dielectric constant, non-hygroscopicity, high transparency, low birefringence, and high permeability [71, 72, 73]. Subsequently, it is suitable for diverse applications such as thermoplastic elastomers [74, 75], high-performance polymers for gas separation membranes [76, 77, 78, 79, 80, 81, 10, 82], microelectronic applications [83, 84], as well as anion-exchange membranes and fuel cells [85, 86, 87, 88, 89, 90]. In several of these potential applications, selective functional substitutions are incorporated to increase melt processability and tailor its properties to the desired specifications [91, 83, 78, 80, 92, 81, 93, 94, 95, 75, 96, 10].

Unsubstituted PNB is not melt processable due to the small window (∼30 K [75]) between its thermal decomposition temperature and T_g (493–663 K [7, 83, 97]). It is also

brittle and often exhibits poor solubility in common organic solvents [7]. However, reported properties vary significantly depending on the catalyst employed for the polymerization reaction and the conditions followed during synthesis [98, 99]. This discrepancy has been attributed to the presence of distinct isomers which is supported by the stereospecificity of different metallocene precursors [100]. While six different stereoregular norbornene polymers could be formed [71], *cis-exo* insertion is expected to lead to erythrodiisotactic (meso), erythrodisyndiotactic (racemic) or erythroatactic sequences (random) with specific isomeric stereoregular tetrades as shown in Fig. 3.1 [100, 71]. The investigation of structure-property relationships for these isomeric sequences has long been sought with an assortment of theories, experiments, and simulations to overcome the challenges present in the processing of these polymeric materials.

Haselwander *et al.* [7] reported vinylic polymerization of norbornenes with Pd^{2+} complexes that produces amorphous, high T_g, soluble polymers with a characteristic ratio (C_∞) of 11.4. To gain further insight, they performed *ab initio* AM1 and STO-3G rotational potential calculations around the bond linking a racemo dimer and Rotational Isomeric State (RIS) computations of ~ 160 repeat units that resulted in $C_\infty = 12.1$. Short (450 ps) simulations of single chains with $N = 100$ using the Dreiding forcefield [101] resulted in a lower value of C_∞=8.5 [102] which could be attributed to the inclusion of long-range interactions in a poor solvent (vacuum) or to a lack of higher-order correlations in the earlier RIS calculations. Two-dimensional rotational potentials using successive rotatable bonds as well as dihedral distributions calculated suggested that such correlations can be important for PNB. Furthermore, simulations by Haselwander *et al.* [102] emphasized the need for a large number of repeat units to reach polymer-like behavior free of chain-end effects and reported rotational jumps at temperatures higher than 800 K with the onset of free rotations at 1600 K. Similar results were also reported when recording nanosecond-long trajectories at 600 K in the condensed phase which also produced a change in the specific volume around 478 K, suggesting the presence of T_g [103].

Ahmed *et al.* [6] derived atomistic (AA) forcefields for PNB by using *ab initio* calculations and semi-empirical methods in model dimers to characterize bond, angle bending, and rotational potentials separately for meso and racemo PNB, while supplementing

intermolecular interactions with Lennard-Jones parameters from the Dreiding forcefield. While high-stiffness terms were initially proposed, subsequent work by Wilks *et al.* [96] proposed that the angle force constants were over-estimated and opted for standard Charmm parameters [104]. The extracted rotational potentials were implemented in Monte Carlo simulations of single chains in vacuum for meso, racemo, and 50/50 atactic copolymer. They reported that the meso polymer resembles a rigid rod and the racemo is semi-rigid, while the conformation of the atactic chain appears closer to a random coil. These data were qualitatively compared to the experimental intrinsic viscosity of PNB and its alkane derivatives synthesized with different catalysts. They postulated that the intractable polymers produced by Pd catalysts have high-meso sequences (assuming no impact of hydrocarbon side chains on polymer conformation). RIS calculations with single chains consisting of the meso isomer predicted an incommensurate helix with successive dihedrals of 200°. This model polymer was close to a rigid rod although kinks could appear in sufficiently long chains [105, 106]. Polarimetric measurements of PNB polymerized with zirconium catalysts did not show an increase in the optical activity of the polymer compared to the monomer, which could indicate a lack of helix formation, assuming that the poor solubility of polymer does not affect this result [107].

In this study, we use molecular dynamics (MD) simulations to directly correlate the bulk properties of PNB with its stereochemistry. We optimized the Williams7B forcefield [1] based on density functional theory (DFT) calculations of trimers to represent PNB with an AA model and consequently derived a coarse-grained (CG) model to perform melt simulations of PNB. The minimized DFT energies and structures for PNB dimers and trimers were provided by our collaborators, Jeffrey A. Laub and Dr. Konstantinos D. Vogiatzis. Our simulations show that increasing the ratio of meso dimers results in longer chains with faster dynamics. We show that the all-racemo chains adopt a helical structure with slower dynamics. Although we did not observe crystallization by cooling the system, these results are in agreement with experimental observations that predict a helical structure for PNB synthesized with a certain catalyst [108].

3.2 Method

3.2.1 Atomistic simulations

MD simulations were performed with the GROMACS package [53] (version 2019.6) using the Williams7B forcefield with modified dihedrals for the PNB backbone (details in Sec. 3.3 3.3.1). The parameters for the original Williams7B and the new dihedrals for PNB backbone are displayed in Table 3.2. We used a cut-off of 1 nm for van der Waals interactions with dispersion corrections for energy and pressure calculations. The simulations were performed with a timestep of 1 fs and bonds with hydrogen atoms were constrained using the Lincs algorithm [109]. Production runs were performed in the canonical (NVT) ensemble using the velocity re-scaling thermostat [59]. Densities were calculated from isothermal–isobaric (NPT) simulations using the Parrinello-Rahman barostat [110] while annealing and the initial equilibration NPT runs were performed with the Berendsen barostat [52]. Dimer and trimer energy minimization was performed with double precision GROMACS using the steepest descent algorithm and convergence tolerance of 1 kJ.mol−1.nm−1. The melt PNB systems studied with the AA model are summarized in Table 3.1 and include different chain lengths and backbone isomers. In the atactic systems, each chain has a specific ratio of meso and racemo dimers in a random sequence.

3.2.2 Coarse-graining method

The coarse-grained model consists of two bead types as shown in Fig. 3.2. Each monomer has a bead (CGS) at the center of the non-backbone carbons (C_1, C_4, C_5, C_6, and C_7). The other bead (CGB) is placed in the middle of the C_3-C_2 bond that connects two consecutive monomers. The forcefield includes different types of bond, angle, dihedral and nonbonded potentials (14 in total) which are assumed to be decoupled. Nonbonded interactions for neighbors up to 3 bonds away are excluded. The total potential is described as $U_{\text{total}} = U_{\text{bond}}(l) + U_{\text{angle}}(\theta) + U_{\text{dihedral}} + U_{\text{nonbond}}$.

We employed the iterative Boltzmann inversion (IBI) method [111, 112] to reproduce the probability distribution of each term (P_α^{target}) as derived from the mapped AA simulations

at 800 K and 1 bar. We employed the same CG representation for all tacticties and derived the target distributions and the CG forcefield separately for each activity, which resulted in different forcefields as demonstrated in Sec. 3.3.1. The initial potentials were the Boltzmann inverted potentials of mean force $U_\alpha^0 = -k_B T \ln P_\alpha^{\text{target}}$. At each iteration after performing the CG simulation in the NVT ensemble, potentials were updated by $U_\alpha^{i+1} = U_\alpha^i + \gamma k_B T \ln (P_\alpha^i / P_\alpha^{\text{target}})$ (γ in the range of 0.1–0.3). To accelerate the optimization process, we updated different potentials simultaneously when possible, and applied the successive optimization in multiple cycles as proposed by Reith *et al.* [23] when necessary. Matching AA conformational and structural distributions at target density often produces a CG forcefield that overestimates pressure by several orders of magnitude. We observed similar results and performed additional optimization of nonbonded potentials to produce the correct pressure by adding an attractive linear tail in each iteration $\Delta U_{\text{nonbond}} = A(1-r/r_{cut})$ [23]. Since this affects the distributions, we performed additional cycles of optimization to match both the distribution and pressure. The initial optimization was performed with $N = 22$ chains using PNB-N22 distributions as the target. Due to the chain end effects, the distribution and density depend on chain length and the initial CG model did not show adequate transferable for higher N, therefore, we performed additional optimization with $N = 30$ chains using target distributions from PNB-N30. Subsequently, CG simulation of PNB-N41 was used to validate the model and the meso system was re-optimized with PNB-N41. In addition to the target distributions, the CG-PNB model accurately predicted the chain conformation.

CG simulations were performed with GROMACS using tabulated potentials with a timestep of 0.5 or 1 fs and a cut-off of 1.5 nm. Simulations for IBI were performed in NVT and production runs were performed in the NPT ensemble using the velocity re-scaling thermostat and the Parrinello-Rahman barostat.

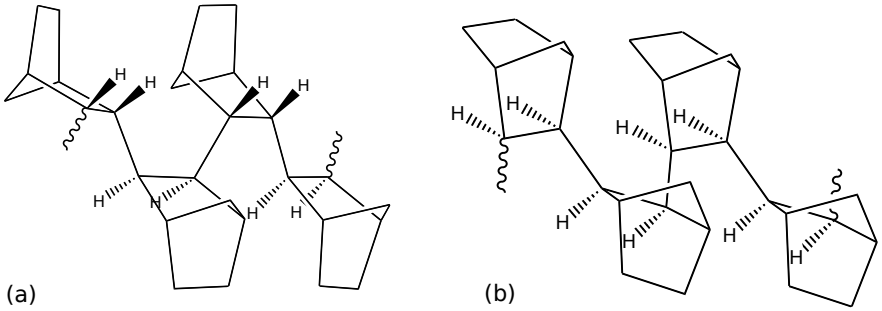


Figure 3.1: Stereoregular isomers of PNB with 2,3 polymerization: a) erythro di-isotactic (meso) and b) erythro di-syndiotactic (racemic). Backbone hydrogens are drawn to note the *exo*-polymerization followed.

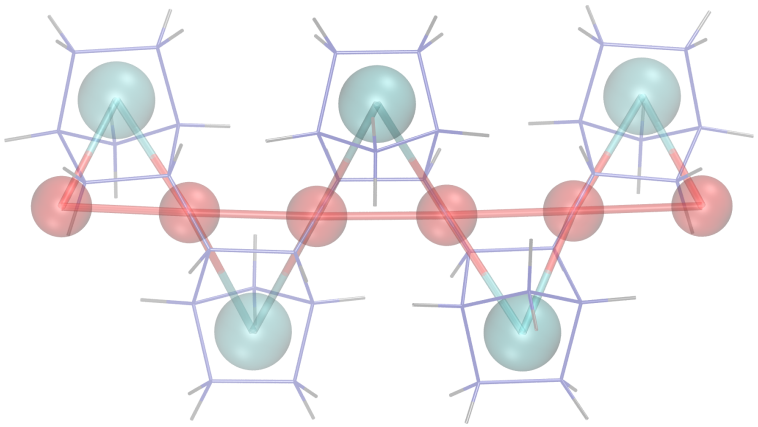


Figure 3.2: Mapping schematic for CG-PNB. Each monomer has a bead in the middle of the backbone bond (C_2-C_3) connecting it to the next monomer (red, CGB) and a bead in the middle of the other 5 ring carbons (cyan, CGS). Each CGB bead is bonded to the consecutive CGB bead as well as the middle CGS bead.

Table 3.1: Studied systems include 4 different backbone tacticities with a random sequence of meso and racemo dimers at different chain lengths.

system	% of racemo dimers	chain length/number of chains	T (K)
meso	0	10/25, 22/40, 30/50, 41/55	800 K
random 50	50	10/25, 22/40, 30/50, 41/55	800 K
random 75	75	10/25, 22/40, 30/50, 41/55	800 K
racemo	100	10/25, 22/40, 30/50, 41/55	800 K

Table 3.2: The parameters for Williams7B [1] forcefield with bonded parameters originally taken from CHARMM forcefield [2] and dihedral parameters from Tu et al. [3]. Meso and racemo backbone dihedrals (C_2-C_3-C_2-C_3) were optimized for PNB (this work).

nonbonded potential $V_{\mathrm{nb}}(r) = A\exp(-Br) - C/r^6$			
pairs	A (kJ/mol)	B (nm^{-1})	C (nm^6.kJ/mol)
C-C	3.4186×10^5	36.94	2.005×10^{-3}
C-H	0.5814×10^5	37.61	0.507×10^{-3}
H-H	0.1365×10^5	38.30	0.128×10^{-3}

bond potential $V_{\mathrm{b}}(b) = 1/2k_b(b - {b_0}^2)$		
bonds	b_0 (nm)	k_b (nm^2.kJ/mol)
C-C	0.153	224262.4
C-H	0.104	284512.0

angle potential $V_{\mathrm{a}}(\theta) = 1/2k_\theta(\theta - {\theta_0}^2)$		
angles	θ_0 (deg.)	k_θ (rad^2.kJ/mol)
C-C-C	113.7	488.273
C-C-H	109.2	313.800
H-C-H	106.0	276.144

dihedral potential $V_{\mathrm{d}}(\phi) = \sum_{n=1}^{3} k_n(1 + \cos(n\phi - \phi_n))$						
dihedrals	k_1 (kJ/mol)	k_2	k_3	ϕ_1 (deg.)	ϕ_2	ϕ_3
C-C-C-C	0.9791	0.4017	1.7154	0	0	0
C-C-C-H	0	0	0.7406	0	0	0
H-C-C-H	0	0	0.6904	0	0	0
meso	-1.3072	0.9035	-3.2567	-159.0	8.6	-4.3
racemo	3.2241	-1.2080	-2.2806	-0.9	180.0	1.0

3.3 Results

3.3.1 Forcefield optimization

Atomistic forcefield

Previous simulation studies have demonstrated that general AA forcefields do not accurately describe PNB due to the high strain and restricted rotation in the bicyclic backbone [7, 6, 40]. Following the literature, we initially evaluated the performance of several forcefields in describing minimal energies of dimer structures under dihedral constraints for the main flexible torsion along the backbone (C_2-C_3-C_2-C_3). DFT energies and structures were provided by our collaborators, Jeffrey A. Laub and Dr. Konstantinos D. Vogiatzis, and as shown in Fig. 3.3 are in good agreement with semiempirical calculations for the two different stereoisomers. We calculated the energy barriers for backbone rotation using several AA forcefields including OPLS-AA [8], Amber99sb [9] and Williams7B [1], which all overestimated the energy, particularly for dihedral angles around the maximum energies.

While rotational potentials for dimers have been used in past studies to develop and validate classical forcefields, we found that for PNB, DFT calculations for trimers are necessary. The trimer energy maps show a high correlation between consecutive dihedrals and several combinations of two neighboring C_2-C_3-C_2-C_3 dihedrals can lead to major steric overlaps between hydrogen atoms of the first and third repeat unit (see Fig. 3.1) that result in high barriers. Fig. 3.4 presents the difference between energies calculated with DFT and three different sets of interaction parameters.

The OPLS and Amber99sb forcefields severely overestimate the energy, especially for highly strained configurations of trimers. These forcefields include the common 12-6 Lennard-Jones nonbonded potential which is known to be too repulsive at short distances [113, 114]. In contrast, Williams7 [115] and Williams7B forcefields that use the exp-6 Buckingham potential (reported to provide a more accurate repulsive interaction [116, 117, 118, 119, 1]) produced the best match with DFT results.

In this work, we adopted the updated Williams7B forcefield that has displayed higher accuracy in predicting the diffusion coefficients and density of oligomers [1]. We performed

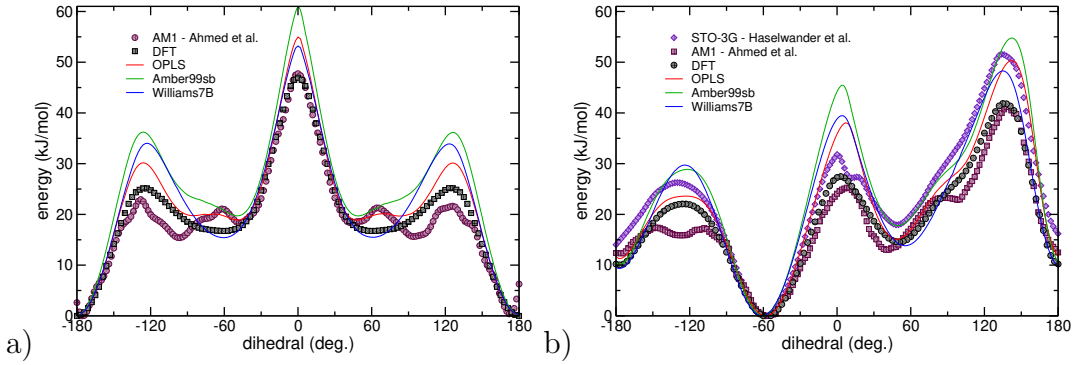


Figure 3.3: Energy barriers for rotation of backbone dihedral (C2-C3-C2-C3) of a) meso and b) racemo dimers. The DFT calculations are compared with data from literature calculated using the AM1 semiempirical method [6] and STO-3G *ab initio* quantum mechanical calculations [7]. Dashed lines show results from MD simulations performed with different forcefields: OPLS-AA [8], Amber99sb [9] and Williams7B [1].

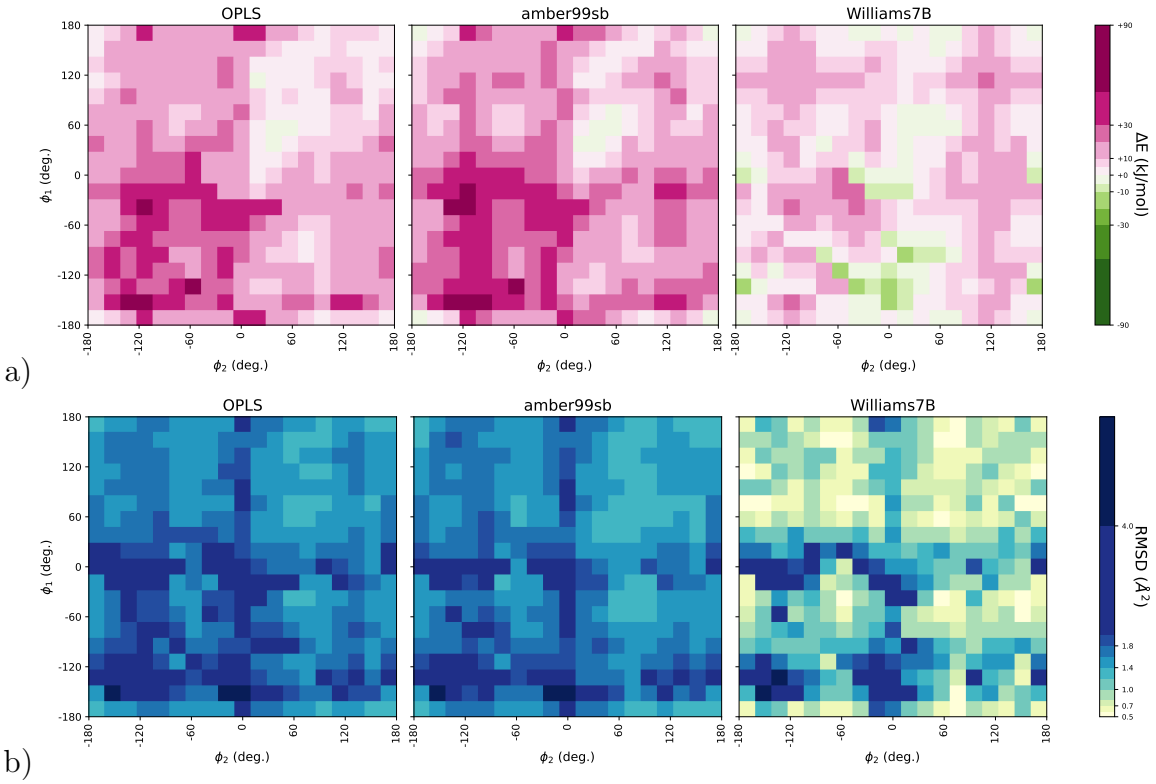


Figure 3.4: a) The energy difference between DFT and classical MD forcefield minimum states for meso-racemo trimers as a function of two successive backbone (C_2-C_3-C_2-C_3) dihedrals (ϕ_1 and ϕ_2) evaluated with different forcefields. Left-to-right: OPLS-AA [8], Amber99sb [9] and Williams7B [1]. b) Root mean square deviation (RMSD) between MD structures after energy minimization and DFT structures used as the initial state.

additional optimization of the meso and racemo backbone dihedral potentials to match the meso-meso and racemo-racemo DFT energies. As shown in Fig. 3.4, the obtained potentials for meso and racemo backbone dihedrals provided a good description for the meso-racemo energy map.

The two-dimensional rotational potentials of trimers shown in Fig. 3.5 indicate high coupling between the dihedral energies of consecutive monomers. For increased accuracy, we used the trimer potentials in the optimization of the AA forcefield (Sec. 3.3.1). Unlike the melt systems, the DFT trimers include a percentage of endo polymerization. The high rotational energy barriers of trimers are consistent with the reported high rigidity of the PNB backbone. All backbone tacticities show a high-energy region around the zero-zero dihedral conformation and have minimum energies at the trans-trans conformation. The meso-racemo trimer shows significantly lower energies with various high-probability conformations while the racemo-racemo tacticity has the lowest density of low-energy conformations.

Coarse-grained model

Fig. 3.6 shows the nonbonded potentials and the corresponding nonbonded radial distribution functions ($\mathrm{rdf_{nb}}$) for the three CG-PNB systems: all meso, all racemo and random 50:50. The optimization results show that the three nonbonded potentials are strongly coupled and composition dependant. Fig. 3.7 shows the backbone bonded potentials and the corresponding distributions between CGB beads in different systems. The CG-PNB models for the racemo and random systems produce a satisfactory description for all bonded distributions, while the meso model overestimates the probability of higher bond length and angle values of backbone beads.

3.3.2 Thermodynamic properties and structure

The random 50 and 75 systems both have a specific volume (V_{sp}) that is similar to the meso system at short chain lengths while the racemo system displays a significantly lower V_{sp}. At the small length of $N = 10$, the racemo chains have a more near collapsed conformation (see Sec. 4.3.2), which results in a high free volume. At the high chain length of $N = 100$, the

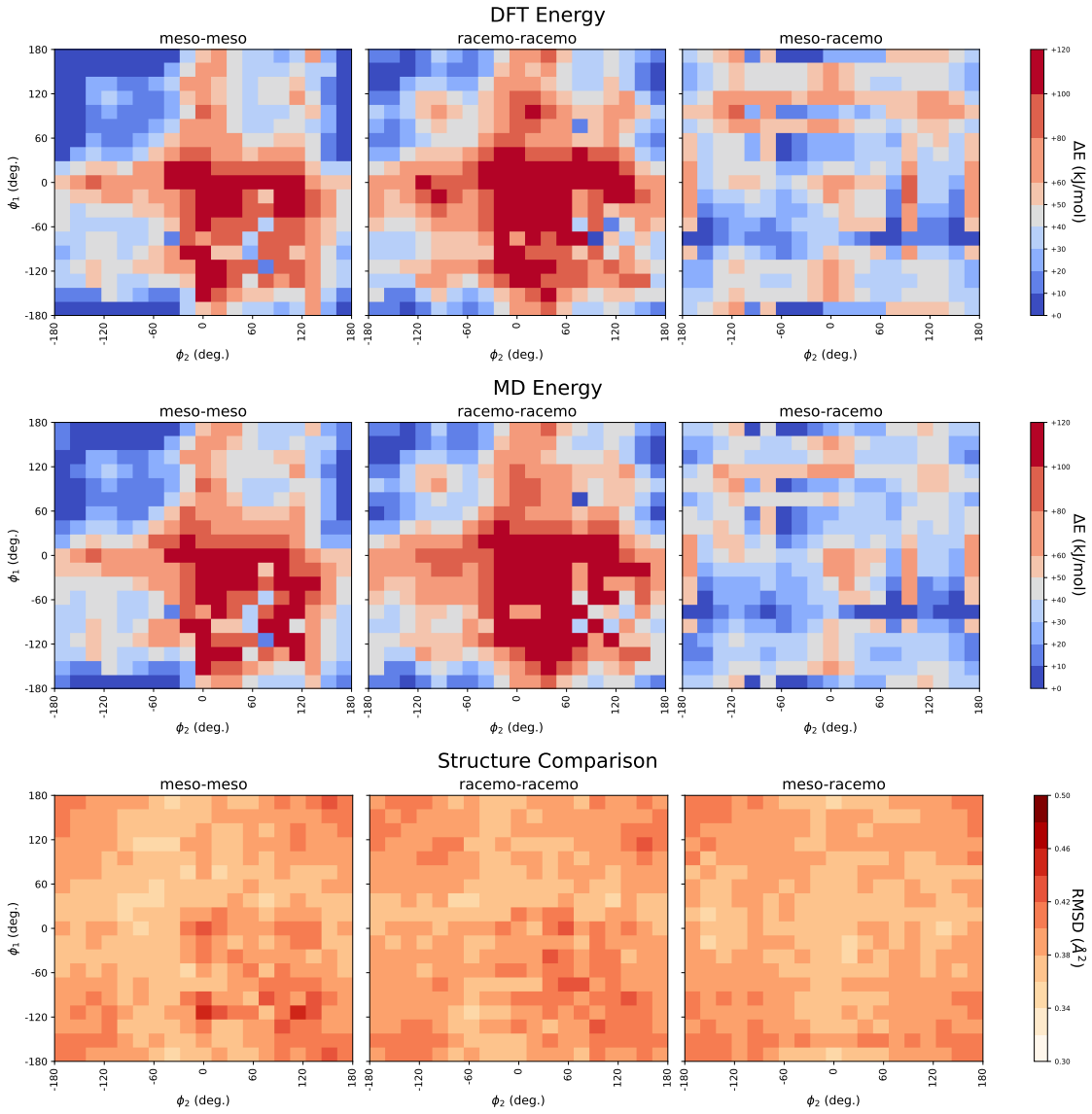


Figure 3.5: Rotational energy maps of trimers from DFT calculations by Jeffrey A. Laub and Dr. Konstantinos D. Vogiatzis and our MD simulations using Williams7B [1] with optimized backbone dihedrals for the meso-meso, racemo-racemo, and meso-racemo tacticities. The bottom row displays the RMSD of minimum MD structures from DFT structures.

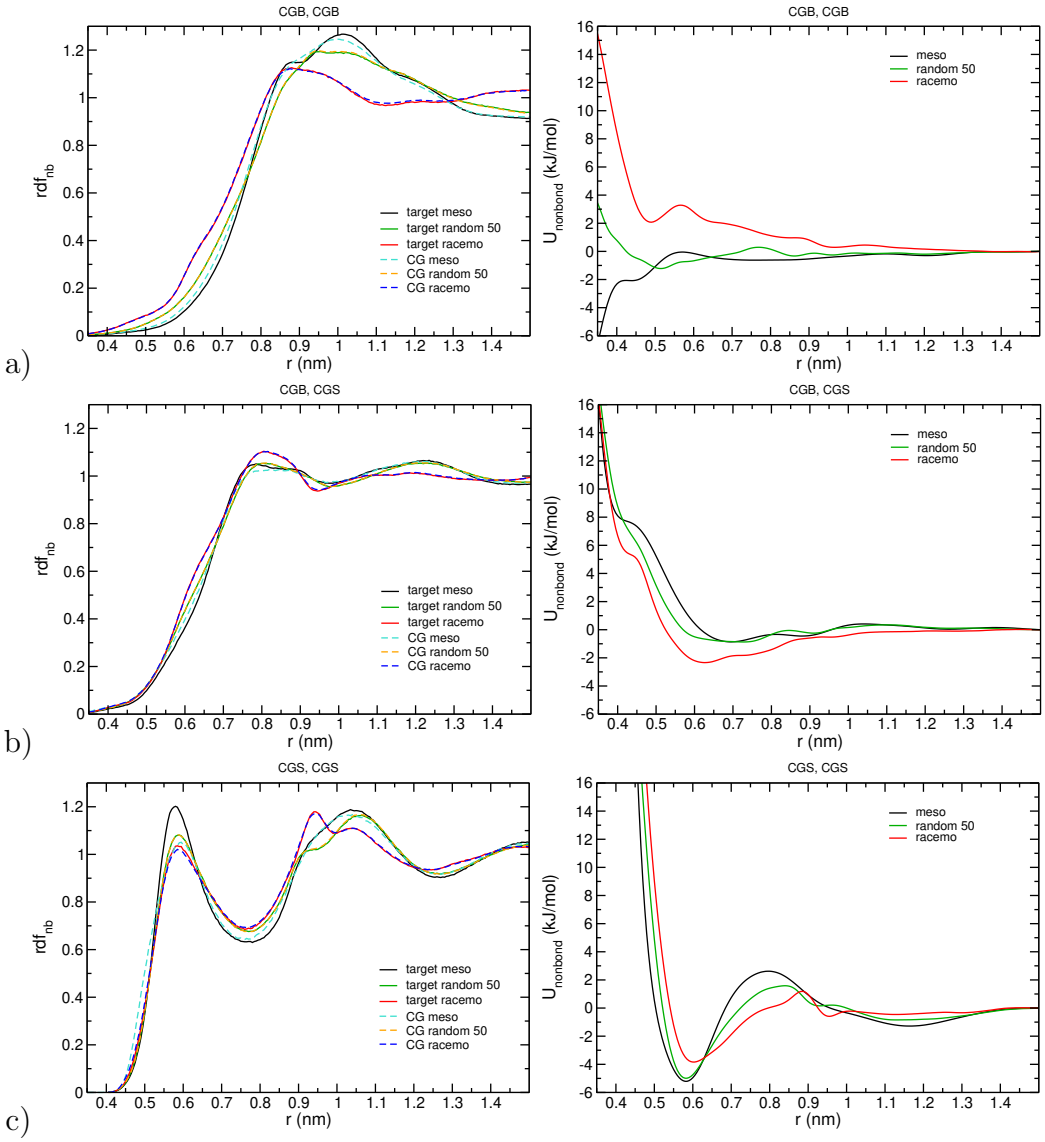


Figure 3.6: The CG-PNB nonbonded radial distribution function ($\mathrm{rdf_{nb}}$) compared with AA target (left) and the optimized CG-PNB nonbonded potentials (right) for: a) CGB-CGB, b) CGB-CGS and c) CGS-CGS. The forcefields were optimized separately for the following systems: meso with $N = 41$, random 50, and racemo with $N = 30$ at 800 K.

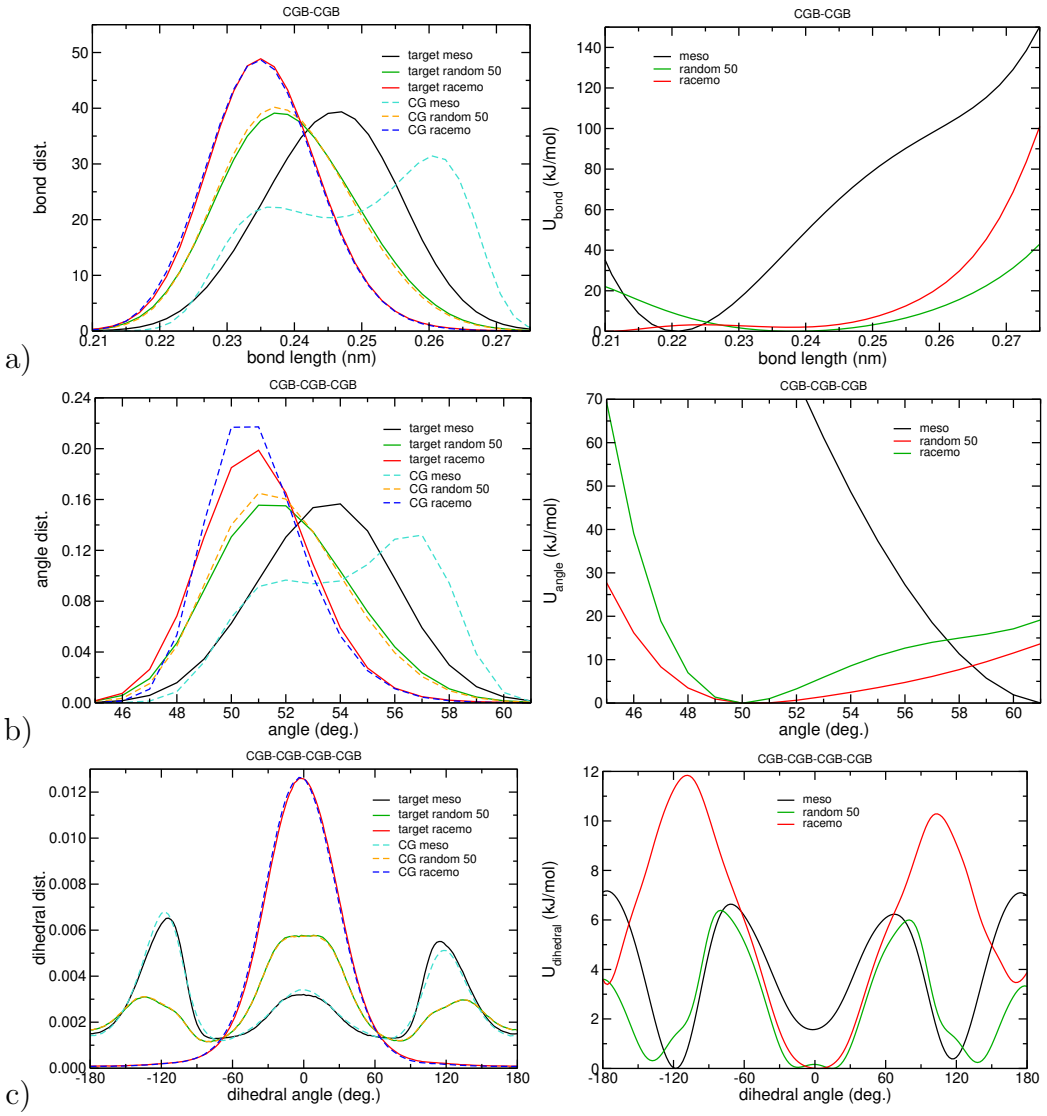


Figure 3.7: The bonded distribution functions for the backbone CGB bead compared with their AA target (left) and the corresponding bonded potentials (right): a) bond, b) angle, and c) dihedral.

CG model shows that the random 50 and racemo systems follow a similar trend, while the meso V_{sp} drops significantly. This is the subject of ongoing work and could be due to the rigid structure of long meso chains at high M_w that enables denser packing.

Fig. 3.8 shows the change in specific volume while cooling PNB-N30 systems at a rate of 2 K/ns. Although the racemo systems have a significantly higher density at 800 K, near T_g and in the glassy state the densities become similar for different tacticities. We observe a broad range of possible T_g values since the thermal expansion coefficient does not change dramatically between melt and glassy states. A similarly weak transition is observed in experimental ellipsometry measurements [75]. Although we observe different dynamics for different tacticities at 800 K (Sec. 3.3.4), all systems show a similar T_g within the observed error. Some experimental reports have observed crystallization for short oligomers with racemo [108] and syndiotactic meso-racemo tacticity [120] which we did not observe, possibly due to the high cooling rate used in simulations. We are simulating short chains compared to the high molecular weights typically used in experiments and therefore we expect our melts to have a lower T_g [121]. However, the high cooling rate used in simulations results in overestimation of T_g [122, 123, 124] which makes direct comparison with experimental data difficult. The observed T_g values of 615 K are similar to the reported value of 658 K [83]. The obtained densities for PNB-N22 at 300 K are $\sim$ 1.04 g/cm^3 for all tacticities which is in agreement with the reported value of 1.065 g/cm^3 [10].

Fig. 3.9 shows the calculated X-ray scattering patterns. The position of the peaks predicted by our model is in good agreement with experimental data [10] which exhibited an amorphous structure. All PNB tacticities have similar peak positions, with high racemo content resulting in broader signals and high meso content resulting in higher intensity in the first peak. Based on the carbon-carbon pair density (g_{CC}), in all systems, the position of the neighbor shells is similar across different tacticities. The density of the bonded pairs at distances below the first intra-molecular neighbor shell which is responsible for the position of the high q peak is similar across different tacticities. Above the first inter-molecular neighbor shell, the racemo system has a higher density of intra-molecular neighbors and a longer distance to reach melt density which results in the shift of the first peak to lower q as the ratio of racemo dimers increases.

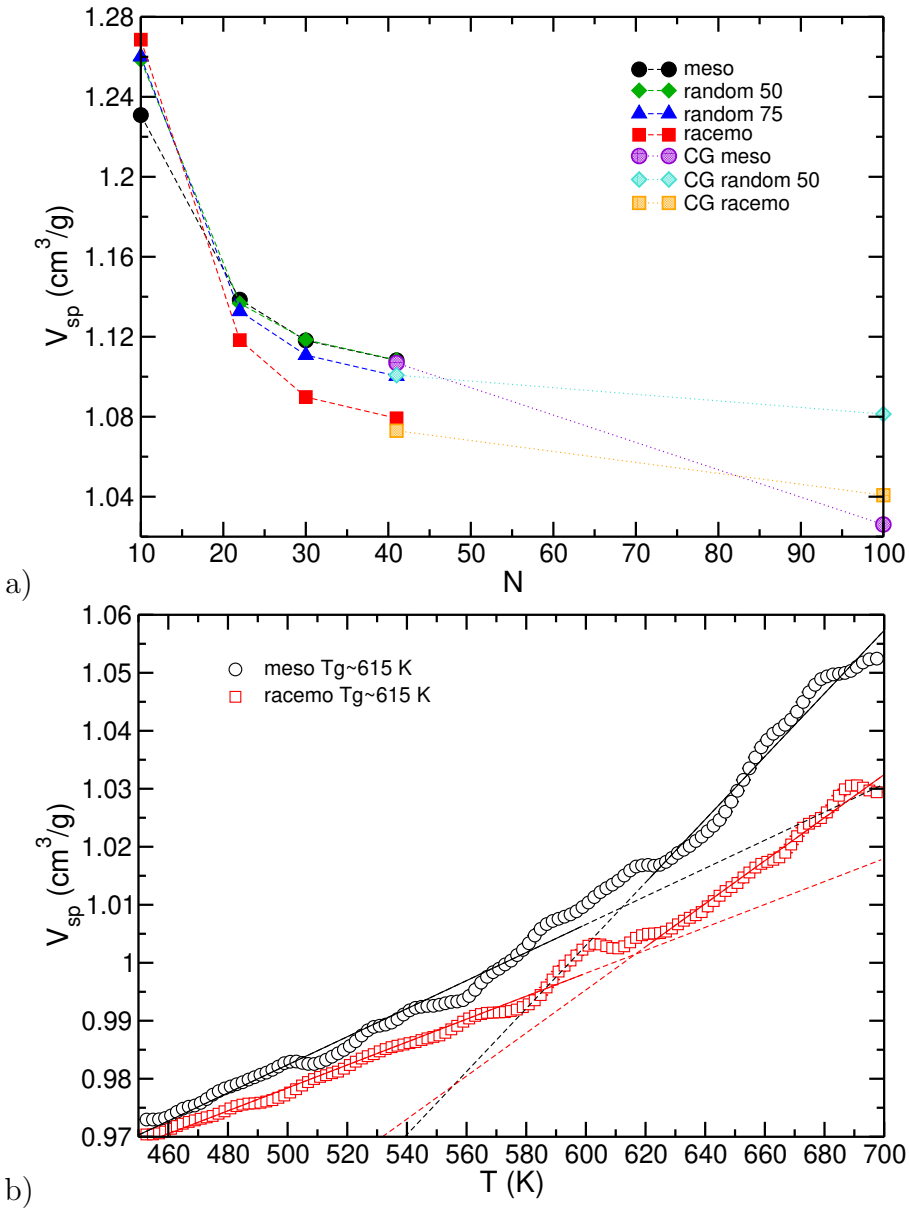


Figure 3.8: a) Specific volume (V_{sp}) of PNB as a function of chain length from AA and CG simulations at 800 K. b) V_{sp} with temperature and T_{g} at the cooling rate of 2 K/ns for PNB-N30. Each point represents the average over a 2 K range (5000 points). Solid lines mark the linear fit to the melt and glass regimes. Dashed lines represent the intersections of linear fits that correspond to Tg.

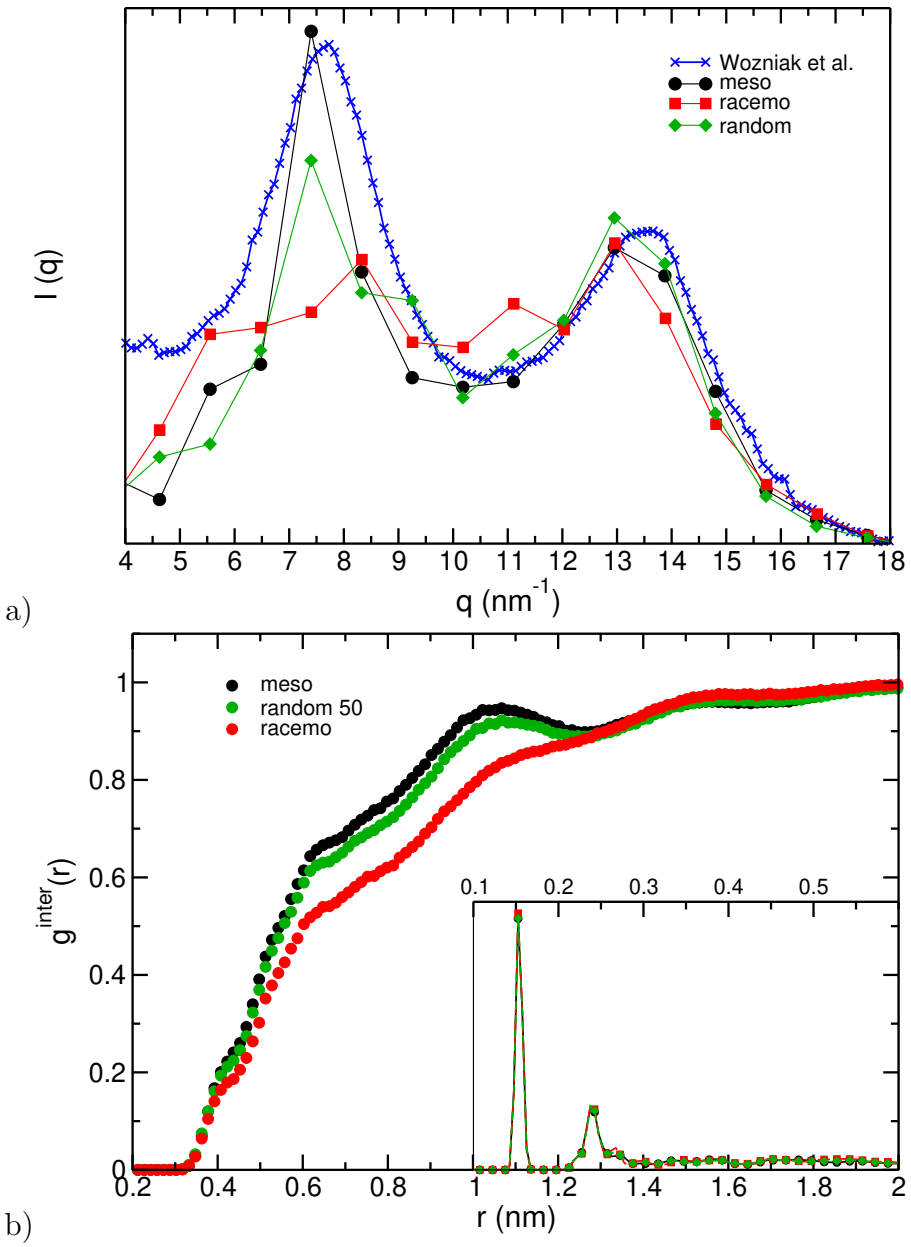


Figure 3.9: a) X-ray scattering patterns calculated for PNB-N22 at 300 K (from the cooling ramp of 10 K/ns starting from 800 K) compared with WAXS experimental data with unknown tacticity from Wozniak et al. [10] ($\lambda = 0.154$ nm). b) Intra-molecular and inter-molecular radial distribution function of carbons (g_{CC}).

3.3.3 Chain conformation

Fig. 3.10 shows the correlation of the C_2-C_3 bond vector along the chain (corresponding to $\langle \cos\theta \rangle$ where θ is the angle between the tangent vectors at monomer i and $i + \Delta n$ along the chain) which drops to zero at sufficiently long distances where the conformational correlations are lost. In random coils, this function follows an exponential decay and is used to calculate the persistence length. The presence of repeated peaks for racemo chains is due to their helical structure and indicates a pitch of $n = 5$. Experimental results of racemo oligomers have similarly observed a tubular helical structure [108]. Additional test simulations with OPLS-AA forcefield similarly indicated the presence of helical structure only for the racemo tacticity. Unlike previous predictions of helicity for meso chains by Ahmed *et al.* [105], we observed a rigid rod-like conformation in meso chains. Since the chains are not perfect rigid helices, the correlation function approaches zero at longer distances. The intra-chain characteristic ratio (C_n) shows that chains with a higher content of meso dimers are longer while racemo chains are shorter and exhibit an additional minimum due to their secondary structure. The random 75 system has a similar size as the purely racemo chains but it does not display a significant degree of helicity.

All tacticities show a linear relationship between $\langle {R_e}^2 \rangle$ and chain length (N). As N increases, the conformation of the random 50 chain starts to resemble a random coil ($\langle {R_e}^2 \rangle / \langle {R_g}^2 \rangle$ approaches 6) while the meso chain retains its rod-like conformation and its size increases significantly. Due to its secondary structure, the racemo chains are smaller, especially at very low M_w where the $\langle {R_e}^2 \rangle / \langle {R_g}^2 \rangle$ value is similar to a collapsed chain. As chain length increases from short oligomers to longer polymers, the racemo chains lose their helical structure, and more kinks form in the backbone which allow for more conformational states and smaller peaks in the bond correlation function.

3.3.4 Dynamics

The autocorrelation function $\left(C(t) = \frac{\langle \vec{V}(t)\vec{V}(0) \rangle}{\langle \vec{V}^2(0) \rangle} \right)$ of the bridge vector (middle of the C_2-C_3 backbone bond to the C_7 bridge carbon) and chain end-to-end vector are used quantify the segmental and chain dynamics respectively and displayed in Fig. 3.13. For PNB-N10 the

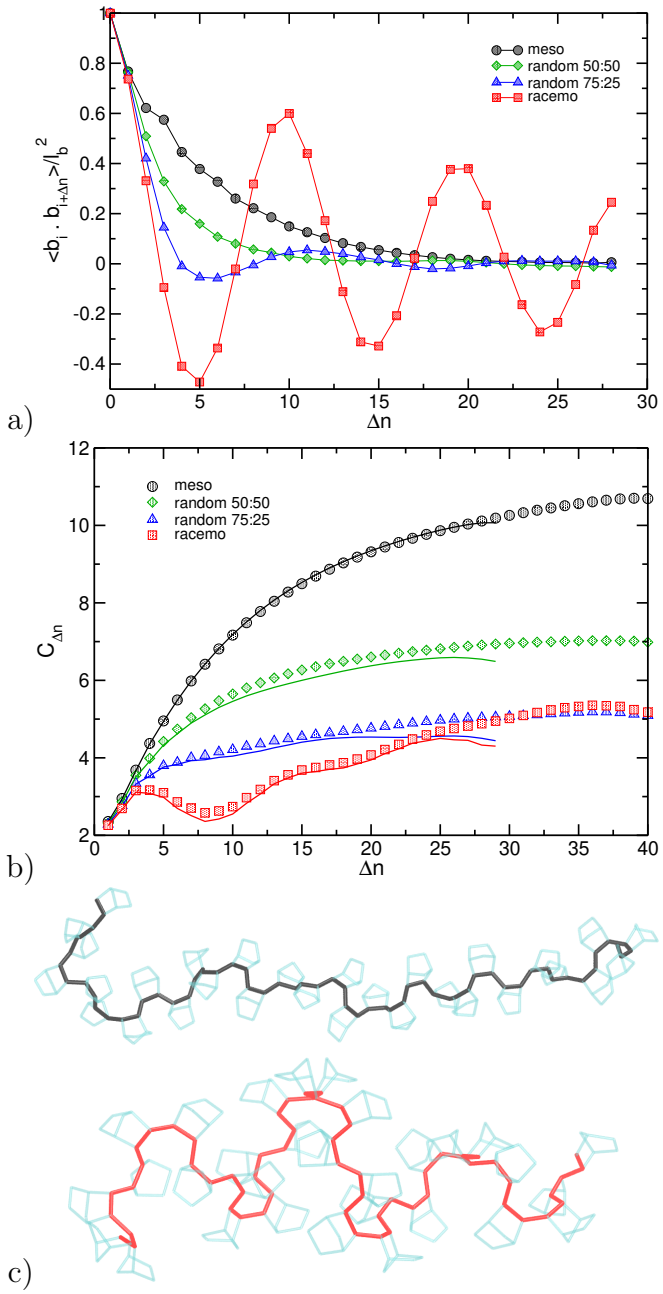


Figure 3.10: a) Normalized correlation of the C_2-C_3 bond vector (with length l_b) for PNB-N30 and b) characteristic ratio ($C_{\Delta n} = < R_e^2(\Delta n) > /2(\Delta n + 1)l^2$ with $l = 1.53\,\text{Å}$) as a function of monomer distance (Δn) for PNB-N30 and PNB-N41 at 800 K. c) Schematic representation of a meso (top) and a racemo (bottom) PNB-N30 chain at 800 K.

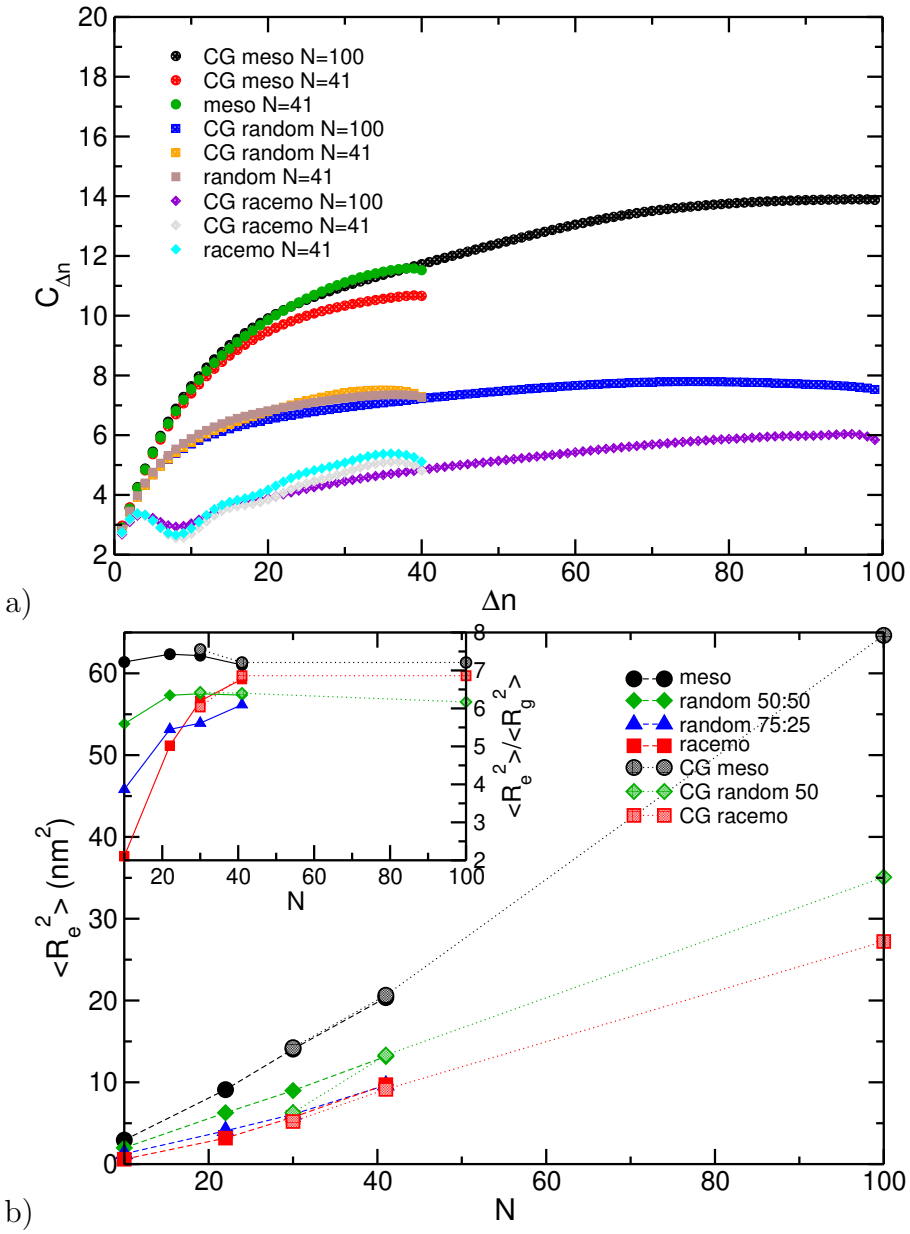


Figure 3.11: a) characteristic ratio as a function of monomer distance using AA and CG models. b) Mean squared chain end-to-end distance ($\langle {R_e}^2 \rangle$) as a function of chain length. Inset shows ratio of $\langle {R_e}^2 \rangle$ over mean squared radius of gyration ($\langle {R_g}^2 \rangle$) for different chain lengths (N) at 800 K. c) Normalized correlation of the C_2-C_3 bond vector for racemo chains. d) Schematic representation of racemo CG-PNB chain with $N = 100$.

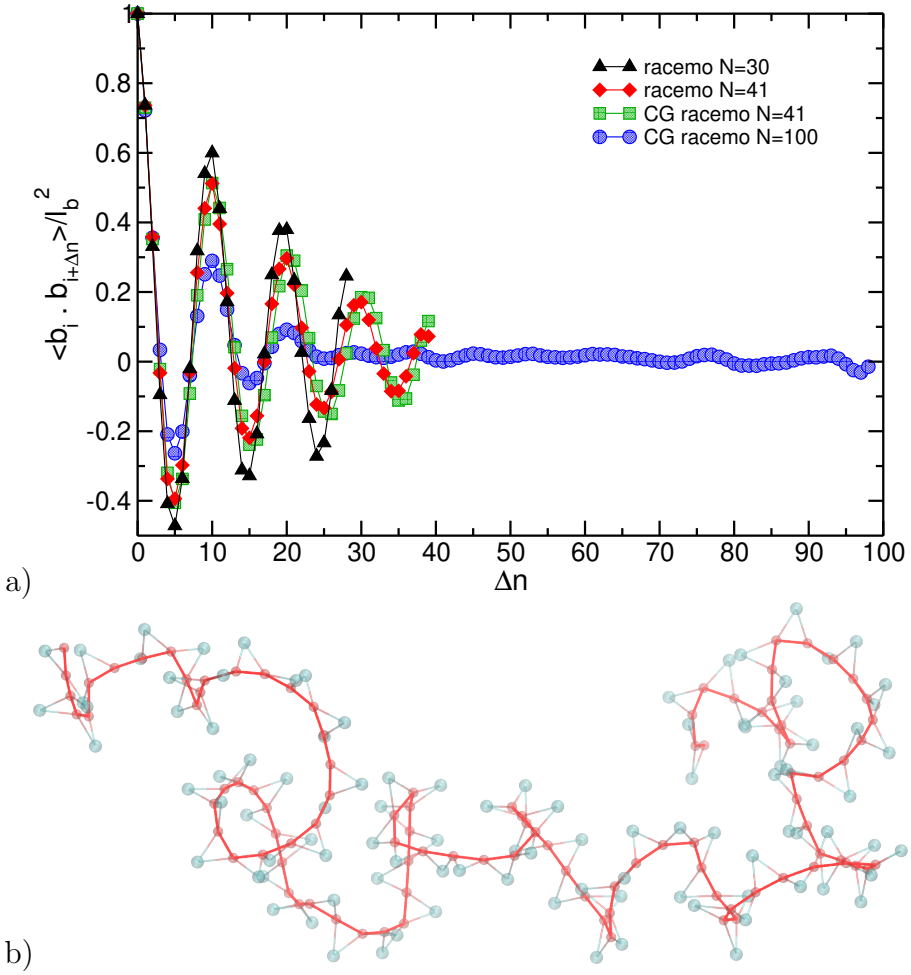


Figure 3.12: a) Normalized correlation of the C_2-C_3 bond vector for racemo chains sing AA and CG models. b) Schematic representation of racemo CG-PNB chain with $N = 100$.

meso system has faster segmental dynamics while the random and racemo systems are similar. However, the end-to-end autocorrelations are similar across meso and random systems and significantly lower in the all-racemo system. Mean squared displacement (MSD) of the chain center of mass shows faster self-diffusion for chains with a higher ratio of meso dimers, with significantly slower dynamics for the racemo system $N = 100$.

3.4 Conclusions

We employed MD simulations to directly examine of the effect of stereochemistry on the properties of PNB. We first examined the representability of different AA forcefields and optimized the backbone dihedral potential of Williams7B to better match DFT rotational energy barriers of trimers and consequently developed a coarse-grained model for different tacticities. The results from melt simulation show that racemo chains show a degree of helicity that decreased at higher M_w, while meso chains became more rigid. As the ratio of meso dimers in the chains increases, so does the chain size while the dynamics become faster.

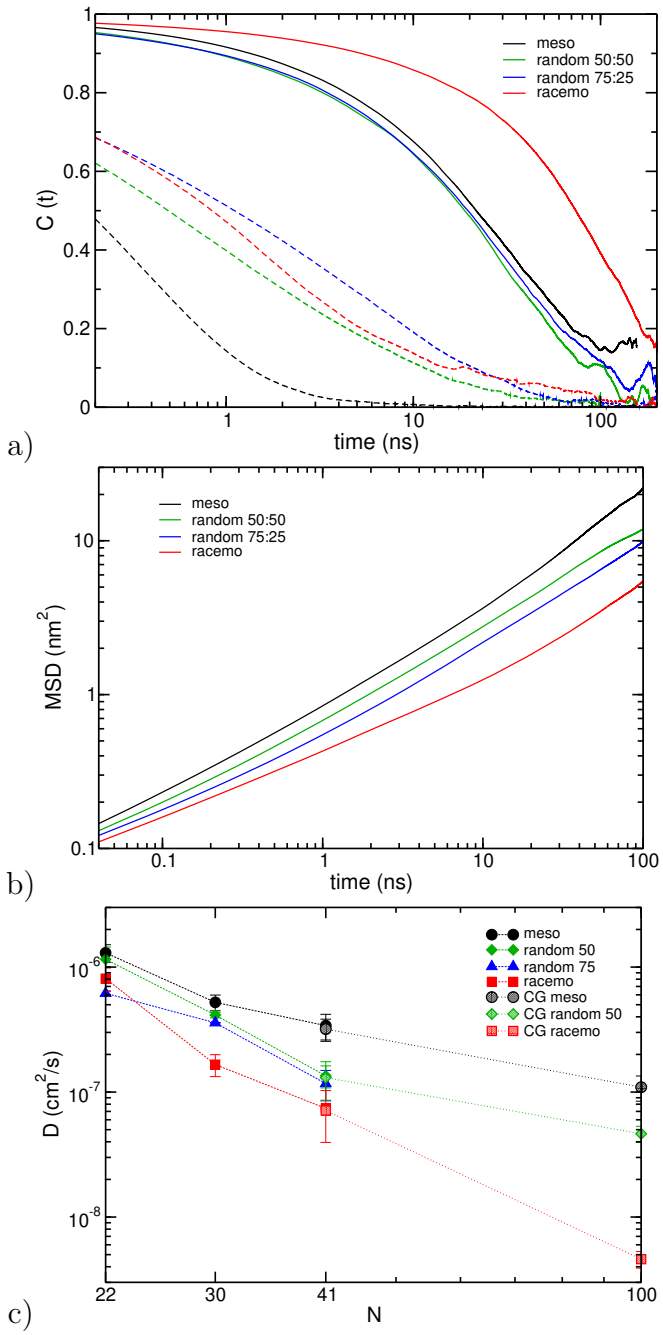


Figure 3.13: a) Autocorrelation of end-to-end vector (solid lines) and bridge vector (dashed lines) from the middle of C2-C3 to C7 and b) Mean square displacement (MSD) of chain center of mass for PNB with $N = 41$ at 800 K. c) Diffusion coefficient (D) of different PNB tacticities as a function of chain length. CG values are scaled to match AA values at $N = 41$.

Chapter 4

Effect of alkyl side chains on structure-property relationships of vinyl-addition polynorbronenes

4.1 Introduction

Thermal and mechanical properties of rigid vinyl-addition polynorbornenes (PNB) can be fine-tuned by the addition of functional groups. Flexible side chains lower the glass transition temperature (T_g) [91] and improve toughness and adhesion [83], as well as gas selectivity and permeability [78, 80, 92, 81, 93]. Alkyl side chains, in particular, have been shown to produce promising engineering thermoplastics due to their improved melt processability, film-forming ability, and toughness [94, 95, 75]. Another method for improving the properties of PNB is copolymerization with alkenes such as ethene [99] and propene [125] to produce cyclic olefin copolymers (COC). COC are engineering thermoplastics that have been commercialized by various manufacturers and are suitable for a wide range of applications in packaging, medical appliances, optics, capacitors, and microfluidic devices [126, 127]. Properties of alkyl-substituted PNB or COC such as T_g, ductility, gas permeability, and selectivity can be further optimized based on the length of the alkyl side chain [96, 10].

Experiments show that as the length of the alkyl side chain increases, T_g and density decrease and fractional free volume increases [96, 10, 95]. This internal plasticization effect from the addition of flexible side chains is due to an increase in free volume and configurational entropy. This is predicted by generalized entropy theory of glass formation for polymers with stiff backbones and flexible side chains [128, 129, 130] and has been observed experimentally in numerous systems such as conjugated polymers [130] and branched and bottle brush polymers [131, 132]. It is well understood that the stereochemistry of polymers plays an important role in determining their physical properties and is a requisite for material design [133]. However, determining the tacticity of the bicyclic norbornene backbone is difficult in the presence of pedant groups [72]. To the best of our knowledge, the effect of stereo-chemistry has not been directly studied by experimental methods (such as ^{13}C NMR analysis used for COC [125]) for PNB with alkyl side chains.

Previous computational studies of PNB have focused on the effect of tacticty on the conformation of unsubstituted chains by using the Rotational Isomeric State (RIS) model or single chain simulations [7, 134, 6, 135, 105, 106]. More recently simulations of bulk polymers have been used for the more flexible COC [136, 137] and PNB with silica side chains [138]. Wilks *et al.* [96] used room temperature simulation of bulk PNB with alkyl side chains to study the glassy state. Here, we study the effect of microstructure and stereochemistry in alkyl-substituted PNB by employing simulations in the condensed state.

4.2 Simulation details

Simulations were performed with GROMACS [53] 2019.6 using the Williams7B [1] forcefield with modified dihedrals for the NB backbone (details in Sec. 3.3.1). We used a cut-off of 1 nm with dispersion corrections for energy and pressure for van der Waals interactions and timestep of 1 fs and constrained the bonds with hydrogen atoms using the Lincs algorithm [109]. Production runs were performed in the canonical (NVT) ensemble using the velocity re-scaling thermostat [59]. Isothermal–isobaric (NPT) simulations with the Parrinello-Rahman barostat [110] were performed to calculate the density and Berendsen barostat [52] were used for annealing and equilibration runs.

Atomistic simulations were performed for 5-n-hexyl-2-NB (PNB-C6) and 5-n-nonyl-2-NB (PNB-C9) melts with different backbone activities: all-racemo, all-meso, random 50, and random 75. The random systems contain 50% and 75% of racemo dimers respectively, distributed randomly among meso dimers for each chain. The alkyl side chains were all bonded to the $5th$ carbon with a random 50:50 *exo-endo* isomerism in each chain.

4.3 Results

4.3.1 Thermodynamic properties and structure

Fig. 4.1 shows the specific volume of PNB-C6 and PNB-C9 at different tacticities. We see a similar trend of lower V_{sp} for systems with a higher ratio of racemo dimers regardless of side chain and higher V_{sp} for PNB-C9 at all tacticities. The change in specific volume while cooling the system at the rate of 10 K/ns was used to derive T_g. We observe a broad range of possible T_g values since the thermal expansion coefficient does not change dramatically between melt and glassy states. A similarly weak transition is observed in experimental ellipsometry measurements [75]. As reported in the literature using experimental methods, T_g decreases when we increase the side chain length. Since we are simulating short chains compared to the high molecular weights used in experiments, we expect our melts to have a lower T_g [121]. However, the high cooling rate used in simulations results in overestimation of T_g [122, 123, 124] compared to rates used in experiments. The T_g values we obtained are in the range of values reported in the literature using different methods and samples (for PNB-C6, 446 K using ellipsometry or 483 K using DMA [75] and 553 K using DMA [91]). Considering the uncertainty of the interception point used for driving T_g, we do not expect a significant difference between T_g of different tacticities for either PNB-C6 or PNB-C9.

Fig. 4.2 shows the calculated X-ray scattering patterns. Similar to un-substituted PNB [7], the experimental WAXS profile of alkyl-substituted PNB [96, 95, 10, 11] show an amorphous glass with two separate peaks which have been attributed to some intermediate ordering in the chain packing [96, 10]. Our model accurately predicts the position of PNB-C6 [11]. All PNB tacticities have similar peak positions, with high racemo content resulting in

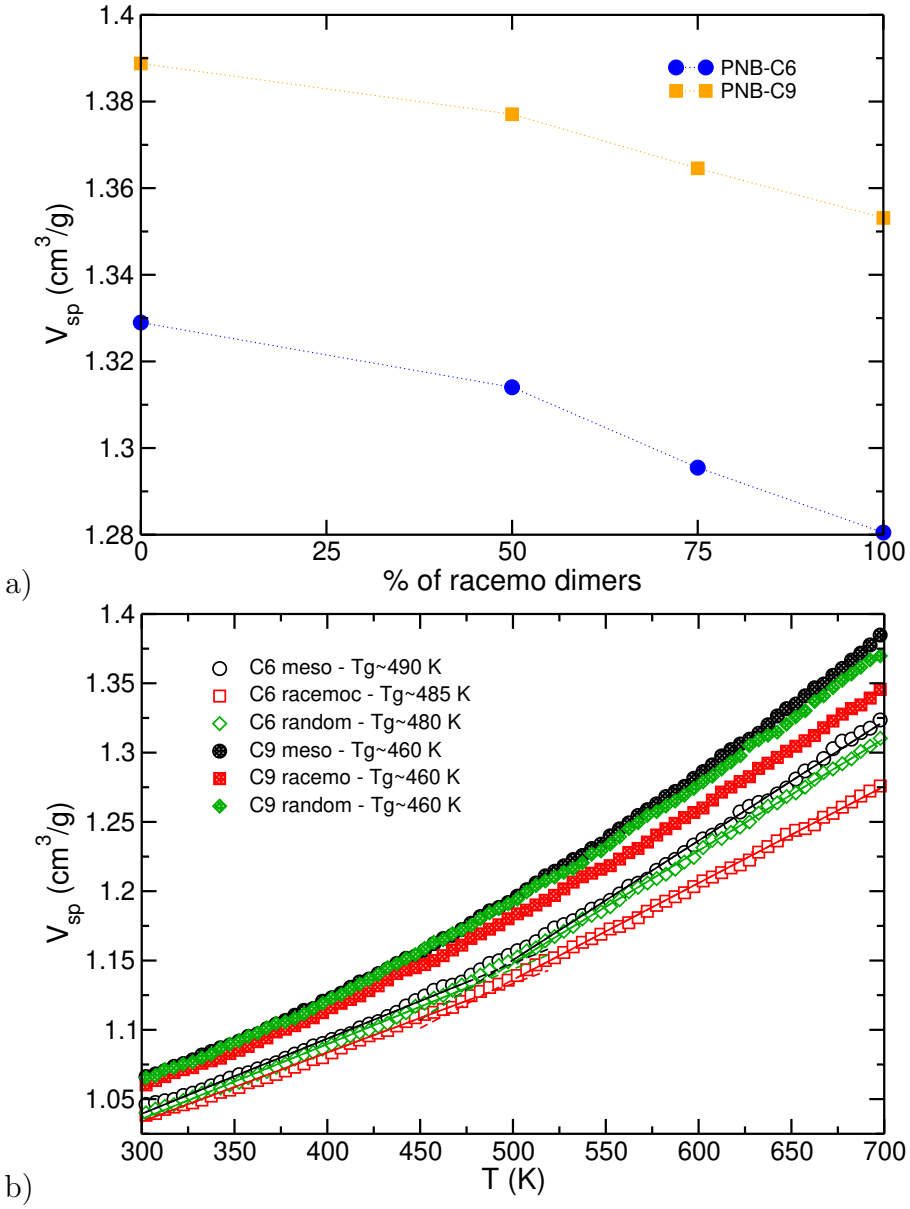


Figure 4.1: a) Specific volume (V_{sp}) with tacticity for PNB-C6 and PNB-C9 at 700 K. b) V_{sp} with temperature and T_g at the cooling rate of 10 K/ns for PNB-C6 and PNB-C9. Each point represents the average over a 5 K range (6000 points). Solid lines mark the range of linear fit. Dashed lines show the interception corresponding to Tg. Error smaller than symbol size.

broader signals and high meso content resulting in higher intensity in the first peak. For PNB-C6 and PNB-C9, the high q peak is similar across different tacticities while the first peak shifts to lower q by increasing the racemo ratio. Kai *et al.* [11] reported data for PNB-C6 samples from two different catalysts, Ni and Pd. Based on simulation results, the position of the first q peak from the Ni sample could be an indication of higher racemo content in the sample compared to the Pd sample. Based on the carbon-carbon radial distribution function (g_{CC}), in all systems, the position of the neighbor shells is similar across different tacticities. The number density of the bonded pairs at distances below the first intra-molecular neighbor shell is responsible for the position of the high q peak, and it is similar across different tacticities. Above the first inter-molecular neighbor shell, the racemo system has a higher density of intra-molecular neighbors and a longer distance to reach melt density which results in the shift of the first peak to lower q as the ratio of racemo dimers increases.

Experimental results show that increasing the length of the PNB-R side chain results in a decrease in relative intensity low to high q peaks, which has been attributed to a decrease in inter-molecular ordering [96]. However, the position of the high q peak which is attributed to intra-molecular interactions does not depend on the size of the alkyl side chain [96, 10, 95]. We found a similar trend for similar tacticities of PNB-C6 and PNB-C9. The position of the random PNB-C9 peaks in relation to experimental PNB-C8 and PNB-C10 match this trend, but tacticity has a large effect on the position and intensity of the first peak for the same side chain.

4.3.2 Conformational properties

Fig. 4.3 shows the characteristic ratio (C_n) of the chains as a function of intra-molecular monomer distance. As the length of the alkyl side chain increases, the chains become stiffer at all tacticities. Regardless of the side chain, chains with higher content of meso dimers are longer. Similar to unsubstituted PNB (Sec. 3 3.3.3), the purely racemo chains exhibit a degree of helicity which reduces the chain size as shown in Fig. 4.4. As the length of the side chain is increased, the racemo chains become less ordered with more kinks and imperfections

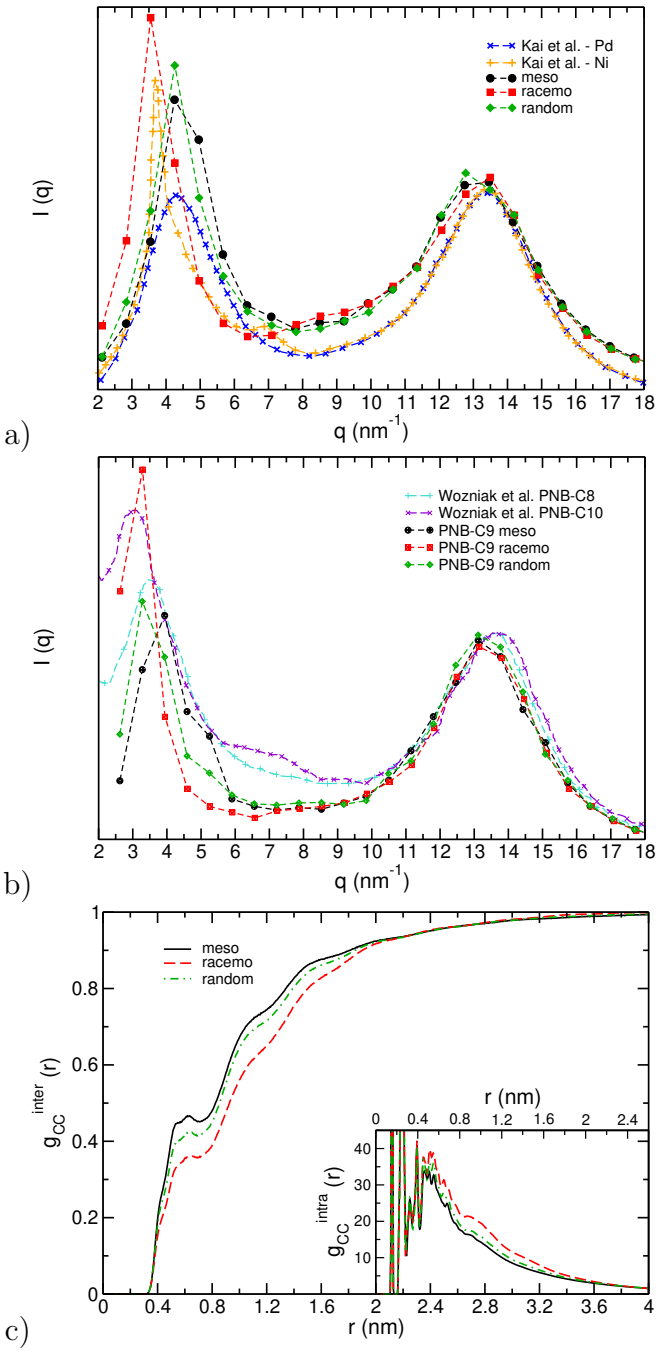


Figure 4.2: a) X-ray scattering patterns calculated for PNB-C6 compared with experimental data from two samples with unknown tacticities from Kai *et al.* [11] (λ = 0.1 nm). b) X-ray scattering for PNB-C9 compared with PNB-C8 and PNB-C10 from Wozniak *et al.* [10] (λ = 0.154 nm). c) Intra-molecular and inter-molecular radial distribution function (g_{CC}) of PNB-C6. All data at 300 K.

in the helical structure. Racemo PNB-C6 displays a similar conformational correlation at 700 K and 800 K.

4.3.3 Dynamics

Fig. 4.5 shows dynamics of PNB-C6 and PNB-C9. We calculated the autocorrelation function $\left(C(t) = \frac{\langle \vec{V}(t)\vec{V}(0)\rangle}{\langle \vec{V}^2(0)\rangle}\right)$ of the side chain vector and chain end-to-end vector to quantify the segmental and chain dynamics respectively. PNB-C6 and PNB-C9 display the same trend, with the racemo system displaying significantly slower segmental and chain dynamics. As expected, PNB-C9 chains are faster than PNB-C6 across all tacticities.

The Rouse mode [139] for a segment with N/p monomers is defined as:

$$\vec{X}_p(t) = \left(\frac{2}{N}\right)^{0.5} \sum_{i=1}^{N} \vec{r_i}.\cos\left(\frac{p\pi\,(i-0.5)}{N}\right) \tag{4.1}$$

Where $\vec{r_i}$ is the position of the ith monomer. We calculated the autocorrelation function of different modes and fitted them with a stretched exponential to calculate the average relaxation time ($\langle\tau_p\rangle$):

$$\frac{\langle \vec{X_p}(t).\vec{X_p}(0)\rangle}{\langle \vec{X_p}^2(0)\rangle} = \exp\left(-\left(\frac{t}{\tau_p}\right)^{\beta_p}\right) \tag{4.2}$$

$$\langle\tau_p\rangle = \left(\frac{\tau_p}{\beta_p}\right)\Gamma\left(\frac{1}{\beta_p}\right) \tag{4.3}$$

The meso systems are the closest to the Rouse prediction of relaxation modes, which assumes that the modes are independent. In contrast, in the racemo systems, the relaxation times do not change below $p = 4$ (≈ 9 monomers) which is in the scale of a helix turn. This trend remains for PNB-C6 even at the high temperature of 800 K. For smaller modes and possibly longer chain lengths, meso and random systems have similar rouse times, while for short segments all meso systems are faster.

The stress-stress autocorrelation displayed in Fig. 4.5 is defined as:

$$G(t) = \frac{V}{3k_BT}\langle\sum_{\alpha\beta}^{\alpha\neq\beta} P_{\alpha\beta}(t)P_{\alpha\beta}(0)\rangle \tag{4.4}$$

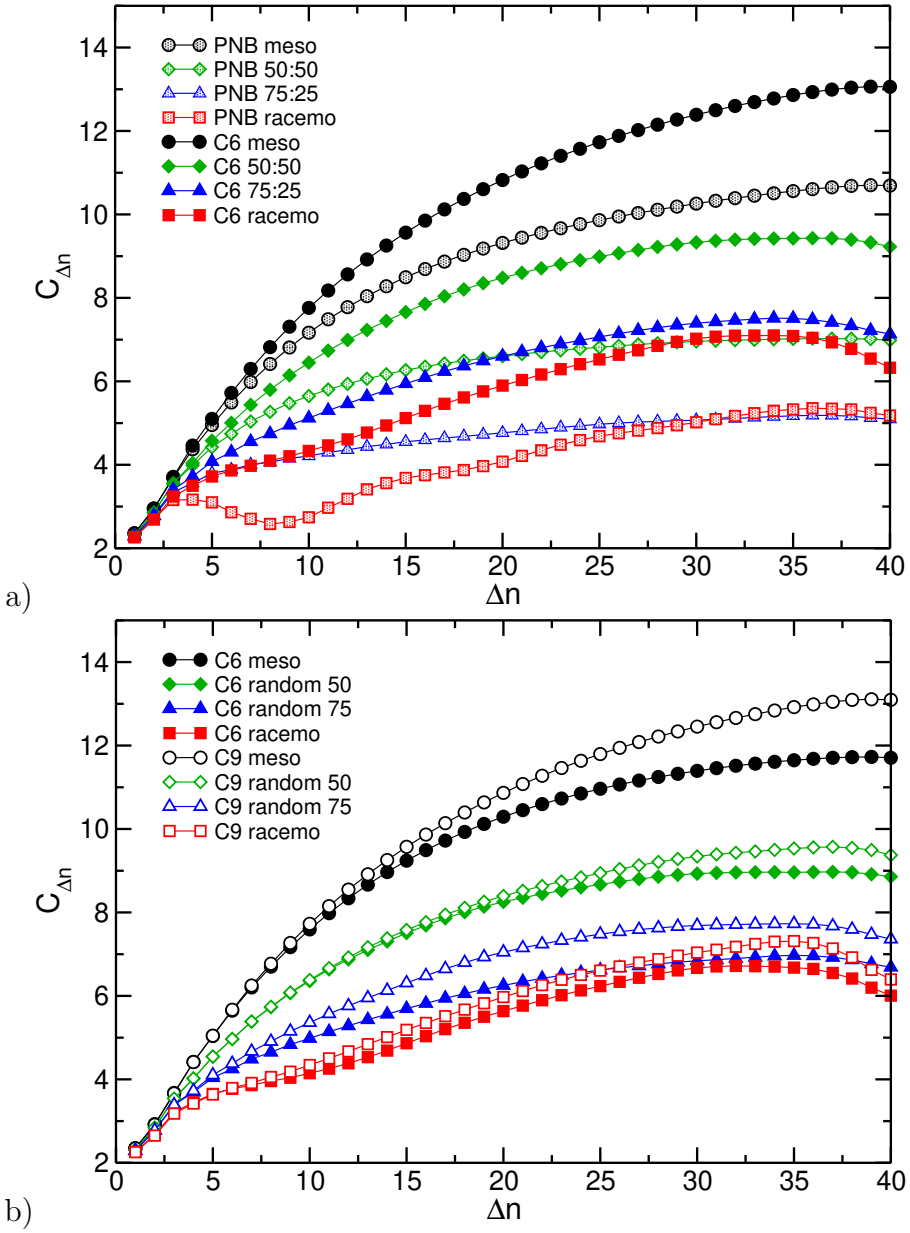


Figure 4.3: Characteristic ratio ($C_n = < R_e^2 > /2(n+1)l^2$ with $l = 1.53\,\text{Å}$) as a function of monomer distance (n) for a) PNB and PNB-C6 at 800 K and b) PNB-C6 and PNB-C9 with at 700 K.

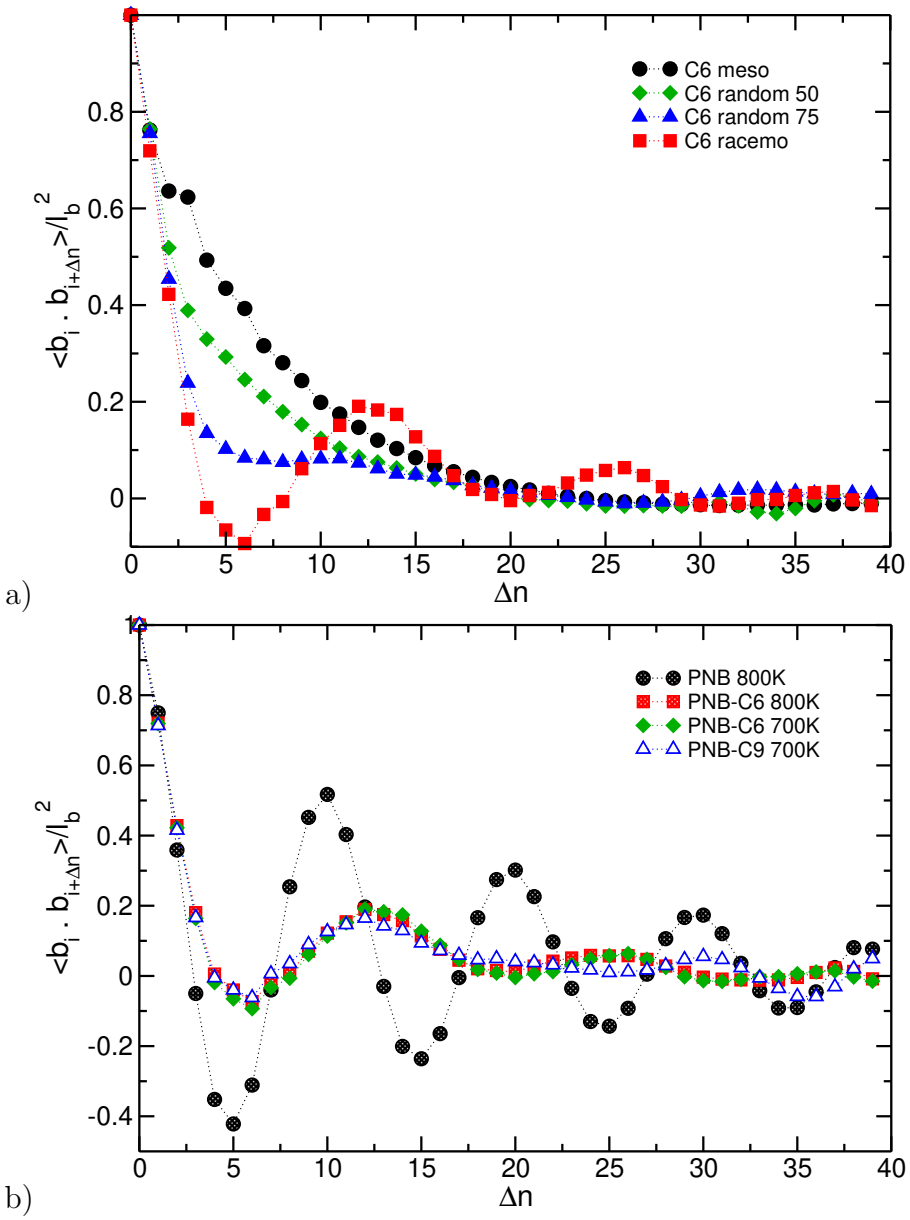


Figure 4.4: Normalized correlation of the C_2-C_3 bond vector (with length l_b) for a) PNB-C6 at 700 K. b) Effect of alkyl side chain on conformation and secondary-structure of racemo chains at 700 K and 800 K.

Three relaxation modes are observed in G(t). The fast (β) relaxation at short times, the segmental (α) relaxation, and the chain relaxation. Different tacticities show a similar β relaxation. As seen in $C(t)$ relaxations, the systems with a higher content of meso dimers have a faster α relaxation while the chain relaxation of meso and random systems is similar at longer times. Both PNB-C6 and PNB-C9 follow a similar trend in terms of tacticity, however, as the length of the side chain increases, the dependence of dynamics on tacticity becomes less significant.

4.4 Conclusions

The effect of tacticity on the thermodynamic, conformation, and dynamic properties of PNB-C6 and PNB-C9 follows a trend similar to PNB. Increasing the length of the side chain results in stiffer chains with faster dynamics regardless of tacticity. However, as the length of the alkyl side chain increases, the racemo chains become less helical and the difference between dynamic properties of meso, racemo, and random systems becomes smaller.

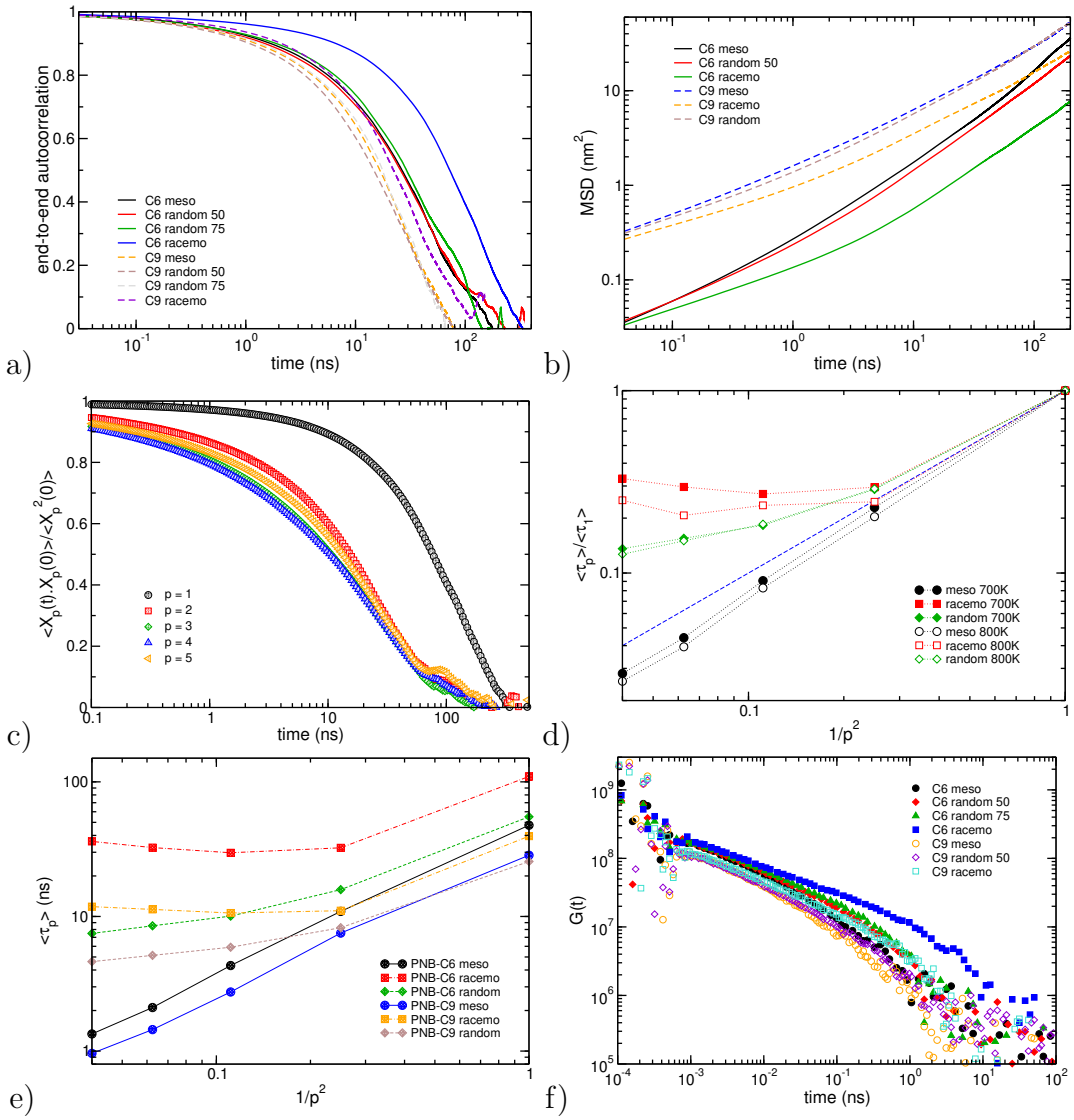


Figure 4.5: a) Autocorrelation of chain end-to-end vector, b) MSD, c) autocorrelation of Rouse modes for PNB-C6 with racemo tacticity, d) average Rouse times normalized by first mode for PNB-C6 (dashed line represents the Rouse prediction of $1/p^2$) at 700 K and 800 K, e) average Rouse times, and $G(t)$ of g) PNB-C6 and h) PNB-C9. All simulations are at 700 K unless otherwise specified.

Chapter 5

Coarse-graining of polyisoprene melts using inverse Monte Carlo and local density potentials

This chapter is based on the following publication:

Shahidi, N., Chazirakis, A., Harmandaris, V., & Doxastakis, M. (2020). Coarse-graining of polyisoprene melts using inverse Monte Carlo and local density potentials. The Journal of Chemical Physics, 152(12) [140].

5.1 Introduction

Molecular modeling of polymers relies on efficient lattice or continuum representations to capture material properties over the large length-scale and long time scales of interest [141]. Methods to build coarse-grained (CG) models representative of chemically-specific systems (including polymer melts) have improved over the last two decades [112, 142, 143, 144, 145, 146, 147]. Bottom-up CG polymer models are often assembled by utilizing detailed atomistic trajectories of oligomer chains that exhibit short relaxation times in contrast to commercial-grade macromolecules. Structure-based coarse-graining methods, such as iterative Boltzmann inversion (IBI) and inverse Monte Carlo (IMC) construction of the pair-wise model, aim for matching the structure proposed by a higher resolution model (often

atomistic) by tuning the interaction potential [111, 148, 23]. Forcefield development proceeds by iterative refinement of the CG interaction terms guided by deviations from the target pair distribution function, sampled bond lengths, bending, and dihedral angles. Due to the coupling of separate potential terms, several optimization cycles are commonly performed in sequence [23] with the assumption that a pair-wise tabulated CG forcefield that lacks cross terms, e.g. bond-angle, will adequately describe chemically-specific polymeric systems. Polyisoprene (PI) is just one of many examples where such CG models have been successfully employed to study the melt or hybrid systems with solid surfaces [23, 149, 150, 151, 142, 152]. Note that coarse-grain modeling that focuses on capturing structural details of the atomistic systems can serve as an intermediate step towards the creation of well-equilibrated initial structures of macromolecular systems by re-introducing atomistic details. Studying local dynamics or structure in atomistic detail is limited by the long chain relaxation times of polymers and back-mapping procedures can address these challenges by transitioning between models at different resolutions [37, 152, 153, 154].

Apart from structure, it is highly desirable that the CG model captures thermodynamic properties, enabling studies under constant pressure. Deviations in the pressure of the CG models developed with IBI are often addressed by the addition of a linear attractive tail to the pair nonbonded interactions [23, 112]. Pressure matching via this process requires a readjustment of the remaining potential terms because of their coupled contribution in matching the desired structure as proposed by the atomistic model [23, 149, 150, 151, 36, 142, 152]. Thermodynamic consistency is not a challenge exclusive to IBI; [155, 147, 156] IMC or force-matching procedures often require the addition of constraints to match the thermodynamic state of the input model [157, 158, 159]. Matching volume (V) fluctuations as expressed by the isothermal compressibility $\kappa_T = (\langle V^2 \rangle - \langle V \rangle^2)/(k_B T \langle V \rangle)$ is even more demanding. This has been shown in several studies, i.e. on water [36], polybutadiene [38] and polystyrene, [37] where a choice between matching either pressure or compressibility is presented [36]. It is important to emphasize that thermodynamic consistency improves with higher resolution CG models [160, 161] where fewer degrees of freedom are eliminated. This was recently shown for PI with a 2-bead per monomer CG model [162] that is closer to the soft degrees of freedom represented by dihedral angles along the PI chain (3 per monomer)

[163, 164]. However, such models offer moderate computational benefit relative to united atom models (5 interaction sites per monomer) and require the development of more complex forcefields given the increased number of particle types (and consequently distinct interaction terms) in the chosen CG representation.

Beyond modifying pair-potentials or increasing resolution, a different proposition is to supplement the forcefield with a volume-dependent term determined by the pressure profile of the mapped atomistic trajectory [160]. The posterior addition of extra potential terms to a CG forcefield requires further refinement due to the expected coupling between each term [165, 145, 166]. A different approach based on the integral equation coarse-graining (IECG) method, treats the density as an intrinsic property and active variable of the CG model [147]. In IECG the effective CG interactions are developed analytically using the Ornstein-Zernike equation of the liquid state theory.

A distinct path that motivated this study concerns the development of local density potentials to supplement pair interactions with terms that are multi-body by design. While the application of multi-body potentials has been common practice for many decades (for example in simulations with the embedded atom method [167, 168] or in simulations using dissipative particle dynamics [169, 170]), the introduction of such interactions has found renewed interest in terms of constructing bottom-up chemically-specific CG models [171, 172, 173, 174, 175, 176, 177, 178, 179, 180, 181]. In the field of molecular liquids, multi-body potentials can serve to improve predictions on structure and thermodynamics. CG models are often described by a single bead and the potentials include a term that depends on the local density. Techniques developed for the optimization of solely pair potentials can be extended with the incorporation of multi-body terms to improve target properties. In one such recent study, Moore *et al.* optimized multi-body interactions by matching the pressure in simulations of hexahydro-1,3,5-trinitro-s-triazine with pair interactions developed by the force-matching method [176]. In another study, Rosenberg used the relative-entropy optimization supplemented with local density potentials [181]; in this scheme the pair and density potentials were simultaneously optimized by calculating the relative entropy at each iteration using short trial simulations in the NVT ensemble. Results were compared to CG models with solely pair interactions developed with the Inverse Monte Carlo method. In the

field of polymers, Sanyal and Shell used the relative entropy framework to parametrize local density potentials for a bead-spring model in an implicit solvent [175]. The optimization performed in the NVT ensemble targeted the development of the nonbonded interactions while the bond and angle potentials were retained from the explicit water model. A different study by Agrawal *et al.* introduced a density-dependent potential term using the embedded-atom method to model semi-crystalline polyethylene [182]. CG bond and bending angle potentials were developed with the IBI method while the parameters of the embedding energy function were calibrated using least squares minimization to match the macroscopic pressure of the system at different state points.

Finally, we should also briefly mention that many-body CG potentials have also been developed in a more rigorous concept based on cluster expansion techniques [183]. It was found that the cluster expansion formalism can provide accurate effective pair and three-body CG potentials, mainly at high temperature and low-density regimes. In addition, such a methodology is computationally efficient since the hierarchy of the effective nonbonded CG potentials terms is developed by the conditional sampling of a few CG particles, and no information from long n-body (bulk) simulations is required. However, for dense liquid systems, as the bulk polymer studied here, this method is not directly applicable since the numerical estimation of higher than three-body order terms is required. This remains a major computational challenge.

In this study we develop a methodology to introduce details of the (many-body) local environment in a bottom-up coarse-graining approach applied to an atomistic model of *cis*-1,4 PI. As described previously, PI has been studied extensively with IBI and a recent report highlighted the challenges in capturing structure, density, and compressibility [162]. We implement the Inverse Monte Carlo method, which to the best of our knowledge has not been applied previously on polyisoprene melts and we supplement the forcefields with a local density term. In our study, all potential terms are developed simultaneously while targeting specific order parameters, and their covariance is accounted for in the optimization process. Section 5.2 presents the methodology together with a systematic evaluation of the first "solvation" shell and the validity of an isotropic approximation of the arrangement of nearest neighbors. Given the limited applications of IMC in polymer systems, we also provide

a short description of the method in Section 5.2.3. Section 5.3 presents our findings on the optimization process with three different forcefields (one solely with pair interactions and two that include local density terms). We examine the ability of different approaches to capture the local and global structure. We evaluate the performance of the CG forcefields with regard to the dynamics of PI oligomers by using results from molecular dynamics (MD) simulations provided by our collaborators, Dr. Antonis Chazirakis and Dr. Vagelis Harmandaris [140]. We finish with a brief discussion of our findings and the opportunities that our study reveals.

5.2 Method

5.2.1 Atomistic simulations

We performed atomistic simulations with a united atom (UA) model for *cis*-1,4 PI that captures the polymer properties quantitatively as shown in past studies [164, 184, 185, 186, 187, 162]. MD simulations were executed for a system of 100 chains with N=30 repeat units (M_w=2043 g/mol) using the GROMACS 2018.3 software [53]. We employed a leap-frog algorithm with a 2 fs time-step and a cutoff of 1.2 nm for van der Waals interactions. The model does not include any partial charges so electrostatic interactions were not considered. Simulations were conducted in the *NPT* ensemble with the Parrinello-Rahman pressure coupling [110, 188] and Nosé-Hoover thermostat [189, 190] with a 0.5 and 2 fs time-step respectively. Properties were calculated over 100 ns, 250 ns and 400 ns at 413 K, 353 K and 298 K and 1 bar following an equilibration period of 120 ns, 200 ns and 1.3 μs respectively. While the average chain relaxation time (slowest mode) at 298 K is estimated as 5.6 μs, the calculated properties show small fluctuations after the 1.3 μs equilibration period. The model predicts a density of $\rho \approx 0.894$ g/cm^3 and an isothermal compressibility of $\kappa_T \approx 8.7\times10^{-5}$ bar^{-1} at 298 K. Experimental data values for high molecular weight PI at room temperature are 0.9 g/cm^3 [191] and $\kappa_T \approx$5-5.3$\times10^{-5}$ bar^{-1} [192, 193], which are in good agreement with our data given the lower molecular weight of our model [185] and the presence of isomers in experimental samples.

5.2.2 Coarse-grain models

A critical parameter in CG modeling is the choice of CG mapping. Different schemes have been employed for CG models of PI with the most common placing a single bead per repeat unit at the center of the bond between two consecutive monomers [23, 151, 152]. We found that this mapping leaves chain ends with a very anisotropic environment and introduces additional challenges to the coarse-graining procedure adopted in this work. To simplify the application of the multi-body terms that depend on local densities, we represent each repeat unit with a single CG bead centered on the monomer center of mass [194].

There are three CG models developed in this study, CG-pair, CG-CN, and CG-NN. A summary of these models together with a brief description of their differences is provided in Table 5.1.

The CG-pair model contains bonded interactions and only pair-wise nonbonded interactions. The effective interactions are optimized to match specific distributions. We calculated the distributions of bond lengths ($\mathbf{S}_{\mathrm{b}}$), bending angles ($\mathbf{S}_{\mathrm{a}}$), dihedral angles ($\mathbf{S}_{\mathrm{d}}$) and distances between nonbonded pairs ($\mathbf{S}_{\mathrm{nb}}$, calculated for intra- and inter-molecular neighbors that are separated by more than three CG bonds) as described further in Section 5.2.3. At each temperature, the discretized distributions were extracted from the mapped trajectory and concatenated to the vector $\mathbf{S}_{\mathrm{target}}$ used as the target for coarse-graining. Furthermore, to account for the many-body interactions beyond the pair-wise assumption, we derived two forcefields (CG-NN and CG-CN) by employing an additional multi-body potential (U_{NN}), where n is the number of nearest-neighbors (NN). The optimization of these forcefields with IMC required the introduction of the distribution of n ($\mathbf{S}_{\mathrm{NN}}$) to the set of target distributions. It has been reported that pair potentials often fail to quantitatively capture the short-range effective interactions from neighbors in the first coordination shell (first minimum of radial distribution function $g(r)$) and corrections via multi-body contributions are necessary to capture the local density as well as density fluctuations [159, 173]. A computationally inexpensive way to calculate the number of nearest-neighbors (n) of a bead on the fly is through a continuous isotropic indicator function (Θ) that reduces to zero at a fixed cut-off. A common choice for $\Theta(r)$ is the Lucy function [195, 196, 176, 197]. Sanyal

et al. [175, 180, 181] optimized the cut-off radius as a system parameter using the relative entropy coarse-graining framework. Faure *et al.* derived the local density using Voronoi tessellation [174, 198, 199, 200]. Here, we explore the use of the solid-angle nearest-neighbor (SANN) algorithm developed by Meel *et al.* [12] to extract n. The SANN algorithm defines n neighbors on a particle i based on the separation between i and all remaining particles as well as their individual contributions towards a total solid angle 4π which leads to the following condition for the maximum neighbor radius R_i^n:

$$R_i^n = \frac{\sum_{j=1}^{n} r_{i,j}}{n-2} < r_{i,n+1} \tag{5.1}$$

The resulting distributions of n at three different temperatures are shown in Fig. 5.1a. Note that the distribution of nearest-neighbors defined by SANN presents minimal changes over a broad range of temperatures. The increase of the density at lower temperatures translates to a lower volume occupied by the first neighbors (defined by R_i^n). An illustration of nearest neighbors is shown in Figure 5.1b. We observed that chain ends exhibit a slightly increased n (positioned at longer distances) due to their increased free volume [185]. While in principle this could translate to a need for a separate density potential this effect is minimized when introducing a uniform indicator function (described below) since for a fixed range similar distributions were observed irrespective of the position of the CG bead along the chain.

The SANN analysis provides a systematic method to define the indicator function from the contribution of nearest-neighbors to the local density surrounding the CG bead and allowed us to quantitatively assess the accuracy of the isotropic approximation of local density. The indicator function $\Theta(r)$ is defined as the fraction of the total pair distribution function from the nearest-neighbors $\Theta(r) = g_{\mathrm{NN}}(r)/g_{\mathrm{tot}}(r)$ and extrapolated to 1 for short separations before the first peak (Fig. 5.1c, ≈ 0.27 nm). The resulting indicator functions calculated at three temperatures are depicted in Fig. 5.1d. It is evident that the aforementioned definition of a "local volume" decreases with temperature as the size of the first coordination shell becomes progressively smaller. The number of nearest-neighbors (n) around a particle i can be calculated using $\Theta(r)$ as:

Table 5.1: Nomenclature for the developed CG models based on their nearest-neighbor (NN) potentials.

Model	NN potential	Ensemble
CG-pair	None	NVT
CG-CN	Attractive	NPT
CG-NN	Full	NPT

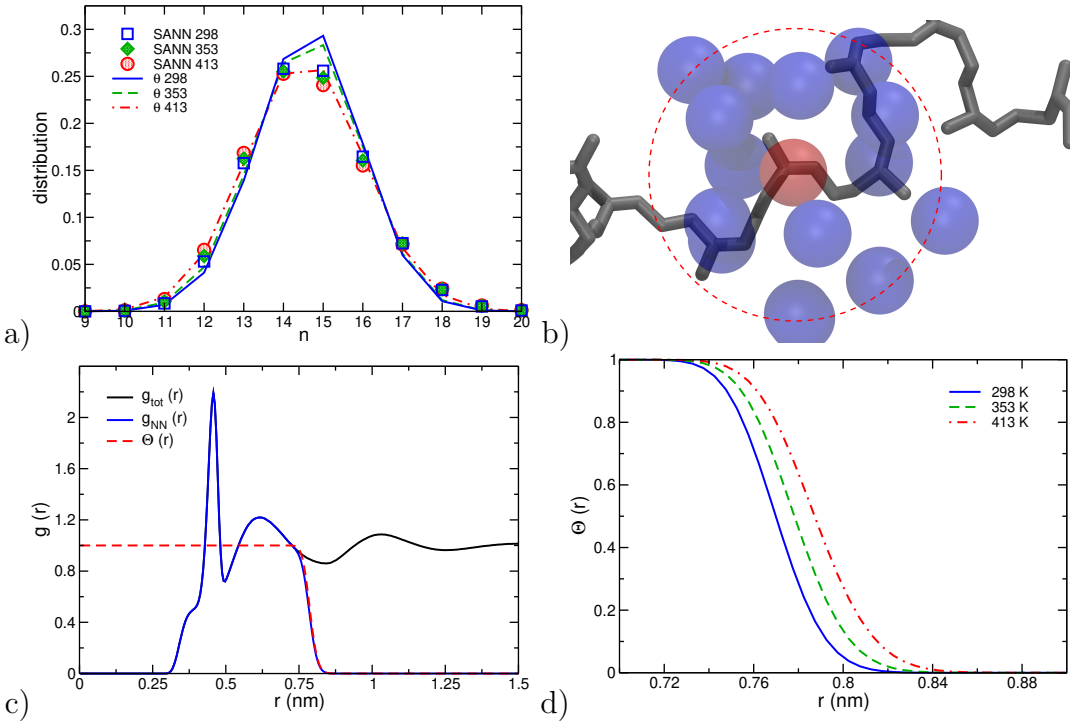


Figure 5.1: a) Distribution of the number of nearest-neighbors (n) extracted with SANN [12] (symbols) and by the use of indicator functions (lines) at 298 K (blue), 353 K (green) and 413 K (red). b) Nearest neighbors (blue) of a CG bead (red) as extracted from SANN analysis on a mapped atomistic configuration. The dashed red lines represent a circle centered on the examined bead. c) Total pair-distribution function (g) and contribution from nearest-neighbors (g_{NN}) as determined by SANN at 413 K. The dashed line depicts the extracted indicator function Θ. d) $\Theta(r)$ extracted at different temperatures.

$$n_i = \sum_{j \neq i}^{N} \Theta(r_{ij}) \tag{5.2}$$

Note that for consistency with pair-distribution functions in defining local density, the center atom does not contribute to the calculation of n [201]. Intra-molecular neighbors that participate in bond stretching, angle bending, and torsional potentials were included in the list of potential neighbors which underlines a complexity present when working with polymers, i.e. the unavoidable direct or indirect correlation between the calculated distributions of the corresponding order parameters. Comparing the direct results of SANN and the analysis performed using an isotropic $\Theta(r)$, we observe that deviations between the two calculations increase as temperature decreases. The isotropic assumption depends on the mapping scheme employed as well as the specific system and conditions studied. SANN was introduced originally as a rapid algorithm to perform NN calculations on-the-fly as an alternative to simulations with Voronoi tessellation of space which is computationally demanding. Although we opted for the simpler $\Theta(r)$ route for calculating n in this study, we note that SANN could be explored for on-the-fly calculations in Monte Carlo simulations, particularly at lower temperatures where the application of the spherical approximation presents significant deviations. Using n calculated from Eq. 5.2, forcefields for the CG model were assembled in tabulated forms and the potential of the CG-CN and CG-NN models assumed the general form of

$$U_{\text{total}} = U_{\text{bond}}(l) + U_{\text{angle}}(\theta) + U_{\text{dihedral}}(\phi) + U_{\text{nonbond}}(r) + U_{\text{NN}}(n) \tag{5.3}$$

where U_{bond}, U_{angle} and U_{dihedral} are the bonded potentials that depend on bond length (l), angle (θ) and dihedral (ϕ) of consecutive beads along the chain. U_{nonbond} is the pair interaction between nonbonded beads and is a function of their separation (r). U_{NN} depends on the number of nearest-neighbors surrounding the bead (n) which includes both bonded and nonbonded neighbors. The force on a particle i from a surrounding neighbor j can be calculated as [202, 176, 203]:

$$f_{i,j} = -\left[\frac{dU_{NN}}{dn}(n_i) + \frac{dU_{NN}}{dn}(n_j)\right]\frac{d\Theta(r_{ij})}{dr}\frac{r_i - r_j}{r_{ij}} \tag{5.4}$$

The above equation underlines the advantage of choosing an indicator function that varies continuously with r. As described in the next section, we derived three different forcefields in this study, one with only pair interactions and two with local density potentials.

5.2.3 Inverse Monte Carlo

We constructed the CG force fields using the inverse Monte Carlo (IMC) method (also known as the inverse Newton method) [24, 204]. IMC provides a numerical framework to derive a set of potentials that reproduce the target distribution vector ($\mathbf{S}_{\text{target}}$) derived from the atomistic model. The tabulated potentials (as constant grids) are updated at each iteration of the IMC procedure. The potential at each bin, E_α, contributes to the bonded, nonbonded, or NN energy with the corresponding occurrence S_α. The total potential energy of the system is calculated by:

$$U_{\text{total}} = \sum_{\alpha} S_\alpha E_\alpha \tag{5.5}$$

The initial estimate for potentials at 413 K was derived from the Boltzmann inversion of target distributions, [23] e.g, $E^0_{\text{nb}}(r) = -\text{k}_\text{B}T \ln g_{\text{nb}}(r)$ where $g_{\text{nb}}(r) = S_{\text{nb}}(r)/(4\pi r^2 N)$. Likewise, we estimated the nearest-neighbor potential from the distribution $S_{\text{NN}}(n)$ as $E^0_{\text{NN}}(n) = -\text{k}_\text{B}T \ln S_{\text{NN}}(n)$ (see Figure 5.1a). We initiated the optimization at lower temperatures using potentials from the immediate higher temperature as the initial guess. The deviation of the distribution vector from the target $\Delta\langle\mathbf{S}\rangle = \langle\mathbf{S}_{\text{obs}}\rangle - \langle\mathbf{S}_{\text{target}}\rangle$ was sampled at each iteration and the potential was updated by $\mathbf{\Delta E}$ after solving the inverse problem:

$$\Delta\langle S_\alpha\rangle = \sum_{\beta} \frac{\partial\langle S_\alpha\rangle}{\partial E_\beta}\Delta E_\beta + \mathcal{O}(\Delta\mathbf{E}^2) \tag{5.6}$$

Note again that the vector $\mathbf{S}$ is a concatenated vector with populations sampled for each bin of the tabular potentials (including bonded, angular, dihedral, pair, and NN terms),

and the vector $\mathbf{\Delta E}$ consists of an update to all tabulated terms. The Jacobian matrix ($\mathbf{A}$) employed in the equation above is calculated using the relationship [24, 204]:

$$A_{\alpha\beta} = \frac{\partial \langle S_\alpha \rangle}{\partial E_\beta} = -\frac{\langle S_\alpha S_\beta \rangle - \langle S_\alpha \rangle \langle S_\beta \rangle}{k_B T} \tag{5.7}$$

The linear problem in Eq. 5.6 is ill-defined as can be further shown by singular value decomposition [158, 205], e.g., the distribution of sampled bond lengths depend on differences in the bonded potential and not the value at the minimum. Therefore we minimized the following objective function instead [158]

$$\text{objective function} = ||\mathbf{A}\Delta\mathbf{E} - \Delta\mathbf{S}||_2 + \gamma||\Delta\mathbf{E}||_2 \tag{5.8}$$

that includes a regularization term to penalize large changes in potentials (expressed as the Euclidean norm of the vector $\mathbf{\Delta E}$) and reduce the impact of statistical noise. We employed the Sequential Quadratic Programming algorithm as implemented in standard Python distributions. The regularization parameter γ controls the stability of the scheme at the expense of sensitivity; we decreased γ as $\mathbf{S}$ approaches the target up to the point where the method becomes unstable given the presence of statistical noise in our data; for our particular system and target vector we employed λ values in the range of 20 to 0.3. At each iteration, the minimum of the bonded potentials was shifted to zero while for the nonbonded potentials, the value at $R_{\text{cut}} = 1.5$ nm was constrained to zero. The bonded and nonbonded tables consisted of $100 - 150$ bins each and the NN potential had about 15; we found that the choice of grid affects the sensitivity of the optimization scheme as well as the strength of the relative contribution of each distribution to $\Delta\mathbf{S}$.

Several past studies restricted multi-body nonbonded potentials to solely providing cohesive energy to the system [206, 175]. Within the scheme proposed herein, we introduced an additional constraint in the minimization that ΔE should result to a monotonic NN potential decreasing as n increases. Effectively all repulsion in this new set of interactions (termed CG-CN model) will be provided by pair interactions testing directly whether such a simpler model provides an equally satisfactory description of the system under study.

The IMC procedure was performed employing our in-house Monte Carlo algorithms [57, 152] and included the execution of single particle displacements (89.95%) and reptate moves performed in a configurational-bias scheme [207]. Simulations for the model without NN interactions (CG-pair) were performed in the NVT ensemble to match the density of the UA model. The local density models were simulated in the NPT ensemble at 1 bar by including 0.05% attempts for volume changes. As documented in the literature, IMC requires exhaustive sampling of both distributions and correlations for the scheme to converge to a satisfactory solution [208, 158, 209]. The distributions herein were calculated over at least 400 million MC iterations (after an equilibration period of 20,000 iterations) to reduce the statistical noise with more iterations performed at lower values of λ. A technical but important detail of the scheme is that the sampling for the Jacobian matrix (Eq. 5.7) was performed on-the-fly every 2000 steps.

5.2.4 Coarse-grained simulations

MD simulations of CG models were performed to study dynamics. MD CG Results were provided by our collaborators, Dr. Antonis Chazirakis and Dr. Vagelis Harmandaris, who performed the simulations using their custom in-house parallel MD code and our CG potentials. The (additional) computational cost of including many-body terms, based on the distribution of nearest-neighbors, is about 2-3 times that of a typical simulation with a pair potential. This is mainly due to the extra neighbor lists which were separately constructed for the calculation of local density for each atom.

Simulations of the CG-NN and CG-CN models were performed in the NPT ensemble at 1 bar and different temperatures. The Parrinello-Rahman barostat [110, 188] and the Nosé-Hoover thermostat [189, 190] were used to maintain constant pressure and temperature. Simulations of the CG-pair model were performed in the NVT ensemble to maintain the density obtained from the corresponding UA simulations. The NVT runs were 10 ns long and the NPT runs were 4 ns long with the time-step of 1 fs.

5.3 Results

In the following sections, we present our findings on the structure, conformational properties, thermodynamic properties, and dynamics of the CG models compared to the underlying UA model as well as the performance of the method employed. We derived three models: (a) The first, "CG-pair", assumes solely pair-wise interactions between particles that do not interact via bond, angle, or dihedral potentials. The other two CG potentials include the multi-body potential acting on particles due to the number of NN in their local environment; (b) the "CG-NN" includes both attractive and repulsive multi-body terms, whereas (c) the "CG-CN" includes only attractive terms due to the constraint implemented during the forcefield development process.

5.3.1 Optimization

A clear advantage of the IMC procedure is the simultaneous refinement of separate interaction potentials based on distributions accounting to an extent for their coupled effect on the sampled distributions. It is therefore instructive to consider the performance of our scheme. Fig. 5.2a presents the norm of the deviation vector from the target distribution for the CG-CN forcefield at 413 K as a function of IMC iterations. Within 5 iterations, the initial $||\Delta\mathbf{S}||_2$ decreases by an order of magnitude while subsequent optimization is slower as the distribution vector approaches the target. The convergence route of individual terms depends on the choice of distribution grid (which determines the weight in $\mathbf{S}$) and the choice of the initial estimate. The initial potential results in high deviations in the nonbonded pair distribution which is the main contributor to the objective function. The inversion of the pair distribution function results in a repulsive potential (Fig. 5.2b, iteration 0) with little cohesion. Such an estimate could jeopardize the stability of CG NPT simulations during forcefield development. In our scheme, the inverted nearest-neighbor potential (Fig. 5.2c for the CG-CN model) provides the necessary attraction preventing the sampling of configurations with reduced local density. As the optimization progresses, the pair potential develops a first minimum to match the distribution of pairs (Iteration 10). The density of the

CG-CN model is rapidly converging to the targeted value at a faster pace than the matching of intra-molecular distributions.

The initial intra-molecular potentials provide a better estimate with smaller deviations, therefore the bonded terms undergo significant improvement only at later stages of the algorithm when sensitivity is increased by lowering the γ parameter. We reduced γ every 5 iterations to increase the allowed size of the update $\mathbf{\Delta E}$ in the forcefield at each step. After 10 iterations the nonbonded distribution resembles the target and the algorithm switches focus towards capturing intra-molecular distributions; remarkably this coincides with the algorithm attempting to match the tails of the nearest-neighbor distribution (see Iteration 10 and Iteration 22 in Fig. 5.2c) with a parallel rendering of the pair-potential at short distances positive and a second clear minimum over the second "solvation shell". Such observations highlight that if the fidelity in matching distributions is overlooked very different forcefields could be derived. We also emphasize (and will demonstrate further) that intramolecular neighbors and their placement is coupled to capture the local density accurately.

The iterative minimization is limited by a system-dependent minimum value of γ as further reduction results in instability. We found that this limit is coupled to the quality of distributions and cross-correlation terms; noise in the Jacobian is detrimental to the method therefore we opted to sample the distributions on the fly circumventing challenges and limitations imposed by storage of large trajectories. All three approaches (CG-pair in NVT, CG-NN, and CG-CN) converged to forcefields that were capable to capture the target distributions satisfactorily with small deviations from the target distributions. The potentials at 413 K provided a good initial estimate for rapid convergence at 353 K however at 298 K the slow structural evolution made the optimization process challenging even while the needed changes from the potentials refined at 353 K were minimal.

5.3.2 Forcefields

The forcefields of the three CG models optimized at 353 K are presented in Fig. 5.3 to demonstrate their significant differences. The CG-pair model is able to capture the target distributions quantitatively. However, it lacks necessary cohesion and is incapable of capturing the correct pressure in the NVT ensemble (and accordingly the correct

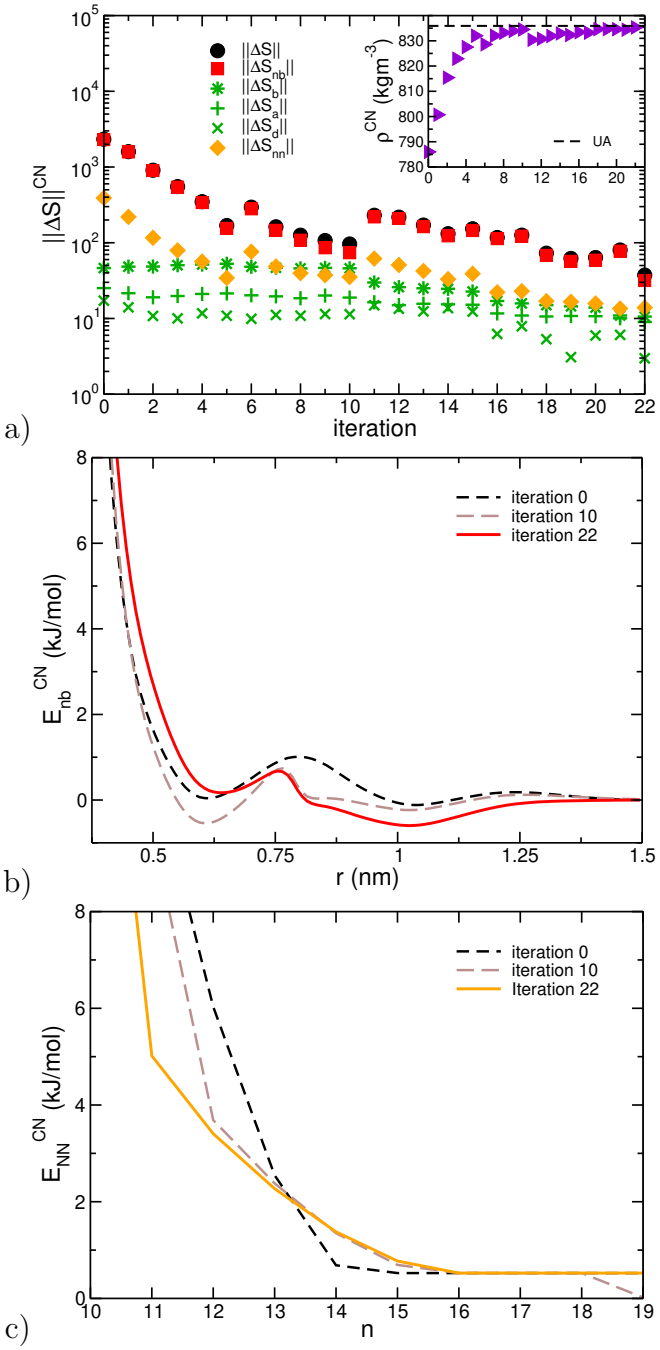


Figure 5.2: a) Convergence of distributions to target values during the IMC process (inset shows the convergence of density to the UA value at 1 bar) and optimization of the b) pair nonbonded potentials and c) nearest-neighbor potentials at 413 K for the CG-CN in the *NPT* ensemble.

density of the melt in an *NPT* simulation). In contrast, both CG-NN and CG-CN PI models include attractive nonbonded interactions with the latter limited to solely monotonic local density potentials as often considered in coarse-grain models with multi-body terms [165, 175, 210, 180]. Note that constraining the local density potentials to cohesive forces results in an increased pair-potential within the range of the chosen indicator function (Fig. 5.3e, 5.1d). Similarly, the repulsion provided by the local density potential in CG-NN at higher values of n (Fig. 5.3e) is counteracted by a more attractive pair potential in the range of the chosen indicator function (Figs 5.3e, 5.1d) to match $\mathbf{S}_{\text{nb}}$ in the first coordination shell. The above findings further underline: a) the strong coupling between pair nonbonded potential and local density potentials and b) the significance of the choice of "local volume" (or range of the multi-body term) in such forcefields. Clearly, the shape of the indicator function holds also a prominent role in guiding the potentials extracted; herein we followed a systematic approach based on the contribution of the first-neighbor shell to the total density profile. It is important to emphasize the unique challenges present in the bottom-up coarse-graining of polymers by direct contributions from proximal intra-molecular neighbors along the chain to the local density profile of a segment. This is evident by differences in the bond, angle, and dihedral potentials extracted as shown in Fig. 5.3 at 353 K with similar results at all temperatures studied. While all-three models are capable of capturing quantitatively the corresponding distributions significant variations can be observed by examining individual terms between the forcefields.

All CG forcefields (CG pair, CG-NN, and CG-CN) were able to reproduce the respective target distributions at different temperatures with minimal deviations; however, none was found to be temperature transferable. A refinement was introduced as described previously with additional optimizations performed to quantitatively capture the distributions at a different state point. Several strategies could be explored to optimize the potentials on multiple state points and improve transferability [177, 211, 212]. However, in our method, two additional features need to be considered: a) the definition of "local volume" changes across temperatures and correspondingly the employed indicator function, and b) the assumption of a spherical local volume at low temperatures needs to be examined. Fig. 5.1c presents a systematic approach to extract the temperature dependence of the

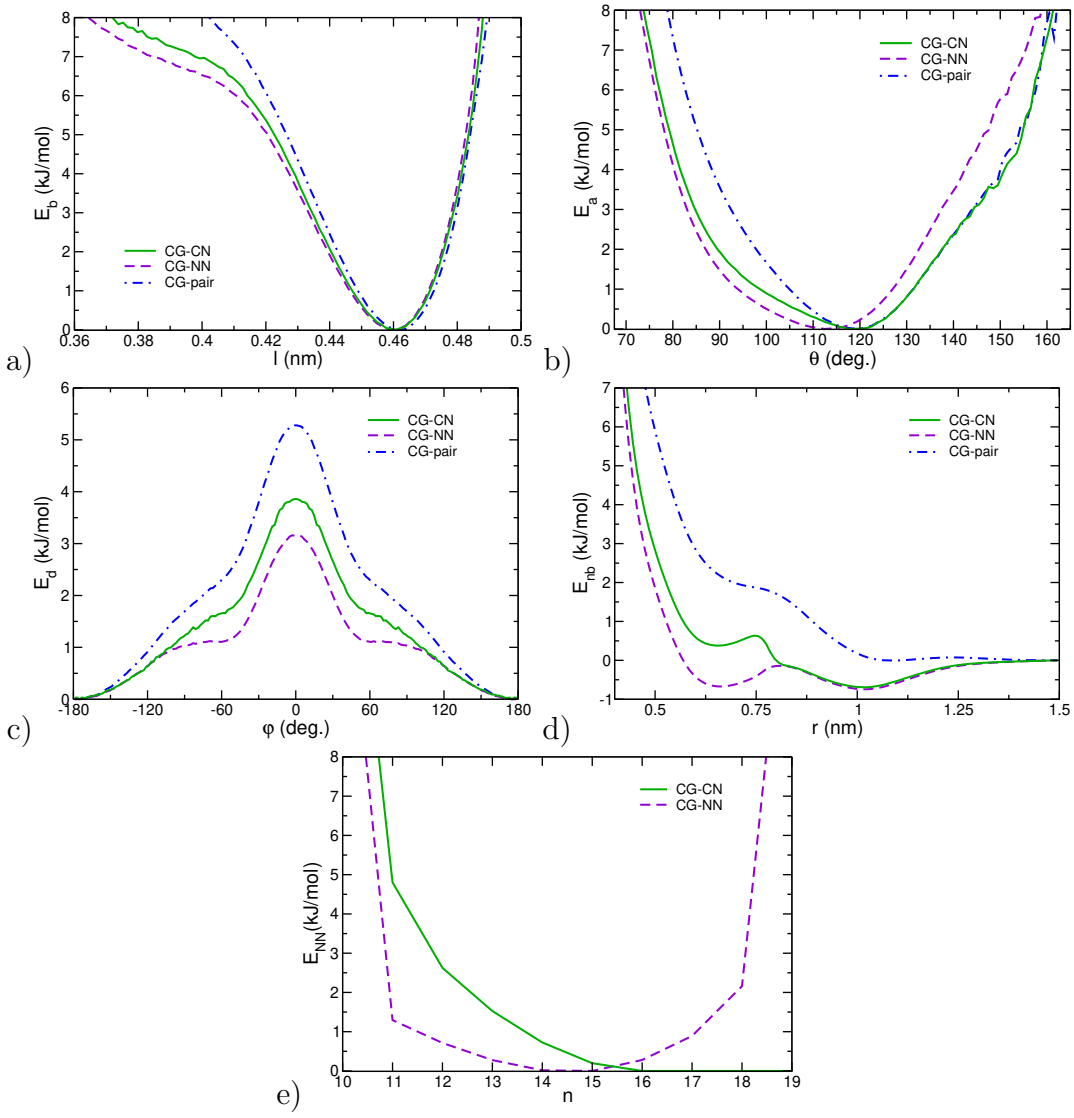


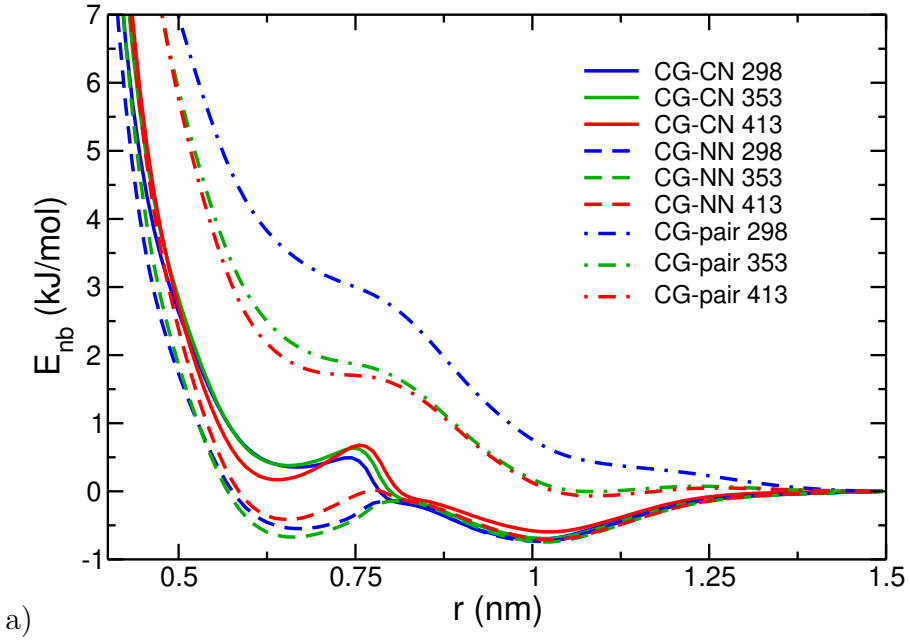
Figure 5.3: a) Bond-stretching, b) Angle-bending, c) Dihedral, d) Pair non bonded, and e) Nearest-neighbor potentials for CG-CN (−), CG-NN (- -) and CG-pair (· - ·) at 353 K.

local volume; using these data the extracted nonbonded potentials after refinement are presented in Fig. 5.4. It is evident that after accounting for the decrease of the local volume (together with remarkably similar distributions of first neighbors, Fig. 5.1a) the nonbonded potentials derived independently at different temperatures are similar but not identical as expected. While a temperature-transferable CG model would be highly desirable we note that the reduced resolution offered by the model (together with the lost entropy of the eliminated degrees of freedom) does come at a cost; as shown in Fig. 5.1a, the spherical approximation of the local volume becomes progressively less accurate therefore additional constraints to capture multiple-state points with a single forcefield could result to reduced quality in matching the target distributions at individual temperatures.

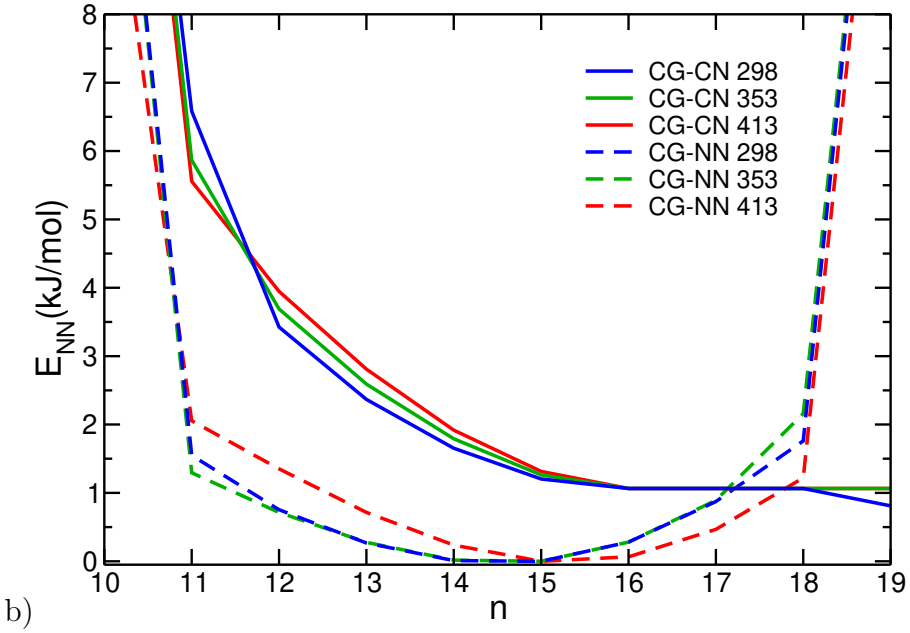
5.3.3 Conformational and thermodynamic properties

We first evaluated the ability of the forcefields to drive CG simulations that exhibit distributions matching those calculated with the atomistic model. In all cases, the method converged to forcefields that were able to reproduce the target distributions with minimal deviations. To demonstrate the successful implementation we present in Fig. 5.5 the distributions using all three models at 298 K compared to the UA target. Note that this is the state point where the largest deviations persisted; in all other cases, the CG model provided an even finer description of target distributions. As it is evident, the CG forcefields are able to capture all essential features recorded with the atomistic model based on the mapping performed. Note however that the shown distribution of nearest neighbors is an approximation based on spherical sampling as discussed previously (and not the one from SANN analysis).

The coarse-graining of polymers aims to facilitate the modeling of long macromolecules. To this extent, it is informative to examine how successive local degrees of freedom vary using common measures as the distribution of internal separations as well as the chain end-to-end distance. The average separation of internal segments cast in the form of characteristic ratio is presented in Figure 5.6a. As seen all models capture well the average distances in close agreement with polyisoprene's conformation [164]. Beyond a small number of monomers, the chains resemble Gaussian coils; the whole distribution of chain end-to-end distances is



a)



b)

Figure 5.4: a) Pair nonbonded and b) nearest-neighbor potentials for CG-NN (−) and CG-CN (- -) at 298 K (blue), 353 K (green) and 413 K (red).

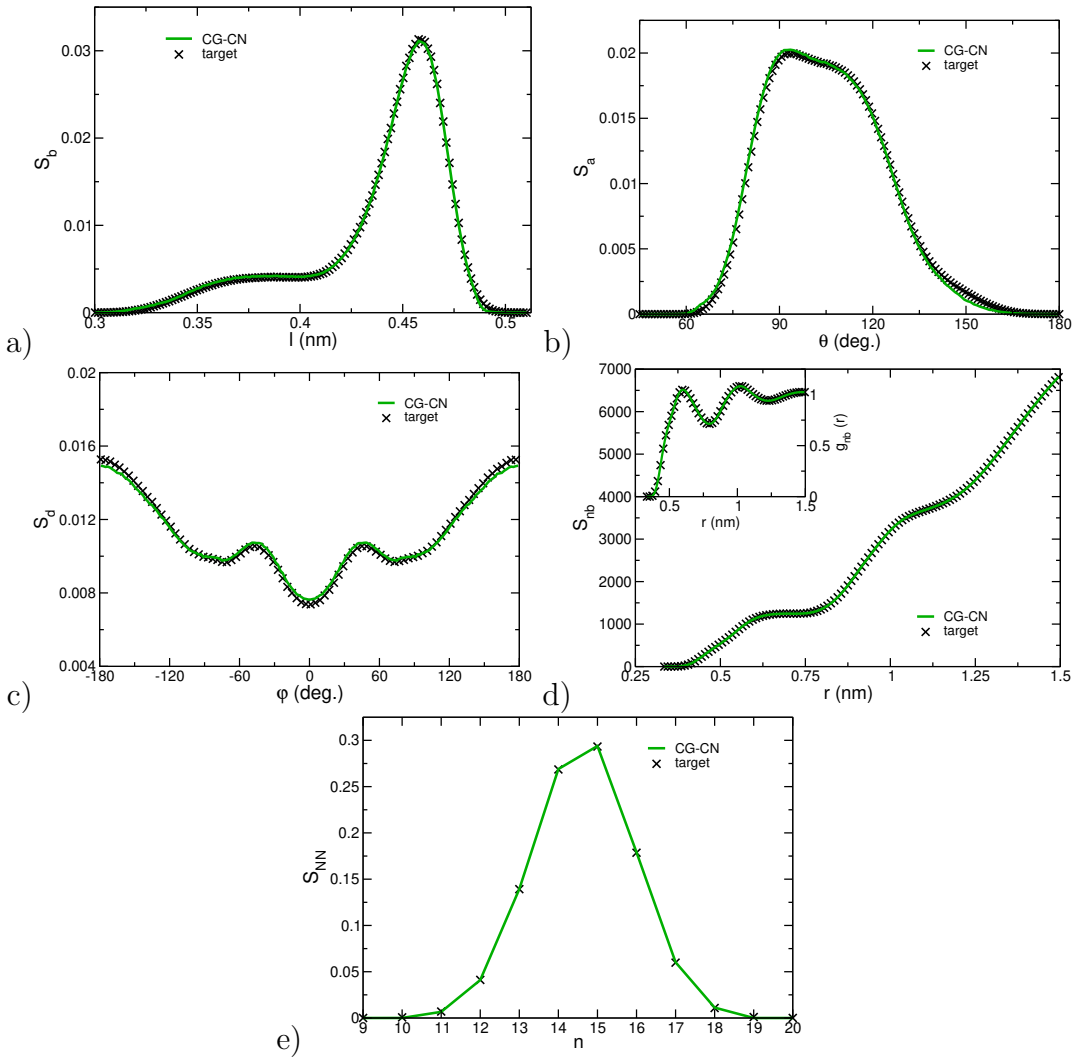


Figure 5.5: Distributions produced by the CG-CN forcefield (lines) and the mapped atomistic trajectory (symbols) at 298 K. At higher temperatures, the comparison was even more favorable.

presented in Figure 5.6b where again a quantitative match between all models is observed. However, if we consider the separation between a small number of segments (1-4, interacting via dihedral and density potential terms) we find that while the coarse-grain models capture the average separation (see Figure 5.6a) they fail to quantitatively describe the distribution of distances. Obviously capturing the dihedral distribution (internal coordinates) does not guarantee a similar result in Cartesian coordinates. Atomistic models retain excluded volume between repeat units separated by three monomers while we opted to exclude such interactions between corresponding coarse-grain beads. Another option would be to include direct nonbonded interactions however we found that the general nonbonded potential is not necessarily applicable between such pairs. In fact, even in atomistic forcefields the inclusion of a portion of nonbonded interactions between atoms interacting via the dihedral potential is a design variable. Given the satisfactory agreement for average separations as well as their distributions when examining segments separated by more CG bonds we chose the scheme with no 1-4 nonbonded interactions. It is also important to emphasize another feature present in our study with regards to 1-4 pairs: based on the data from mapped atomistic trajectory such segments switch between the first and second solvation shell of each other (symbols in Fig. 5.6c). This further cautions that the development of the CG forcefield is subject to the coupling between individual terms and supports the selection of an indicator function that clearly distinguishes between the two populations.

Finally, we compared the predictions of all three CG models on PI's thermodynamic properties. The CG-pair model performs satisfactorily with regards to structure and conformational properties at the target density, i.e., $R_g \approx 1.35$ at 413 K. However, it overestimates the pressure by three orders of magnitude, $P \approx 5{\times}10^3$ bar. Introducing the nearest-neighbor potentials does not only help to drive the system to the target density (inset in Fig. 5.2a) under an optimization process within the NPT ensemble but also assists in capturing density fluctuations. The isothermal compressibility was calculated using [213]:

$$\kappa_T = \frac{\langle V^2 \rangle - \langle V \rangle^2}{k_B T \langle V \rangle} \tag{5.9}$$

Table 5.2: Comparison of density (ρ) and isothermal compressiblity (κ_T) of CG models with UA for various temperatures (T) at 1 bar.

T (K)	413			353			298		
Model	UA	CG-CN	CG-NN	UA	CG-CN	CG-NN	UA	CG-CN	CG-NN
ρ (kg/m^3)	836	835	836	866	866	866	894	894	894
κ_T (10^{-5} bar^{-1})	10.0	9.9	9.6	9.3	8.2	10.0	8.7	11.7	10.3

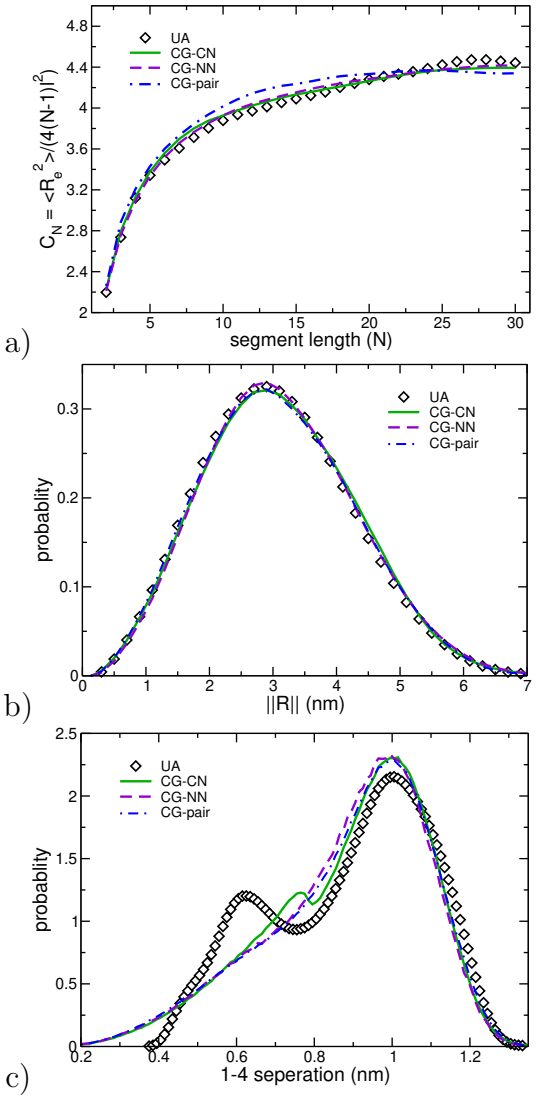


Figure 5.6: a) Characteristic ratio (C_N) as a function of monomer distance (N) in a chain with 30 repeat units, b) distribution of chain end-to-end distances, and c) distribution of distances for CG beads separated by three bonds for mapped UA and CG models (CG-NN, CG-CN, and CG-pair) at 353 K.

The CG-NN and CG-CN models reproduce both the atomistic density and volume fluctuations with an excellent agreement, i.e. $\rho \approx 835$ kg/m^3 and isothermal compressibility κ_T $\approx 9.6\times10^{-5}$ bar^{-1} for the CG-NN model in the NPT ensemble at 1 bar and 413 K. Table 5.2 presents the thermodynamic and conformations properties predicted by the CG-NN and CG-CN models at three temperatures compared to the UA model. It is important to emphasize that in contrast to techniques that add potential terms to the extensive volume of the system (or density) herein, we aimed at capturing the fluctuations at local length scales; therefore it is not guaranteed that volume fluctuations would be matched. In fact, upon close inspection we find that the atomistic model predicts a decrease of compressibility as we move to lower temperatures; this trend does not appear in the CG model. We attribute this disagreement to the non-spherical packing of neighbors (or the limitation of a spherical description of CG beads) as well as to potential coupling between neighboring solvation shells. At lower temperatures, we anticipate that the correlation length increases while the solvation shells over which the many-body term applies become progressively smaller (Fig. 5.2d). Despite these small deviations, the agreement between the models is remarkable given the challenges present to capture both density and fluctuations with simpler CG models [162].

5.3.4 Dynamics

In this section, we examined the ability of the different CG models to qualitatively predict the dynamics of the atomistic PI system. The main advantage of coarse-graining in polymers is the increase in length and time scales accessible by simulations. However, as discussed in the Introduction, the direct use of the "raw" CG data for the quantitative predictions of polymer dynamics is not straightforward due to the use of softer effective CG potentials. Indeed, as a consequence of the softening of the energy landscape at the mesoscopic description, and the fact that we neglect the friction and random forces, [153, 146] the time in the dynamic CG simulations does not correspond to the real-time of the underlying polymeric system and has to be properly scaled. For systems characterized by scalar friction, such as the homopolymer melts studied here, the scaling parameter (τ) is expected to be a scalar

variable, and corresponds, in the long time regime, to the ratio between the atomistic friction coefficient and the one in the CG description [214, 215].

$$\tau = \frac{\zeta_{AT}}{\zeta_{CG}} \tag{5.10}$$

Due to the complex and strongly fluctuating potential energy surface (PES), it is not possible to derive an analytical prediction of τ. Thus, typically τ is calculated either from experimental data or from detailed atomistic simulations [214, 215]. Here, we used data from the UA MD simulations and matched the mean square displacement (MSD) of the CG particles over a considerable time, where both amplitude and shape coincide. Thus, the derived scaling factor determines the real-time unit to which the CG time corresponds. In addition, such a methodology provides direct insight into the spatio-temporal scales the particular CG simulation can be used for. The MD simulations for the CG-pair model were performed in the NVT ensemble at the corresponding UA density while all other simulations were performed in the NPT ensemble at 1 bar.

Mean square displacement

We compared the segmental (monomer) and chain center-of-mass MSD of PI from the UA and the different CG MD simulations at different temperatures in Fig. 5.7. In all cases, the CG data are scaled with a scaling factor, τ, obtained by overlapping the CG and the atomistic curves in the long-time (Fickian) regime. Note that although the simulation lengths are shorter than the time scale of the Fickian regime, the scaling factors for the segmental and chain MSD have similar values at the observed time. In Fig. 5.7a, for the two density-dependent CG models, CG-NN and CG-CN, we see that segmental $\tau = 20 \pm 3$; i.e. for this specific system and state point, the CG model exhibits segmental dynamics that is about 20 times faster than the more accurate atomistic one.

It is clear from the data shown in Fig. 5.7 that atomistic and CG dynamics overlap for length scales around 0.35 nm (MSDs of 0.1 nm^2) for both chain and segmental MSD at all temperatures. This length scale corresponds to the size of the PI monomer (similar to CG bead in the current 1:1 mapping). This is not surprising if we consider that a CG

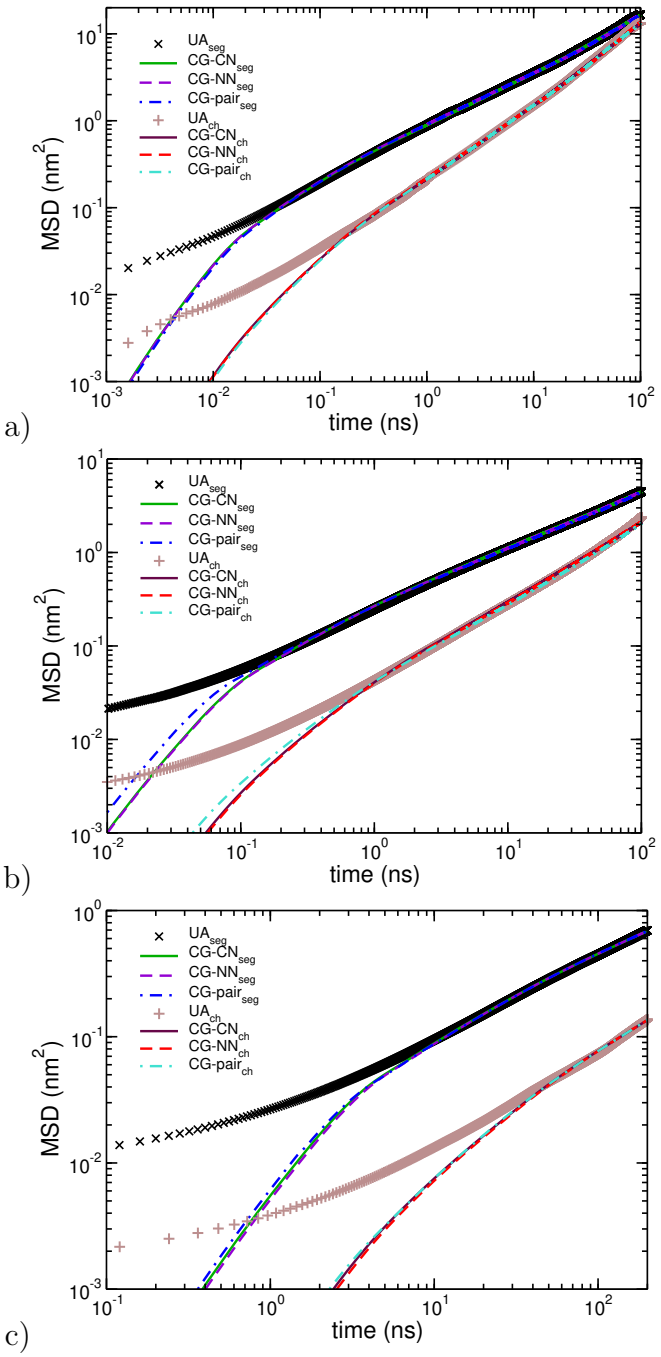


Figure 5.7: Mean square displacement (MSD) for the segment (monomer) and chain center-of-mass from UA and CG simulations (CG-CN, CG-NN, and CG-pair) at different temperatures: a) 413 K, b) 353 K and c) 298 K.

model is not expected to accurately capture the displacement of the COM of the CG bead at distances shorter than its size therefore it will underestimate such short-length displacement due to the lack of necessary degrees of freedom. The time scale where segmental MSD curves overlap is expected to be of the same order of magnitude as the characteristic time of the CG bead length scale and increases as temperature decreases from around 0.04 ns at 413 K to about 10 ns at 298 K. Such a time scale for segmental dynamics is similar to the $\alpha-$relaxation time in PI which is about 0.04 ns for the UA model at 413 K. The chain MSDs overlap at times above 0.1 ns at 413 K. The CG time scaling does not need to be performed in the diffusive regime, since atomistic and CG MSD curves follow each other even for shorter times. This is due to the fact that our CG model is rather close to the underlying chemistry, i.e. a CG bead corresponds to a PI monomer. Such, a behavior has been observed in the past for other polymers as well [153, 214]. Interestingly, the CG-pair potential gives rather similar dynamics. However, note that the latter is performed in the NVT ensemble; since as previously mentioned the NPT simulations with this model do not yield the correct density. Thus, for the above spatio-temporal scales the proposed density-dependent CG model describes correctly, after scaling, both the segmental and the chain translation dynamics of the PI melts as predicted by the atomistic simulations.

The scaling factor is the same for chain and segmental MSDs (within the error) but varies greatly with temperature; from around 20 at 413 K, becomes about 100 at 353 K, up to about 4000 at 298 K. Such a strong temperature dependence of the parameter τ has been observed before for other CG polymer models [216] and since the friction coefficient is inversely proportional to diffusivity the decrease of temperature causes a more pronounced deceleration of the Brownian dynamics of atomistic chains as compared to the CG ones. Finally, we should note that as temperature decreases, approaching T_g, it is clear that the atomistic short-time (below 1 ps) dynamics become more heterogeneous; these motions clearly cannot be captured by the CG model since they correspond to length scales below the size of the CG bead (PI monomer). Note also that the time mapping is very similar if a dynamical quantity describing the orientational dynamics, such as the chain end-to-end vector auto-correlation function, is used.

Overall, the possibility to describe accurately the Brownian motion of a PI chain at such small length and short time scales is one of the advantages of the present CG model and is directly related to the chosen mapping (1:1) scheme, which allows the model to be close to the atomistic structure. However, we should note that as temperature decreases, approaching T_g, it is clear that the atomistic local (segmental) dynamics of PI become more heterogeneous for very short length scales; see atomistic MSD data of about 0.1 nm^2 in Fig. 5.7c. Such dynamical heterogeneities are related to local motions, such as bond vibrations and angle librations, which clearly cannot be captured by the CG model since they correspond to length scales below the size of the CG bead. This observation supports the importance of the atomistic detail in order to describe local dynamical modes of PI, particularly at low temperatures; note though that the CG models can still be practical by providing initial starting points for backmapping procedures.

Dynamic structure factor

The previous analysis examined the ability of the CG models considered in this work, to predict the translational dynamics of PI chains (quantified via the MSDs) at the segmental and chain-center-of-mass level, using as a reference the data from the detailed atomistic simulations. Another quantity that typically probes molecular motions at multiple length scales is the coherent dynamic structure factor $S(q,t)$ (measured directly by neutron spin echo, NSE experiments), defined as:

$$S(q,t) = \frac{1}{N}\sum_{i=1}^{N}\sum_{j=1}^{N}\frac{\sin(qr_{ij}(t))}{qr_{ij}(t)}/S(q,0) \tag{5.11}$$

The above equation can be used to extract $S(q,t)$ directly, using the configurations that are stored during the MD simulations, by recording the time correlation function of segments i and j belonging to the same chain [217, 218, 219]. The advantage of $S(q,t)$ is that by varying the value of the scattering vector q the dynamics over distinct length scales can be studied and compared between different models.

Fig. 5.8 shows the normalized single-chain dynamic structure factor $S(q,t)$ for different values of the scattering vector (q = 3, 6, 9, and 12 nm^{-1}) as extracted by the mapped

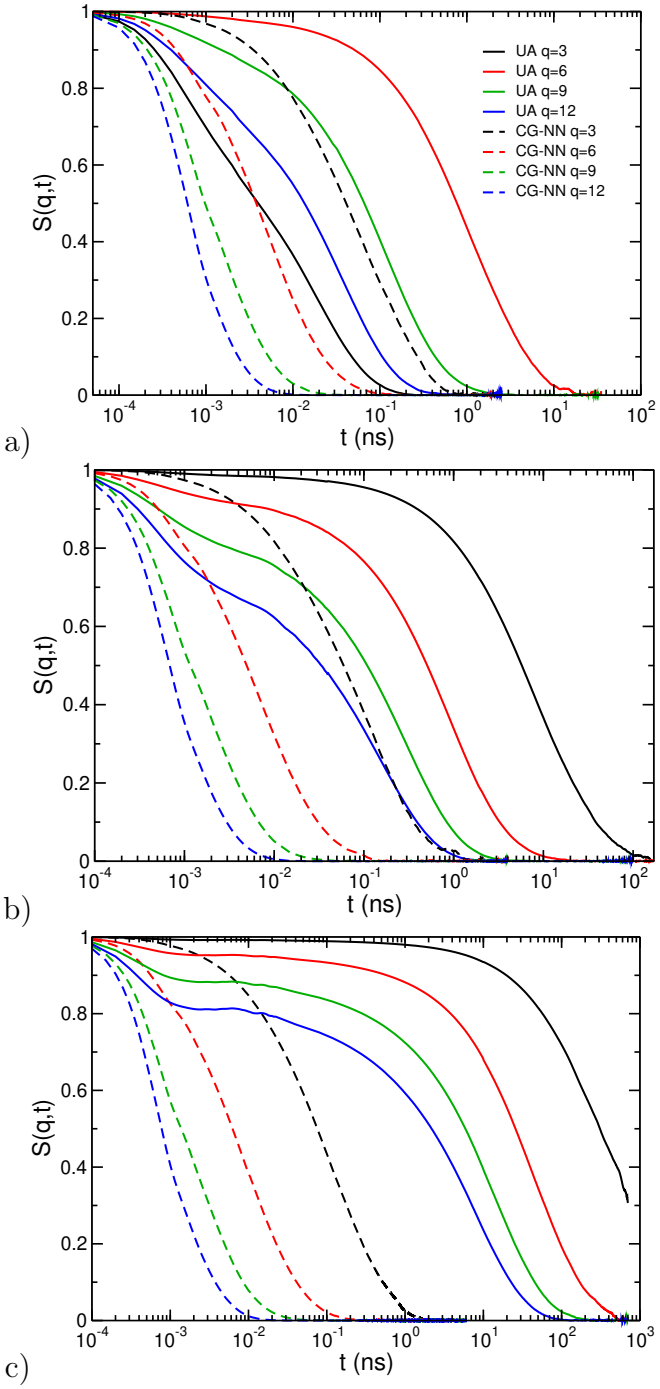


Figure 5.8: Single chain dynamic structure factor S(q,t) from UA and CG-NN models at $q = 3, 6, 9$, and 12 nm^{-1}, at different temperatures: a) 413 K, b) 353 K and c) 298 K.

atomistic trajectory and the CG density dependent *NPT* simulations, at 413 K. All three CG models have very similar dynamics as shown in MSD data, so in the following, we report only the data from the CG-NN simulations. Note, that the first peak of the static structure factor $S(q)$ occurs at $q = 18$ nm^{-1}. Moreover, as it was shown by Moe and Ediger [217] for high q values (above 12 nm^{-1}) the total coherent $S(q,t)$ is dominated by intramolecular contributions. The data shown are presented as calculated from the original CG simulations before any time re-scaling. Thus, as expected, $S(q,t)$ from the CG models decorrelate much faster than the atomistic ones.

A convenient dynamical quantity, used typically in NSE experiments to describe the relaxation of over associated length scales of the polymer chain, is a characteristic time τ_{NSE} defined as the area under a curve of $S(q,t)$. To compute τ_{NSE} values from the atomistic and the CG-NN dynamic simulations, we modeled the curves shown in Fig. 5.8 using two terms, a fast exponential and a slower stretched exponential one:

$$S(q,t) = \alpha \exp(-t/\tau_0) + (1-\alpha)\exp(-(t/\tau_1)^{\beta}) \tag{5.12}$$

Fig. 5.9 shows the relaxation time τ_{NSE}, for various q values, derived via the above procedure for both the UA, τ_{NSE}^{UA}, and the CG, τ_{NSE}^{CG}, PI models. As q increases, $S(q,t)$ describes the dynamics at smaller length scales of a polymer chain and as expected the dynamics become faster, i.e. the characteristic time τ_{NSE} decreases. For example, τ_{NSE} from the atomistic simulations at 413 K ranges from about 2 ns for $q = 3$ nm^{-1} to about 20 ps for $q = 12$ nm^{-1}. The CG models follow the same trend for different q values supporting further that similar dynamic characteristics are probed by the two models.

As a final check of the consistency of the CG density-dependent PI models to reproduce qualitatively, the PI dynamics at multiple length scales, we report in Fig. 5.9 the $\tau_{NSE}^{UA}/\tau_{NSE}^{CG}$ ratios for all systems studied here. For each temperature the ratio $\tau_{NSE}^{UA}/\tau_{NSE}^{CG}$ is very similar to the time mapping factor, τ, reported above (see Fig. 5.7). This is not surprising since the relaxation of $S(q,t)$ is a measure of the Brownian motion of the PI chains, and as mentioned above, τ is a measure of the ratio between the atomistic and the CG PI friction coefficient (Eq. 5.10). Nevertheless, it is interesting that the ratio $\tau_{NSE}^{UA}/\tau_{NSE}^{CG}$ does not depend on the

value of the q vector. This is a clear indication that the CG models predict consistently the long-time dynamics of bulk PI, at multiple length scales, from the chain dimension (radius of gyration) down to the size of a CG bead. However, naturally, there are differences between S(q,t) of atomistic and CG PI in the short time regime, as shown in Fig. 5.8. This is clear in the first local decay of the atomistic model, which develops with increasing q and decreasing T, while it is absent in the CG one. The above is in agreement with the short-time heterogeneous segmental dynamics of the atomistic PI at lower temperatures (see Fig. 5.7), which, as mentioned above, cannot be described by the CG model.

Finally, note the strong dependence of $\tau_{NSE}^{UA}/\tau_{NSE}^{CG}$ on temperature. Similar to the scaling factor τ, it varies from around 20 for the higher temperature (413 K) up to several thousand for the lower one (298 K). Such a strong temperature dependence further emphasizes the different temperature dependence of the friction factor of the atomistic and CG models.

5.4 Conclusions

We developed three CG models for polyisoprene melts and demonstrated the application of multi-body neighbor potentials based on the local environment proposed by a more detailed united atom model. We introduced such interaction terms through an order parameter with a well-defined free energy minimum ($\approx 14-15$ first neighbors) based on geometric analysis. Nearest-neighbor potentials facilitate CG forcefield development by driving the system to the target density under constant pressure simulations in addition to offering another set of parameters to improve matching the target distributions.

The implementation of many-body potentials is a developing area with several options to be explored such as the applicability of isotropic sampling of nearest-neighbors, the range and shape of the introduced indicator function, the shape of the multi-body potential, and most importantly the algorithm to be employed to develop such terms. All these options play a prominent role in the success of this approach. For the system studied herein, at all state points examined, we found that solely attractive multi-body interactions and isotropic sampling suffice to provide an accurate description of the structure at all but the lowest temperature point. We observed small deviations at 298 K (both in terms of spherical

packing as well as in the compressibility of the CG system), indicating that there could be cases where improvements might be sought with on-the-fly calculations of the nearest-neighbors. This was also the motivation for the original design of the SANN algorithm. We found that a purely attractive multi-body term performs equally well to one that presents a clear minimum; the nonbonded pair interactions adjust accordingly to match the target distributions. In regards to the algorithm, it is important to emphasize that the application of the Inverse Monte Carlo method, despite the numerical challenges it imposes, offers clear advantages over the sequential refinement of each potential term. Beyond the clear coupling between pair and multi-body nonbonded terms, we have demonstrated that for polymers additional complications arise; i.e. the dihedral potential can be coupled to the nearest-neighbor distributions.

Furthermore, we have characterized the dynamics of the developed CG models at different temporal and length scales. We found that in all cases, the dynamics were accelerated with a ratio that is highly sensitive to the temperature studied. Most importantly, we provided evidence that the introduction of the many-body term did not alter the character of the relaxation modes probed at different scattering vectors.

The bottom-up coarse-graining methodology for PI presented here, is, in general, applicable to other polymeric systems. From the methodology point of view we would like to relate the hybrid particle-density field CG polymer models, as the one presented here, with many-body CG potentials based on rigorous re-normalization group theory approaches, such as the cluster expansion techniques [183]. In addition, future studies will focus both on improving temperature transferability and exploring different systems, *i.e.* polymer mixtures, copolymers, or heterogeneous nanostructured systems in the presence of polymer/solid or polymer/liquid interfaces [220, 221, 143, 142]. The development and implementation of multi-body interaction terms for such systems present significant potential as well as challenges.

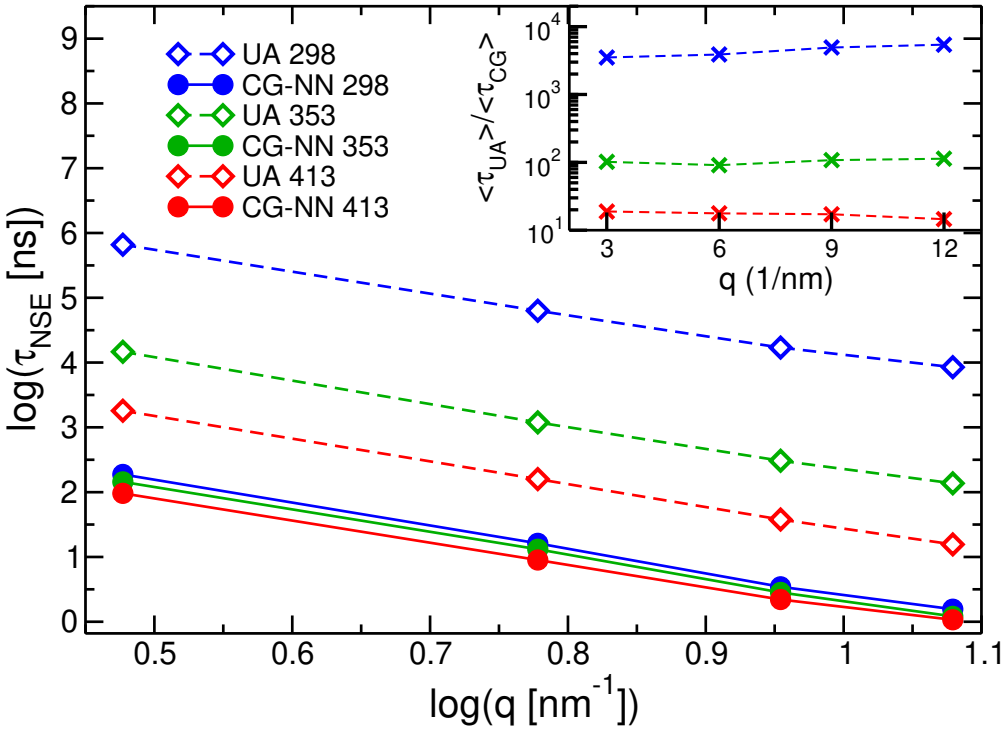


Figure 5.9: Average relaxation time of the single chain structure factor (τ_{NSE}) as a function of the scattering vector (q) at 413 K (red), 353 K (green), and 298 K (blue).

Chapter 6

Conclusions

This work focuses on the use of chemically specific models to provide insight into molecular mechanisms and predict the properties of polymers from their atomistic structure.

In chapter 2, we employed atomistic simulations to directly probe molecular motion throughout free PVAC thin films on silica. The simulations determined the range of interfacial effects on segmental dynamics and showed the existence of an additional relaxation mode in the adsorbed layer. Although simulations provided direct insight into molecular motions of PVAC oligomers, due to high correlation times at the adsorbed surface, we were limited to simulating comparatively short chains and high temperatures which made direct comparison with experimental observations difficult.

PNB are unique rigid polymers with various applications but due to experimental challenges, the effect of stereochemistry on their macroscopic properties is unclear. To derive the structure-property relationship for unsubstituted and alkyl-substituted PNB, we first employed an atomistic forcefield. Since many general forcefields do not perform well for PNB, in chapter 3 we used DFT results to inform the choice and optimization of the atomistic model. Due to the high T_g of PNB, we first performed simulations of short chains at high temperatures and showed that racemo chains form helical structures while meso chains are larger and more rigid with faster diffusion. Consequently, we derived a bottom-up coarse-grained model for different tacticities to derive the properties at high molecular weights. In chapter 4, we extended our study to the effect of alkyl side chains with different molecular weights. We showed that as the length of the side chain increases, thermodynamic

and dynamic properties become less dependent on backbone tacticity. Ongoing work for this system includes the development of coarse-grained models that can predict longer-scale dynamics such as zero-shear viscosity.

Finally in chapter 5, we developed a unique method for systematic bottom-up coarse-graining of polymers that improves the thermodynamic representability of the coarse-grained model by introducing a many-body potential term. The model was derived for *cis*-1,4 PI at different temperatures. Although our CG models did not show temperature transferability, they accurately represented several features such as density, thermal coefficient, structure, and dynamics. The method shows promise for application in more challenging systems such as mixtures and copolymers.

Bibliography

[1] Stephen A Burrows, Ivan Korotkin, Stoyan K Smoukov, Edo Boek, and Sergey Karabasov. Benchmarking of molecular dynamics force fields for solid–liquid and solid–solid phase transitions in alkanes. *The Journal of Physical Chemistry B*, 125(19):5145–5159, 2021. x, xii, xiii, 21, 25, 26, 27, 29, 42

[2] Jeffery B Klauda, Richard M Venable, J Alfredo Freites, Joseph W O'Connor, Douglas J Tobias, Carlos Mondragon-Ramirez, Igor Vorobyov, Alexander D MacKerell Jr, and Richard W Pastor. Update of the charmm all-atom additive force field for lipids: validation on six lipid types. *The journal of physical chemistry B*, 114(23):7830–7843, 2010. x, 25

[3] Kechuan Tu, Douglas J Tobias, and Michael L Klein. Constant pressure and temperature molecular dynamics simulations of crystals of the lecithin fragments: glycerylphosphorylcholine and dilauroylglycerol. *The Journal of Physical Chemistry*, 99(24):10035–10042, 1995. x, 25

[4] Madhusudan Tyagi, Angel Alegría, and Juan Colmenero. Heterogeneous dynamics of poly(vinyl acetate) far above Tg: A combined study by dielectric spectroscopy and quasielastic neutron scattering. *The Journal of Chemical Physics*, 122(24):244909, June 2005. xi, xii, 14, 18

[5] Emmanuel Urandu Mapesa, Nobahar Shahidi, Friedrich Kremer, Manolis Doxastakis, and Joshua Sangoro. Interfacial dynamics in supported ultrathin polymer films—from the solid to the free interface. *The Journal of Physical Chemistry Letters*, 12:117–125, 2020. xii, 5, 6, 13, 15, 18

[6] S Ahmed, Ss A Bidstrup, PA Kohl, and PJ Ludovice. Development of a new force field for polynorbornene. *The Journal of Physical Chemistry B*, 102(49):9783–9790, 1998. xii, 4, 20, 26, 27, 42

[7] Thomas FA Haselwander, Walter Heitz, Stefan A Krügel, and Joachim H Wendorff. Polynorbornene: synthesis, properties and simulations. *Macromolecular Chemistry and Physics*, 197(10):3435–3453, 1996. xii, 4, 19, 20, 26, 27, 42, 43

[8] William L Jorgensen, David S Maxwell, and Julian Tirado-Rives. Development and testing of the opls all-atom force field on conformational energetics and properties of organic liquids. *Journal of the American Chemical Society*, 118(45):11225–11236, 1996. xii, 6, 26, 27

[9] Viktor Hornak, Robert Abel, Asim Okur, Bentley Strockbine, Adrian Roitberg, and Carlos Simmerling. Comparison of multiple amber force fields and development of improved protein backbone parameters. *Proteins: Structure, Function, and Bioinformatics*, 65(3):712–725, 2006. xii, 26, 27

[10] Alyona I Wozniak, Evgeniya V Bermesheva, Ilya L Borisov, Alexey V Volkov, Dmitrii I Petukhov, Natalia N Gavrilova, Victor P Shantarovich, Andrey F Asachenko, Maxim A Topchiy, Eugene Sh Finkelshtein, et al. Switching on/switching off solubility controlled permeation of hydrocarbons through glassy polynorbornenes by the length of side alkyl groups. *Journal of Membrane Science*, 641:119848, 2022. xiii, xiv, 19, 32, 34, 41, 42, 43, 45, 46

[11] Hideki Kai, Atsushi Izumi, Shun Hayakawa, J Alex Niemiec, Carl Ebner, Mike Schofield, Doug Skilskyj, and Larry F Rhodes. Interchain ordering structure and main chain conformation analysis of thermal stability in vinyl-addition polynorbornene. *Polymer*, page 125260, 2022. xiv, 43, 45, 46

[12] Jacobus A. van Meel, Laura Filion, Chantal Valeriani, and Daan Frenkel. A parameter-free, solid-angle based, nearest-neighbor algorithm. *J. Chem. Phys.*, 136(23):234107, 2012. xv, 58, 59

[13] Paul J Flory. Thermodynamics of high polymer solutions. *The Journal of chemical physics*, 9(8):660–660, 1941. 1

[14] Paul J Flory. Thermodynamics of high polymer solutions. *The Journal of chemical physics*, 10(1):51–61, 1942. 1

[15] Maurice L Huggins. Some properties of solutions of long-chain compounds. *The Journal of Physical Chemistry*, 46(1):151–158, 1942. 1

[16] Michael Tambasco, JEG Lipson, and Julia S Higgins. Blend miscibility and the flory-huggins interaction parameter: a critical examination. *Macromolecules*, 39(14):4860–4868, 2006. 1

[17] Julia S Higgins, Jane EG Lipson, and Ronald P White. A simple approach to polymer mixture miscibility. *Philosophical Transactions of the Royal Society A: Mathematical, Physical and Engineering Sciences*, 368(1914):1009–1025, 2010. 1

[18] Piotr Knychała, Ksenia Timachova, Michał Banaszak, and Nitash P Balsara. 50th anniversary perspective: phase behavior of polymer solutions and blends. *Macromolecules*, 50(8):3051–3065, 2017. 1

[19] Aidan P Thompson, H Metin Aktulga, Richard Berger, Dan S Bolintineanu, W Michael Brown, Paul S Crozier, Pieter J in't Veld, Axel Kohlmeyer, Stan G Moore, Trung Dac Nguyen, et al. Lammps-a flexible simulation tool for particle-based materials modeling at the atomic, meso, and continuum scales. *Computer Physics Communications*, 271:108171, 2022. 2

[20] Jörg Baschnagel, Kurt Binder, Pemra Doruker, Andrei A Gusev, Oliver Hahn, Kurt Kremer, Wayne L Mattice, Florian Müller-Plathe, Michael Murat, Wolfgang Paul, et al. Bridging the gap between atomistic and coarse-grained models of polymers: Status and perspectives. *Viscoelasticity, atomistic models, statistical chemistry*, pages 41–156, 2000. 2

[21] VA Harmandaris, NP Adhikari, Nico FA van der Vegt, and Kurt Kremer. Hierarchical modeling of polystyrene: From atomistic to coarse-grained simulations. *Macromolecules*, 39(19):6708–6719, 2006. 2

[22] Wei Li, Craig Burkhart, Patrycja Polińska, Vagelis Harmandaris, and Manolis Doxastakis. Backmapping coarse-grained macromolecules: An efficient and versatile machine learning approach. *The Journal of Chemical Physics*, 153(4):041101, 2020. 2

[23] Dirk Reith, Mathias Pütz, and Florian Müller-Plathe. Deriving effective mesoscale potentials from atomistic simulations. *J. Comput. Chem.*, 24(13):1624–1636, 2003. 2, 3, 23, 53, 57, 61

[24] Alexander P. Lyubartsev and Aatto Laaksonen. Calculation of effective interaction potentials from radial distribution functions: A reverse monte carlo approach. *Phys. Rev. E*, 52:3730–3737, Oct 1995. 2, 61, 62

[25] Sergei Izvekov, Angela Violi, and Gregory A Voth. Systematic coarse-graining of nanoparticle interactions in molecular dynamics simulation. *The Journal of Physical Chemistry B*, 109(36):17019–17024, 2005. 2

[26] WG Noid, Jhih-Wei Chu, Gary S Ayton, Vinod Krishna, Sergei Izvekov, Gregory A Voth, Avisek Das, and Hans C Andersen. The multiscale coarse-graining method. i. a rigorous bridge between atomistic and coarse-grained models. *The Journal of chemical physics*, 128(24):244114, 2008. 2

[27] E Brini and NFA Van der Vegt. Chemically transferable coarse-grained potentials from conditional reversible work calculations. *The Journal of chemical physics*, 137(15):154113, 2012. 2

[28] M Scott Shell. The relative entropy is fundamental to multiscale and inverse thermodynamic problems. *The Journal of chemical physics*, 129(14):144108, 2008. 2

[29] Aviel Chaimovich and M Scott Shell. Coarse-graining errors and numerical optimization using a relative entropy framework. *The Journal of chemical physics*, 134(9):094112, 2011. 2

[30] WG Noid. Perspective: Advances, challenges, and insight for predictive coarse-grained models. *The Journal of Physical Chemistry B*, 2023. 2

[31] Florian Müller-Plathe. Coarse-graining in polymer simulation: from the atomistic to the mesoscopic scale and back. *ChemPhysChem*, 3(9):754–769, 2002. 2, 3

[32] Sergei Izvekov and Gregory A Voth. Multiscale coarse graining of liquid-state systems. *The Journal of chemical physics*, 123(13):134105, 2005. 3

[33] Teemu Murtola, Emma Falck, Mikko Karttunen, and Ilpo Vattulainen. Coarse-grained model for phospholipid/cholesterol bilayer employing inverse monte carlo with thermodynamic constraints. *The Journal of chemical physics*, 126(7):02B607, 2007. 3

[34] Sergei Izvekov, Peter W Chung, and Betsy M Rice. The multiscale coarse-graining method: Assessing its accuracy and introducing density dependent coarse-grain potentials. *The Journal of chemical physics*, 133(6):064109, 2010. 3

[35] Avisek Das and Hans C Andersen. The multiscale coarse-graining method. v. isothermal-isobaric ensemble. *The Journal of chemical physics*, 132(16):164106, 2010. 3

[36] Han Wang, Christoph Junghans, and Kurt Kremer. Comparative atomistic and coarse-grained study of water: What do we lose by coarse-graining? *Eur. Phys. J. E*, 28(2):221–229, Feb 2009. 3, 53

[37] Theodora Spyriouni, Christos Tzoumanekas, Doros Theodorou, Florian Müller-Plathe, and Giuseppe Milano. Coarse-grained and reverse-mapped united-atom simulations of long-chain atactic polystyrene melts: structure, thermodynamic properties, chain conformation, and entanglements. *Macromolecules*, 40(10):3876–3885, 2007. 3, 53

[38] G. Maurel, B. Schnell, F. Goujon, M. Couty, and P. Malfreyt. Multiscale modeling approach toward the prediction of viscoelastic properties of polymers. *J. Chem. Theory Comput.*, 8(11):4570–4579, 2012. 3, 53

[39] Karim Farah, Aoife Catherine Fogarty, Michael Christian Böhm, and Florian Müller-Plathe. Temperature dependence of coarse-grained potentials for liquid hexane. *Physical Chemistry Chemical Physics*, 13(7):2894–2902, 2011. 3

[40] Jussi Katajisto, Mikko Linnolahti, Matti Haukka, and Tapani A Pakkanen. Development of a new force field for property prediction of cyclo-olefin copolymers. *The Journal of Physical Chemistry B*, 108(7):2168–2172, 2004. 4, 26

[41] Rodney D Priestley, Daniele Cangialosi, and Simone Napolitano. On the equivalence between the thermodynamic and dynamic measurements of the glass transition in confined polymers. *Journal of non-crystalline solids*, 407:288–295, 2015. 5

[42] Friedrich Kremer, Martin Tress, and Emmanuel Urandu Mapesa. Glassy dynamics and glass transition in nanometric layers and films: A silver lining on the horizon. *Journal of Non-Crystalline Solids*, 407:277–283, 2015. 5

[43] Wengang Zhang, Jack F Douglas, and Francis W Starr. Why we need to look beyond the glass transition temperature to characterize the dynamics of thin supported polymer films. *Proceedings of the National Academy of Sciences*, 115(22):5641–5646, 2018. 5

[44] Hamid Mortazavian, Christopher J. Fennell, and Frank D. Blum. Structure of the Interfacial Region in Adsorbed Poly(vinyl acetate) on Silica. *Macromolecules*, 49(1):298–307, January 2016. 5, 9

[45] Anastassia N. Rissanou and Vagelis Harmandaris. Dynamics of various polymer–graphene interfacial systems through atomistic molecular dynamics simulations. *Soft Matter*, 10(16):2876–2888, 2014. 6, 9, 13

[46] L. Yelash, P. Virnau, K. Binder, and W. Paul. Slow process in confined polymer melts: Layer exchange dynamics at a polymer solid interface. *Physical Review E*, 82(5):050801, November 2010. 6, 9, 13

[47] L Yelash, P Virnau, K Binder, and W Paul. Three-step decay of time correlations at polymer-solid interfaces. *EPL (Europhysics Letters)*, 98(2):28006, 2012. 6, 9, 13

[48] Mathieu Solar, Kurt Binder, and Wolfgang Paul. Dielectric Relaxation of a Polybutadiene Melt at a Crystalline Graphite Surface: Atomistic Molecular Dynamics Simulations. In Friedrich Kremer, editor, *Dynamics in Geometrical Confinement*, Advances in Dielectrics, pages 1–15. Springer International Publishing, Cham, 2014. 6, 9, 13

[49] R Stannarius, F Kremer, and M Arndt. Dynamic exchange effects in broadband dielectric spectroscopy. *Physical review letters*, 75(25):4698, 1995. 6, 17

[50] M Arndt, R Stannarius, W Gorbatschow, and F Kremer. Dielectric investigations of the dynamic glass transition in nanopores. *Physical Review E*, 54(5):5377, 1996. 6, 17

[51] Michael Vogel. Rotational and conformational dynamics of a model polymer melt at solid interfaces. *Macromolecules*, 42(24):9498–9505, 2009. 6, 17

[52] Herman JC Berendsen, David van der Spoel, and Rudi van Drunen. Gromacs: a message-passing parallel molecular dynamics implementation. *Comput. Phys. Commun.*, 91(1-3):43–56, 1995. 6, 22, 42

[53] Mark James Abraham, Teemu Murtola, Roland Schulz, Szilárd Páll, Jeremy C Smith, Berk Hess, and Erik Lindahl. Gromacs: High performance molecular simulations through multi-level parallelism from laptops to supercomputers. *SoftwareX*, 1:19–25, 2015. 6, 22, 42, 56

[54] Melissa LP Price, Dennis Ostrovsky, and William L Jorgensen. Gas-phase and liquid-state properties of esters, nitriles, and nitro compounds with the opls-aa force field. *Journal of Computational Chemistry*, 22(13):1340–1352, 2001. 6

[55] Pedro EM Lopes, Vladimir Murashov, Mouhsine Tazi, Eugene Demchuk, and Alexander D MacKerell. Development of an empirical force field for silica. application to the quartz- water interface. *The Journal of Physical Chemistry B*, 110(6):2782–2792, 2006. 6

[56] Tinashe V. M. Ndoro, Evangelos Voyiatzis, Azadeh Ghanbari, Doros N. Theodorou, Michael C. Böhm, and Florian Müller-Plathe. Interface of Grafted and Ungrafted Silica Nanoparticles with a Polystyrene Matrix: Atomistic Molecular Dynamics Simulations. *Macromolecules*, 44(7):2316–2327, April 2011. 6, 7

[57] Yogendra Narayan Pandey and Manolis Doxastakis. Detailed atomistic monte carlo simulations of a polymer melt on a solid surface and around a nanoparticle. *J. Chem. Phys.*, 136(9):094901, 2012. 6, 63

[58] H. J. C. Berendsen, J. P. M. Postma, W. F. van Gunsteren, A. DiNola, and J. R. Haak. Molecular dynamics with coupling to an external bath. *The Journal of Chemical Physics*, 81(8):3684–3690, October 1984. 6

[59] Giovanni Bussi, Davide Donadio, and Michele Parrinello. Canonical sampling through velocity rescaling. *The Journal of chemical physics*, 126(1):014101, 2007. 6, 22, 42

[60] David R. Lide and G. W. A. Milne. *CRC Handbook of Data on Organic Compounds*. CRC Press, December 1993. Google-Books-ID: JaQ6b6qCHTIC. 7

[61] James E Mark. *Physical properties of polymers handbook*, volume 1076. Springer, 2007. 7

[62] Stephen W. Provencher. Inverse problems in polymer characterization: Direct analysis of polydispersity with photon correlation spectroscopy. *Die Makromolekulare Chemie*, 180(1):201–209, 1979. 7

[63] Stephen W. Provencher. A constrained regularization method for inverting data represented by linear algebraic or integral equations. *Computer Physics Communications*, 27(3):213–227, September 1982. 7

[64] Stephen W. Provencher. CONTIN: A general purpose constrained regularization program for inverting noisy linear algebraic and integral equations. *Computer Physics Communications*, 27(3):229–242, September 1982. 7

[65] Graham Williams and David C. Watts. Non-symmetrical dielectric relaxation behaviour arising from a simple empirical decay function. *Transactions of the Faraday Society*, 66(0):80–85, 1970. 9

[66] S Negami, R. J Ruch, and R. R Myers. The dielectric behavior of poly(vinyl acetate) as a function of molecular weight. *Journal of Colloid and Interface Science*, 90(1):117–126, November 1982. 10

[67] S Havriliak and S Negami. A complex plane representation of dielectric and mechanical relaxation processes in some polymers. *Polymer*, 8:161–210, 1967. 15

[68] Hans Vogel. Das temperaturabhangigkeitsgesetz der viskositat von flussigkeiten. *Phys. Z.*, 22:645–646, 1921. 17

[69] Gordon S Fulcher. Analysis of recent measurements of the viscosity of glasses. *Journal of the American Ceramic Society*, 8(6):339–355, 1925. 17

[70] GHWZ Tammann and W Hesse. Die abhängigkeit der viscosität von der temperatur bie unterkühlten flüssigkeiten. *Zeitschrift für anorganische und allgemeine Chemie*, 156(1):245–257, 1926. 17

[71] Christoph Janiak and Paul G Lassahn. Metal catalysts for the vinyl polymerization of norbornene. *Journal of molecular catalysis A: chemical*, 166(2):193–209, 2001. 19, 20

[72] Frederik Blank and Christoph Janiak. Metal catalysts for the vinyl/addition polymerization of norbornene. *Coordination Chemistry Reviews*, 253(7-8):827–861, 2009. 19, 42

[73] Rui Ma, Yubang Hou, Jie Gao, and Feng Bao. Recent progress in the vinylic polymerization and copolymerization of norbornene catalyzed by transition metal catalysts. *Journal of Macromolecular Science®, Part C: Polymer Reviews*, 49(3):249–287, 2009. 19

[74] Xiangyang Song, Lixin Cao, Ryo Tanaka, Takeshi Shiono, and Zhengguo Cai. Optically transparent functional polyolefin elastomer with excellent mechanical and thermal properties. *ACS Macro Letters*, 8(3):299–303, 2019. 19

[75] Xinyi Wang, Yewon L Jeong, Christopher Love, Holly A Stretz, Gila E Stein, and Brian K Long. Design, synthesis, and characterization of vinyl-addition polynorbornenes with tunable thermal properties. *Polymer Chemistry*, 12(40):5831–5841, 2021. 19, 32, 41, 43

[76] M Gringolts, M Bermeshev, Yu Yampolskii, L Starannikova, V Shantarovich, and E Finkelshtein. New high permeable addition poly (tricyclononenes) with si (ch3) 3 side groups. synthesis, gas permeation parameters, and free volume. *Macromolecules*, 43(17):7165–7172, 2010. 19

[77] Evgenii Sh Finkelshtein, Maksim V Bermeshev, Mariya L Gringolts, LE Starannikova, and Yu P Yampolskii. Substituted polynorbornenes as promising materials for gas separation membranes. *Russian Chemical Reviews*, 80(4):341, 2011. 19

[78] Eugene Finkelshtein, Maria Gringolts, Maksim Bermeshev, Pavel Chapala, and Yulia Rogan. Polynorbornenes. *Membrane Materials for Gas and Vapor Separation: Synthesis and Application of Silicon-Containing Polymers*, pages 143–221, 2017. 19, 41

[79] Wouter Dujardin, Cédric Van Goethem, Julian A Steele, Maarten Roeffaers, Ivo FJ Vankelecom, and Guy Koeckelberghs. Polyvinylnorbornene gas separation membranes. *Polymers*, 11(4):704, 2019. 19

[80] Alyona I Wozniak, Evgeniya V Bermesheva, Fedor A Andreyanov, Ilya L Borisov, Danil P Zarezin, Danila S Bakhtin, Natalia N Gavrilova, Igor R Ilyasov, Mikhail S Nechaev, Andrey F Asachenko, et al. Modifications of addition poly (5-vinyl-2-norbornene) and gas-transport properties of the obtained polymers. *Reactive and Functional Polymers*, 149:104513, 2020. 19, 41

[81] Xinyi Wang, Trevor J Wilson, Dmitry Alentiev, Maria Gringolts, Eugene Finkelshtein, Maxim Bermeshev, and Brian K Long. Substituted polynorbornene membranes: a modular template for targeted gas separations. *Polymer Chemistry*, 12(20):2947–2977, 2021. 19, 41

[82] Xinyi Wang, Trevor J Wilson, Christopher R Maroon, Jeffrey A Laub, Savannah E Rheingold, Konstantinos D Vogiatzis, and Brian K Long. Vinyl-addition fluoroalkoxysilyl-substituted polynorbornene membranes for co2/ch4 separation. *ACS Applied Polymer Materials*, 2022. 19

[83] Nicole R Grove, Paul A Kohl, Sue Ann Bidstrup Allen, Saikumar Jayaraman, and Robert Shick. Functionalized polynorbornene dielectric polymers: adhesion and mechanical properties. *Journal of Polymer Science Part B: Polymer Physics*, 37(21):3003–3010, 1999. 19, 32, 41

[84] Mehrsa Raeis-Zadeh and Paul A Kohl. High-contrast, high-sensitivity aqueous base-developable polynorbornene dielectric. *Journal of applied polymer science*, 127(6):4366–4373, 2013. 19

[85] Xiaohui He, Jingyin Liu, Hongyu Zhu, Yan Zheng, and Defu Chen. Novel quaternary ammonium functional addition-type norbornene copolymer as hydroxide-conductive and durable anion exchange membrane for direct methanol fuel cells. *RSC Advances*, 5(78):63215–63225, 2015. 19

[86] Mrinmay Mandal, Garrett Huang, and Paul A Kohl. Anionic multiblock copolymer membrane based on vinyl addition polymerization of norbornenes: Applications in anion-exchange membrane fuel cells. *Journal of Membrane Science*, 570:394–402, 2019. 19

[87] Mrinmay Mandal, Garrett Huang, and Paul A Kohl. Highly conductive anion-exchange membranes based on cross-linked poly (norbornene): vinyl addition polymerization. *ACS Applied Energy Materials*, 2(4):2447–2457, 2019. 19

[88] Mrinmay Mandal, Garrett Huang, Noor Ul Hassan, William E Mustain, and Paul A Kohl. Poly (norbornene) anion conductive membranes: homopolymer, block copolymer and random copolymer properties and performance. *Journal of Materials Chemistry A*, 8(34):17568–17578, 2020. 19

[89] Ryan Selhorst, Jamie Gaitor, Minjung Lee, Danielle Markovich, Yue Yu, Megan Treichel, Che Olavarria Gallegos, Tomasz Kowalewski, Lena F Kourkoutis, Ryan C Hayward, et al. Multiblock copolymer anion-exchange membranes derived from vinyl addition polynorbornenes. *ACS Applied Energy Materials*, 4(9):10273–10279, 2021. 19

[90] Michelle Lehmann, Daniel Leonard, Jackie Zheng, Lilin He, Xiaomin Tang, Xi Chelsea Chen, Katie Heeyum Lim, Sandip Maurya, Yu Seung Kim, and Tomonori Saito. Quaternized polynorbornene random copolymers for fuel cell devices. *ACS Applied Energy Materials*, 0(0):null, 0. 19

[91] Kokou D Dorkenoo, Peter H Pfromm, and Mary E Rezac. Gas transport properties of a series of high tg polynorbornenes with aliphatic pendant groups. *Journal of Polymer Science Part B: Polymer Physics*, 36(5):797–803, 1998. 19, 41, 43

[92] John A Lawrence III, Daniel J Harrigan, Christopher R Maroon, Seth A Sharber, Brian K Long, and Benjamin J Sundell. Promoting acid gas separations via strategic alkoxysilyl substitution of vinyl-added poly (norbornene) s. *Journal of Membrane Science*, 616:118569, 2020. 19, 41

[93] Xiaohui He, Jianhua Zou, Yufei Wen, Bin Wu, Xiujing Zang, Jiahao Deng, Zengwei Qin, Guoxiao Yang, Jiang Xu, and Defu Chen. Preparation and performance of bisimidazole cationic crosslinked addition-type polynorbornene-based anion exchange membrane. *International Journal of Hydrogen Energy*, 47(1):69–80, 2022. 19, 41

[94] Brian L Goodall, George M Benedikt, Lester H McIntosh III, and Dennis A Barnes. Process for making polymers containing a norbornene repeating unit by addition polymerization using an organo (nickel or palladium) complex, November 21 1995. US Patent 5,468,819. 19, 41

[95] Eun Chae Kim, Myung-Jin Kim, Linh Nguyet Thi Ho, Woohwa Lee, Jae-Won Ka, Dong-Gyun Kim, Tae Joo Shin, Kang Moo Huh, Sungmin Park, and Yong Seok Kim. Synthesis of vinyl-addition polynorbornene copolymers bearing pendant n-alkyl chains and systematic investigation of their properties. *Macromolecules*, 54(14):6762–6771, 2021. 19, 41, 42, 43, 45

[96] Broderick R Wilks, Won J Chung, Peter J Ludovice, Mary E Rezac, Pavla Meakin, and Anita J Hill. Structural and free-volume analysis for alkyl-substituted palladium-catalyzed poly (norbornene): A combined experimental and monte carlo investigation. *Journal of Polymer Science Part B: Polymer Physics*, 44(1):215–233, 2006. 19, 21, 41, 42, 43, 45

[97] Adnan S Abu-Surrah, Ulf Thewalt, and Bernhard Rieger. Chiral palladium (ii) complexes bearing tetradentate nitrogen ligands: synthesis, crystal structure and

reactivity towards the polymerization of norbornene. *Journal of organometallic chemistry*, 587(1):58–66, 1999. 19

[98] Takashi Tsujino, Takeo Saegusa, and Junji Furukawa. Polymerization of norbornene by modified ziegler-catalysts. *Die Makromolekulare Chemie*, 85(1):71–79, 1965. 20

[99] W Kaminsky, A Bark, and M Arndt. New polymers by homogenous zirconocene/aluminoxane catalysts. *Makromolekulare Chemie. Macromolecular Symposia*, 47(1):83–93, 1991. 20, 41

[100] Michael Arndt, Rüdiger Engehausen, Walter Kaminsky, and Konstantin Zoumis. Hydrooligomerization of cycloolefins-a view of the microstructure of polynorbornene. *Journal of Molecular Catalysis A: Chemical*, 101(3):171–178, 1995. 20

[101] Stephen L Mayo, Barry D Olafson, and William A Goddard. Dreiding: a generic force field for molecular simulations. *Journal of Physical chemistry*, 94(26):8897–8909, 1990. 20

[102] Th FA Haselwander, W Heitz, St A Krügel, and JH Wendorff. Rigid random coils: rotationally confined chain molecules. *Macromolecules*, 30(18):5345–5351, 1997. 20

[103] Stefan A Krügel, Florian Raubacher, and Joachim H Wendorff. Polynorbornene in the condensed state: Simulations on chain conformations and dynamics. *Macromolecular Chemistry and Physics*, 199(5):757–762, 1998. 20

[104] Bernard R Brooks, Robert E Bruccoleri, Barry D Olafson, David J States, S a Swaminathan, and Martin Karplus. Charmm: a program for macromolecular energy, minimization, and dynamics calculations. *Journal of computational chemistry*, 4(2):187–217, 1983. 21

[105] S Ahmed, PJ Ludovice, and P Kohl. Microstructure of 2, 3 erythro di-isotactic polynorbornene from atomistic simulation. *Computational and Theoretical Polymer Science*, 10(1-2):221–233, 2000. 21, 35, 42

[106] Won J. Chung, Clifford L. Henderson, and Peter J. Ludovice. Ris model of the helix-kink conformation of erythro diisotactic polynobornene. *Macromolecular Theory and Simulations*, 19(7):421–431, 2010. 21, 42

[107] Marie Tschage, Seungwhan Jung, Thomas P Spaniol, and Jun Okuda. Polymerization of norbornene using chiral bis (phenolate) zirconium catalysts. *Macromolecular Rapid Communications*, 36(2):219–223, 2015. 21

[108] Annamaria Buono, Antonino Famulari, Stefano Valdo Meille, Giovanni Ricci, and Lido Porri. 2, 3-exo-disyndiotactic polynorbornene: a crystalline polymer with tubular helical molecular structure. *Macromolecules*, 44(10):3681–3684, 2011. 21, 32, 35

[109] Berk Hess, Henk Bekker, Herman JC Berendsen, Johannes GEM Fraaije, et al. Lincs: a linear constraint solver for molecular simulations. *Journal of computational chemistry*, 18(12):1463–1472, 1997. 22, 42

[110] Michele Parrinello and Aneesur Rahman. Polymorphic transitions in single crystals: A new molecular dynamics method. *J. Appl. Phys.*, 52(12):7182–7190, 1981. 22, 42, 56, 63

[111] W. Schommers. Pair potentials in disordered many-particle systems: A study for liquid gallium. *Phys. Rev. A*, 28:3599–3605, Dec 1983. 22, 53

[112] Florian Müller-Plathe. Coarse-graining in polymer simulation: From the atomistic to the mesoscopic scale and back. *Chem. Phys. Chem.*, 3(9):754–769, 2002. 22, 52, 53

[113] Thomas A Halgren. The representation of van der waals (vdw) interactions in molecular mechanics force fields: potential form, combination rules, and vdw parameters. *Journal of the American Chemical Society*, 114(20):7827–7843, 1992. 26

[114] Jeffrey R Errington, Georgios C Boulougouris, Ioannis G Economou, Athanassios Z Panagiotopoulos, and Doros N Theodorou. Molecular simulation of phase equilibria for water- methane and water- ethane mixtures. *The Journal of Physical Chemistry B*, 102(44):8865–8873, 1998. 26

[115] Donald E Williams. Nonbonded potential parameters derived from crystalline hydrocarbons. *The Journal of Chemical Physics*, 47(11):4680–4684, 1967. 26

[116] Nathaniel Wentzel and Scott T Milner. Crystal and rotator phases of n-alkanes: A molecular dynamics study. *The Journal of Chemical Physics*, 132(4):044901, 2010. 26

[117] Nathaniel Wentzel and Scott T Milner. Simulation of multiple ordered phases in c23 n-alkane. *The Journal of chemical physics*, 134(22):224504, 2011. 26

[118] Lee-Ping Wang, Jiahao Chen, and Troy Van Voorhis. Systematic parametrization of polarizable force fields from quantum chemistry data. *Journal of chemical theory and computation*, 9(1):452–460, 2013. 26

[119] Marie-Madeleine Walz, Mohammad M Ghahremanpour, Paul J Van Maaren, and David Van der Spoel. Phase-transferable force field for alkali halides. *Journal of chemical theory and computation*, 14(11):5933–5948, 2018. 26

[120] Giovanni Ricci, Aldo Boglia, Antonella Caterina Boccia, Lucia Zetta, Antonino Famulari, and Stefano Valdo Meille. New stereoregularity in the stereospecific polymerization of bulky strained olefins: Diheterotactic polynorbornene. *Macromolecules*, 41(9):3109–3113, 2008. 32

[121] Alexey V Lyulin, Nikolaj K Balabaev, and MAJ Michels. Molecular-weight and cooling-rate dependence of simulated t g for amorphous polystyrene. *Macromolecules*, 36(22):8574–8575, 2003. 32, 43

[122] R Brüning and K Samwer. Glass transition on long time scales. *Physical Review B*, 46(18):11318, 1992. 32, 43

[123] Jie Han, Richard H Gee, and Richard H Boyd. Glass transition temperatures of polymers from molecular dynamics simulations. *Macromolecules*, 27(26):7781–7784, 1994. 32, 43

[124] Katharina Vollmayr, Walter Kob, and Kurt Binder. How do the properties of a glass depend on the cooling rate? a computer simulation study of a lennard-jones system. *The Journal of chemical physics*, 105(11):4714–4728, 1996. 32, 43

[125] Incoronata Tritto, Laura Boggioni, and Dino R Ferro. Metallocene catalyzed ethene-and propene co-norbornene polymerization: Mechanisms from a detailed microstructural analysis. *Coordination chemistry reviews*, 250(1-2):212–241, 2006. 41, 42

[126] Ronald R Lamonte and Donal McNally. Cyclic olefin copolymers. *Advanced Materials and Processes*, 159(3):33–36, 2001. 41

[127] Pedro S Nunes, Pelle D Ohlsson, Olga Ordeig, and Jörg P Kutter. Cyclic olefin polymers: emerging materials for lab-on-a-chip applications. *Microfluidics and nanofluidics*, 9(2):145–161, 2010. 41

[128] Jacek Dudowicz, Karl F Freed, and Jack F Douglas. Generalized entropy theory of polymer glass formation. *Advances in Chemical Physics*, 137:125, 2008. 42

[129] Evgeny B Stukalin, Jack F Douglas, and Karl F Freed. Application of the entropy theory of glass formation to poly (α-olefins). *The Journal of chemical physics*, 131(11):114905, 2009. 42

[130] Xiaolei Xu, Jack F Douglas, and Wen-Sheng Xu. Influence of side-chain length and relative rigidities of backbone and side chains on glass formation of branched polymers. *Macromolecules*, 54(13):6327–6341, 2021. 42

[131] Christine Gerstl, Gerald J Schneider, A Fuxman, M Zamponi, B Frick, T Seydel, M Koza, A-C Genix, J Allgaier, Dieter Richter, et al. Quasielastic neutron scattering study on the dynamics of poly (alkylene oxide) s. *Macromolecules*, 45(10):4394–4405, 2012. 42

[132] Carlos R López-Barrón, Patrick Brant, Aaron PR Eberle, and Donna J Crowther. Linear rheology and structure of molecular bottlebrushes with short side chains. *Journal of Rheology*, 59(3):865–883, 2015. 42

[133] Joshua C Worch, Hannah Prydderch, Sètuhn Jimaja, Panagiotis Bexis, Matthew L Becker, and Andrew P Dove. Stereochemical enhancement of polymer properties. *Nature Reviews Chemistry*, 3(9):514–535, 2019. 42

[134] TFA Haselwander, W Heitz, and M Maskos. Vinylic polymerization of norbornene by pd (ii)-catalysis in the presence of ethylene. *Macromolecular rapid communications*, 18(8):689–697, 1997. 42

[135] Savant Ahmed, Sue Ann Bidstrup, Paul Kohl, and Peter Ludovice. Stereochemical structure-property relationships in polynorbornene from simulation. *Macromolecular Symposia*, 133(1):1–10, 1998. 42

[136] J Katajisto, M Linnolahti, and TA Pakkanen. Properties of modified cyclo-olefin copolymers predicted by ab initio and molecular simulation techniques. *Theoretical Chemistry Accounts*, 113(5):281–286, 2005. 42

[137] Jussi Katajisto, Mikko Linnolahti, and Tapani A Pakkanen. Effect of branching of cyclo-olefin copolymers and polycarbonate polymers on mechanical and optical properties: Ab initio and molecular simulation study. *Journal of Molecular Structure: THEOCHEM*, 758(2-3):189–194, 2006. 42

[138] Michail Mazo, Nikolay Balabaev, Alexandre Alentiev, and Yury Yampolskii. Molecular dynamics simulation of nanostructure of high free volume polymers with sime3 side groups. *Macromolecules*, 51(4):1398–1408, 2018. 42

[139] Prince E Rouse Jr. A theory of the linear viscoelastic properties of dilute solutions of coiling polymers. *The Journal of Chemical Physics*, 21(7):1272–1280, 1953. 47

[140] Nobahar Shahidi, Antonis Chazirakis, Vagelis Harmandaris, and Manolis Doxastakis. Coarse-graining of polyisoprene melts using inverse monte carlo and local density potentials. *The Journal of chemical physics*, 152(12):124902, 2020. 52, 56

[141] Kurt Binder. *Monte Carlo and molecular dynamics simulations in polymer science*. Oxford University Press, 1995. 52

[142] Yogendra Narayan Pandey, George J. Papakonstantopoulos, and Manolis Doxastakis. Polymer/nanoparticle interactions: Bridging the gap. *Macromolecules*, 46(13):5097–5106, 2013. 52, 53, 82

[143] Karen Johnston and Vagelis Harmandaris. Hierarchical simulations of hybrid polymer–solid materials. *Soft Matter*, 9(29):6696–6710, 2013. 52, 82

[144] Raffaello Potestio, Christine Peter, and Kurt Kremer. Computer simulations of soft matter: Linking the scales. *Entropy*, 16(8):4199–4245, 2014. 52

[145] Nicholas J. H. Dunn, Thomas T. Foley, and William G. Noid. Van der waals perspective on coarse-graining: Progress toward solving representability and transferability problems. *Acc. Chem. Res.*, 49(12):2832–2840, 2016. 52, 54

[146] E. Kalligiannaki, A. Chazirakis, A. Tsourtis, M.A. Katsoulakis, P. Plecháč, and V. Harmandaris. Parametrizing coarse grained models for molecular systems at equilibrium. *Eur. Phys. J. Spec. Top.*, 225(8):1347–1372, Oct 2016. 52, 74

[147] Mohammadhasan Dinpajooh and Marina G. Guenza. On the density dependence of the integral equation coarse-graining effective potential. *J. Phys. Chem. B*, 122(13):3426–3440, 2018. 52, 53, 54

[148] A.K. Soper. Empirical potential monte carlo simulation of fluid structure. *Chem. Phys.*, 202(2):295 – 306, 1996. 53

[149] Roland Faller. Automatic coarse graining of polymers. *Polymer*, 45(11):3869 – 3876, 2004. 53

[150] Qi Sun and Roland Faller. Systematic coarse-graining of a polymer blend: polyisoprene and polystyrene. *J. Chem. Theory Comput.*, 2(3):607–615, 2006. 53

[151] Qi Sun and Roland Faller. Phase separation in polyisoprene/polystyrene blends by a systematically coarse-grained model. *J. Chem. Phys.*, 126(14):144908, 2007. 53, 57

[152] Yogendra Narayan Pandey, Alexander Brayton, Craig Burkhart, George J. Papakonstantopoulos, and Manolis Doxastakis. Multiscale modeling of polyisoprene on graphite. *J. Chem. Phys.*, 140(5):054908, 2014. 53, 57, 63

[153] Vagelis Harmandaris, N. Adhikari, N.F.A. van der Vegt, and K. Kremer. Hierarchical modeling of polystyrene: From atomistic to coarse-grained simulations. *Macromolecules*, 39(-):6708, 2006. 53, 74, 77

[154] G. G. Zhang, A. Chazirakis, V. Harmandaris, T. Stuehn, K. Daoulas, and K. Kremer. Hierarchical modelling of polystyrene melts: from soft blobs to atomistic resolution. *Soft Matter*, 15(-):289–302, 2019. 53

[155] M. Guenza. Thermodynamic consistency and other challenges in coarse-graining models. *Eur. Phys. J. Spec. Top.*, 224(12):2177–2191, Sep 2015. 53

[156] Mohammadhasan Dinpajooh and Marina G. Guenza. Coarse-graining simulation approaches for polymer melts: the effect of potential range on computational efficiency. *Soft Matter*, 14:7126–7144, 2018. 53

[157] Sergei Izvekov and Gregory A. Voth. Multiscale coarse graining of liquid-state systems. *J. Chem. Phys.*, 123(13):134105, 2005. 53

[158] Teemu Murtola, Emma Falck, Mikko Karttunen, and Ilpo Vattulainen. Coarse-grained model for phospholipid/cholesterol bilayer employing inverse monte carlo with thermodynamic constraints. *J. Chem. Phys.*, 126(7):075101, 2007. 53, 62, 63

[159] Sergei Izvekov, Peter W. Chung, and Betsy M. Rice. The multiscale coarse-graining method: Assessing its accuracy and introducing density dependent coarse-grain potentials. *J. Chem. Phys.*, 133(6):064109, 2010. 53, 57

[160] Avisek Das and Hans C. Andersen. The multiscale coarse-graining method. v. isothermal-isobaric ensemble. *J. Chem. Phys.*, 132(16):164106, 2010. 53, 54

[161] Chia-Chun Fu, Pandurang M. Kulkarni, M. Scott Shell, and L. Gary Leal. A test of systematic coarse-graining of molecular dynamics simulations: Thermodynamic properties. *J. Chem. Phys.*, 137(16):164106, 2012. 53

[162] Takahiro Ohkuma and Kurt Kremer. Comparison of two coarse-grained models of cis-polyisoprene with and without pressure correction. *Polymer*, 130:88–101, 2017. 53, 55, 56, 74

[163] J. E. Mark. Random-coil configurations of cis-1,4-polybutadiene and cis-1,4-polyisoprene. theoretical interpretation. *J. Am. Chem. Soc.*, 88(19):4354–4359, 1966. 54

[164] M. Doxastakis, V. G. Mavrantzas, and D. N. Theodorou. Atomistic monte carlo simulation of cis-1,4 polyisoprene melts. i. single temperature end-bridging monte carlo simulations. *J. Chem. Phys.*, 115(24):11339–11351, 2001. 54, 56, 69

[165] Nicholas J. H. Dunn and W. G. Noid. Bottom-up coarse-grained models that accurately describe the structure, pressure, and compressibility of molecular liquids. *J. Chem. Phys.*, 143(24):243148, 2015. 54, 67

[166] David Rosenberger and Nico F. A. van der Vegt. Addressing the temperature transferability of structure based coarse graining models. *Phys. Chem. Chem. Phys.*, 20:6617–6628, 2018. 54

[167] Murray S. Daw and M. I. Baskes. Semiempirical, quantum mechanical calculation of hydrogen embrittlement in metals. *Phys. Rev. Lett.*, 50:1285–1288, Apr 1983. 54

[168] Murray S. Daw and M. I. Baskes. Embedded-atom method: Derivation and application to impurities, surfaces, and other defects in metals. *Phys. Rev. B*, 29:6443–6453, Jun 1984. 54

[169] I. Pagonabarraga and D. Frenkel. Non-ideal dpd fluids. *Mol. Simul.*, 25(3-4):167–175, 2000. 54

[170] Samy Merabia and Ignacio Pagonabarraga. Density dependent potentials: Structure and thermodynamics. *J. Chem. Phys.*, 127(5):054903, 2007. 54

[171] Erik C. Allen and Gregory C. Rutledge. A novel algorithm for creating coarse-grained, density dependent implicit solvent models. *J. Chem. Phys.*, 128(15):154115, 2008. 54

[172] Erik C. Allen and Gregory C. Rutledge. Evaluating the transferability of coarse-grained, density-dependent implicit solvent models to mixtures and chains. *J. Chem. Phys.*, 130(3):034904, 2009. 54

[173] Sergei Izvekov, Peter W Chung, and Betsy M Rice. Particle-based multiscale coarse graining with density-dependent potentials: Application to molecular crystals (hexahydro-1, 3, 5-trinitro-s-triazine). *J. Chem. Phys.*, 135(4):044112, 2011. 54, 57

[174] Gérôme Faure, Jean-Bernard Maillet, and Gabriel Stoltz. Local density dependent potential for compressible mesoparticles. *J. Chem. Phys.*, 140(11):114105, 2014. 54, 58

[175] Tanmoy Sanyal and M. Scott Shell. Coarse-grained models using local-density potentials optimized with the relative entropy: Application to implicit solvation. *J. Chem. Phys.*, 145(3):034109, 2016. 54, 55, 58, 62, 67

[176] Joshua D. Moore, Brian C. Barnes, Sergei Izvekov, Martin Lísal, Michael S. Sellers, DeCarlos E. Taylor, and John K. Brennan. A coarse-grain force field for rdx: Density dependent and energy conserving. *J. Chem. Phys.*, 144(10):104501, 2016. 54, 57, 60

[177] Vipin Agrawal, Gaurav Arya, and Jay Oswald. Simultaneous iterative boltzmann inversion for coarse-graining of polyurea. *Macromolecules*, 47(10):3378–3389, 2014. 54, 67

[178] Jacob W. Wagner, Thomas Dannenhoffer-Lafage, Jaehyeok Jin, and Gregory A. Voth. Extending the range and physical accuracy of coarse-grained models: Order parameter dependent interactions. *J. Chem. Phys.*, 147(4):044113, 2017. 54

[179] James P. Larentzos, J. Matthew Mansell, Martin Lísal, and John K. Brennan. Coarse-grain modelling using an equation-of-state many-body potential: application to fluid mixtures at high temperature and high pressure. *Mol. Phys.*, 0(0):1–12, 2018. 54

[180] Tanmoy Sanyal and M. Scott Shell. Transferable coarse-grained models of liquid–liquid equilibrium using local density potentials optimized with the relative entropy. *J. Phys. Chem. B*, 122(21):5678–5693, 2018. 54, 58, 67

[181] David Rosenberger, Tanmoy Sanyal, M Scott Shell, and Nico FA van der Vegt. Transferability of local density-assisted implicit solvation models for homogeneous fluid

mixtures. *Journal of Chemical Theory and Computation*, 15(5):2881–2895, 2019. 54, 58

[182] Vipin Agrawal, Pedro Peralta, Yiyang Li, and Jay Oswald. A pressure-transferable coarse-grained potential for modeling the shock hugoniot of polyethylene. *J. Chem. Phys.*, 145(10):104903, 2016. 55

[183] Anastasios Tsourtis, Vagelis Harmandaris, and Dimitrios Tsagkarogiannis. Parameterization of coarse-grained molecular interactions through potential of mean force calculations and cluster expansion techniques. *Entropy*, 19(8):395, 2017. 55, 82

[184] M. Doxastakis, V. G. Mavrantzas, and D. N. Theodorou. Atomistic monte carlo simulation of cis-1,4 polyisoprene melts. ii. parallel tempering end-bridging monte carlo simulations. *J. Chem. Phys.*, 115(24):11352–11361, 2001. 56

[185] V. A. Harmandaris, M. Doxastakis, V. G. Mavrantzas, and D. N. Theodorou. Detailed molecular dynamics simulation of the self-diffusion of n-alkane and cis-1,4 polyisoprene oligomer melts. *J. Chem. Phys.*, 116(1):436–446, 2002. 56, 58

[186] M. Doxastakis, D. N. Theodorou, G. Fytas, F. Kremer, R. Faller, F. Müller-Plathe, and N. Hadjichristidis. Chain and local dynamics of polyisoprene as probed by experiments and computer simulations. *J. Chem. Phys.*, 119(13):6883–6894, 2003. 56

[187] Pragati Sharma, Sudip Roy, and Hossein Ali Karimi-Varzaneh. Validation of force fields of rubber through glass-transition temperature calculation by microsecond atomic-scale molecular dynamics simulation. *J. Phys. Chem. B*, 120(7):1367–1379, 2016. 56

[188] Shuichi Nosé and ML Klein. Constant pressure molecular dynamics for molecular systems. *Mol. Phys.*, 50(5):1055–1076, 1983. 56, 63

[189] Shūichi Nosé. A molecular dynamics method for simulations in the canonical ensemble. *Mol. Phys.*, 52(2):255–268, 1984. 56, 63

[190] William G Hoover. Canonical dynamics: Equilibrium phase-space distributions. *Phys. Rev. A*, 31(3):1695, 1985. 56, 63

[191] WW Graessley and SF Edwards. Entanglement interactions in polymers and the chain contour concentration. *Polymer*, 22(10):1329–1334, 1981. 56

[192] Robert A Orwoll. Densities, coefficients of thermal expansion, and compressibilities of amorphous polymers. In *Physical properties of polymers handbook*, pages 93–101. Springer, 2007. 56

[193] YX Yi and P Zoller. An experimental and theoretical study of the pvt equation of state of butadiene and isoprene elastomers to 200 c and 200 mpa. *J. Polym. Sci., Part B: Polym. Phys.*, 31(7):779–788, 1993. 56

[194] Md Salah Uddin and Jaehyung Ju. Multiscale modeling of a natural rubber: Bridging a coarse-grained molecular model to the rubber network theory. *Polymer*, 101:34–47, 2016. 57

[195] Leon B Lucy. A numerical approach to the testing of the fission hypothesis. *Astron. J.*, 82:1013–1024, 1977. 57

[196] Robert A Gingold and Joseph J Monaghan. Smoothed particle hydrodynamics: theory and application to non-spherical stars. *Mon. Not. R. Astron. Soc*, 181(3):375–389, 1977. 57

[197] Pep Espanol and Mariano Revenga. Smoothed dissipative particle dynamics. *Phys. Rev. E*, 67(2):026705, 2003. 57

[198] Atsuyuki Okabe, Barry Boots, Kokichi Sugihara, and Sung Nok Chiu. *Spatial tessellations: concepts and applications of Voronoi diagrams*, volume 501. John Wiley & Sons, 2009. 58

[199] Donald E Knuth. *Art of computer programming, volume 2: Seminumerical algorithms*. Addison-Wesley Professional, 2014. 58

[200] Peter Wilcox Jones, Andrei Osipov, and Vladimir Rokhlin. Randomized approximate nearest neighbors algorithm. *Proc. Natl. Acad. Sci. U.S.A*, 108(38):15679–15686, 2011. 58

[201] SY Trofimov, ELF Nies, and MAJ Michels. Thermodynamic consistency in dissipative particle dynamics simulations of strongly nonideal liquids and liquid mixtures. *J. Chem. Phys.*, 117(20):9383–9394, 2002. 60

[202] P. B. Warren. Vapor-liquid coexistence in many-body dissipative particle dynamics. *Phys. Rev. E*, 68:066702, Dec 2003. 60

[203] Patrick B Warren. No-go theorem in many-body dissipative particle dynamics. *Phys. Rev. E*, 87(4):045303, 2013. 60

[204] Alexander P Lyubartsev and Aatto Laaksonen. On the reduction of molecular degrees of freedom in computer simulations. In *Novel Methods in Soft Matter Simulations*, pages 219–244. Springer, 2004. 61, 62

[205] Alexey Savelyev and Garegin A. Papoian. Molecular renormalization group coarse-graining of polymer chains: Application to double-stranded dna. *Biophys. J.*, 96(10):4044 – 4052, 2009. 62

[206] I Pagonabarraga and D Frenkel. Dissipative particle dynamics for interacting systems. *J. Chem. Phys.*, 115(11):5015–5026, 2001. 62

[207] Daan Frenkel and Berend Smit. *Understanding Molecular Simulation From Algorithms to Applications*. Academic Press, California, 2002. 63

[208] Alexander Lyubartsev, Alexander Mirzoev, LiJun Chen, and Aatto Laaksonen. Systematic coarse-graining of molecular models by the newton inversion method. *Faraday Discuss.*, 144:43–56, 2010. 63

[209] David Rosenberger, Martin Hanke, and Nico FA van der Vegt. Comparison of iterative inverse coarse-graining methods. *Eur. Phys. J. Spec. Top.*, 225(8-9):1323–1345, 2016. 63

[210] Michael R. DeLyser and William G. Noid. Extending pressure-matching to inhomogeneous systems via local-density potentials. *J. Chem. Phys.*, 147(13):134111, 2017. 67

[211] Timothy C Moore, Christopher R Iacovella, and Clare McCabe. Derivation of coarse-grained potentials via multistate iterative boltzmann inversion. *J. Chem. Phys.*, 140(22):06B606_1, 2014. 67

[212] Timothy C Moore, Christopher R Iacovella, Remco Hartkamp, Annette L Bunge, and Clare McCabe. A coarse-grained model of stratum corneum lipids: Free fatty acids and ceramide ns. *J. Phys. Chem. B*, 120(37):9944–9958, 2016. 67

[213] M P Allen and D J Tildesley. *Computer Simulation of Liquids*. Oxford University Press, New York, 1987. 72

[214] Vagelis Harmandaris and Kurt Kremer. Dynamics of polystyrene melts through hierarchical multiscale simulations. *Macromolecules*, 42(-):791–802, 2009. 75, 77

[215] Vagelis Harmandaris and Kurt Kremer. Predicting polymer dynamics at multiple length and time scales. *Soft Matter*, 5(-):3920–3926, 2009. 75

[216] Vagelis Harmandaris, N. Adhikari, N.F.A. van der Vegt, K. Kremer, B. Mann, R. Voelkel, C.C. Liew, and H. Weiss. Ethylbenzene diffusion in polystyrene: United atom atomistic/coarse grained simulations and experiments. *Macromolecules*, 40(-):7026, 2007. 77

[217] Neil E Moe and MD Ediger. Calculation of the coherent dynamic structure factor of polyisoprene from molecular dynamics simulations. *Phys. Rev. E*, 59(1):623, 1999. 78, 80

[218] JJ Salacuse, AR Denton, and PA Egelstaff. Finite-size effects in molecular dynamics simulations: Static structure factor and compressibility. i. theoretical method. *Phys. Rev. E*, 53(3):2382, 1996. 78

[219] VA Harmandaris, VG Mavrantzas, DN Theodorou, Martin Kröger, J Ramirez, Hans Christian Öttinger, and D Vlassopoulos. Crossover from the rouse to the entangled polymer melt regime: signals from long, detailed atomistic molecular dynamics simulations, supported by rheological experiments. *Macromolecules*, 36(4):1376–1387, 2003. 78

[220] M. Doxastakis, K. Chrissopoulou, A. Aouadi, B. Frick, T. P. Lodge, and G. Fytas. Segmental dynamics of disordered styrene–isoprene tetrablock copolymers. *J. Chem. Phys.*, 116(11):4707–4714, 2002. 82

[221] Vagelis Harmandaris and Manolis Doxastakis. Molecular dynamics of polyisoprene/polystyrene oligomer blends: The role of self-concentration and fluctuations on blend dynamics. *J. Chem. Phys.*, 139(3):034904, 2013. 82

Nobahar Shahidi was born in Tehran, Iran in 1993. She studied chemical engineering at the Sharif University of Technology, Tehran, and obtained her bachelor's degree in 2016. She attended the University of Tennessee, Knoxville, and joined Dr. Doxastakis's research group in 2017 to pursue her doctoral degree in chemical engineering. Her doctoral research has focused on developing and implementing multiscale computational models for macromolecules.